# DISSERTATION | DOCTORAL THESIS

Titel | Title

Clouds and bare sea ice as key factors in stabilizing waterbelt solutions for Snowball Earth

verfasst von | submitted by

Johannes Hörner B.Sc. M.Sc.

angestrebter akademischer Grad | in partial fulfilment of the requirements for the degree of

Doktor der Naturwissenschaften (Dr.rer.nat.)

Wien | Vienna, 2025

| | |
|---|---|
| Studienkennzahl lt. Studienblatt \| Degree programme code as it appears on the student record sheet: | UA 796 605 415 |
| Dissertationsgebiet lt. Studienblatt \| Field of study as it appears on the student record sheet: | Meteorologie |
| Betreut von \| Supervisor: | Univ.-Prof. Dr. Aiko Voigt |

*Die Forscher, die sich mit [...] dem Klima der Erde befassen, sind reine Erfahrungswissenschaftler. Sie haben keine Lust, sich mit komplizierten mathematischen Theorien zu befassen. [...] Man könnte es von ihnen auch gar nicht verlangen, durch den Schornstein den Weg in ein Gebäude zu suchen, dessen Pforte weit geöffnet steht.*

**— Milanković, 1957**

# Abstract

Snowball Earth describes several periods in Earth's history when geological evidence indicates that the entire planet was covered in ice. This was caused by a runaway ice-albedo feedback, where increasing ice cover and decreasing temperatures reinforce each other, resulting in global ice cover. However, the Snowball Earth theory is challenged by the question of how aquatic phototrophic life was able to survive a globally ice covered ocean.

Waterbelt states are one possible scenario of Snowball Earth, where a narrow strip of ocean remains ice-free at the equator. They pose an attractive alternative, as they reconcile the survival of life with the geological evidence. However, these states are disputed due to significant uncertainty surrounding the mechanisms that stabilize them.

The Jormungand mechanism describes one such mechanism that is able to stabilize a waterbelt state. When sea ice reaches the subtropical desert regions, it falls under the descending branch of the Hadley circulation, leading to a negative precipitation-evaporation balance. As a result, snow on ice melts and bare, darker sea ice is exposed. This weakens the ice-albedo feedback and stabilizes the climate in a waterbelt state. This thesis investigates the robustness of this mechanism in three approaches.

First, the existence of bare sea ice is investigated. The ICON model is run with different thermodynamic sea-ice models, showing that a simple sea ice model overestimates the bare sea-ice region and thus the stabilizing effect of the Jormungand mechanism.

Second, the role of clouds for the Jormungand mechanism is examined. Clouds have been shown to stabilize waterbelt states by masking the ice-albedo feedback, but they also induce their own radiative feedbacks. Using the approximate partial radiative perturbation method, a cloud masking parameter is defined that enables the quantitative comparison between cloud masking, cloud feedback and ice-albedo feedback. Applying this framework on ICON simulations with retuned cloud physics shows that both cloud masking and cloud feedback determine waterbelt states.

Third, we apply this framework to output of different climate models. Waterbelt states in different versions of the ICON and CAM models are analysed with respect to the role of bare sea ice and clouds. Preliminary results assert the relevance of clouds. The CAM models simulate a larger and more stable waterbelt state due to larger cloud masking as well as a stabilizing shortwave cloud feedback.

The results of this thesis imply that the Jormungand mechanism may be too weak to stabilize waterbelt states on its own; its effect may be overestimated due to simple sea-ice models. Thus, it may only be a secondary mechanism for waterbelt stability. Additionally, the results emphasize the importance of clouds for waterbelt stability. Clouds can influence waterbelt stability by masking the ice-albedo feedback and inducing cloud radiative feedbacks. Thus, in order to constrain the uncertainty associated with waterbelt states, the uncertainty of clouds during the climate transition to a Snowball Earth must be constrained by future studies.

# Zusammenfassung

Die Schneeballerde beschreibt mehrere Perioden in der Erdgeschichte, in denen geologische Beweise darauf hindeuten, dass der gesamte Planet mit Eis bedeckt war. Dies wurde durch eine unkontrollierte Eis-Albedo-Rückkopplung verursacht, bei der sich eine zunehmende Eisbedeckung und sinkende Temperaturen gegenseitig verstärken, was zu einer globalen Eisbedeckung führt. Die Schneeballerde-Theorie wird jedoch dadurch in Frage gestellt, wie aquatisches, phototrophes Leben in einem weltweit eisbedeckten Ozean überleben konnte.

Ein mögliches Szenario der Schneeballerde sind Wassergürtelzustände, in denen ein schmaler Streifen des Ozeans am Äquator eisfrei bleibt. Sie stellen eine attraktive Alternative dar, da sie das Überleben von Leben mit den geologischen Beweisen in Einklang bringen. Diese Zustände sind jedoch umstritten, da die Mechanismen, die sie stabilisieren, mit großer Unsicherheit behaftet sind.

Der Jormungand-Mechanismus beschreibt einen solchen Mechanismus, der in der Lage ist, einen Wassergürtelzustand zu stabilisieren. Wenn Meereis die subtropischen Wüstenregionen erreicht, gerät es unter den absteigenden Ast der Hadley-Zirkulation, was zu einer Nettoablation von Eis an der Oberfläche führt. Infolgedessen schmilzt der Schnee auf dem Eis und das blanke, dunklere Meereis wird freigelegt. Dies schwächt die Eis-Albedo-Rückkopplung ab und stabilisiert das Klima in einem Wassergürtelzustand. In dieser Arbeit wird die Robustheit dieses Mechanismus in drei Ansätzen untersucht.

Zunächst wird die Existenz von blankem Meereis untersucht. Das ICON-Modell wird mit verschiedenen thermodynamischen Meereismodellen getestet. Dabei zeigt sich, dass ein einfaches Meereismodell die Größe der schneefreien Meereisregion und damit die stabilisierende Wirkung des Jormungand-Mechanismus überschätzt.

Zweitens wird die Rolle der Wolken für den Jormungand-Mechanismus untersucht. Frühere Arbeiten haben gezeigt, dass Wolken den Wassergürtelzustand stabilisieren, indem sie die Eis-Albedo-Rückkopplung maskieren. Sie induzieren allerdings auch ihre eigenen Strahlungsrückkopplungen. Mit Hilfe der "approximate partial radiative perturbation" Methode wird ein Wolkenmaskierungsparameter

definiert, der einen quantitativen Vergleich zwischen Wolkenmaskierung, Wolkenrückkopplung und Eis-Albedo-Rückkopplung ermöglicht. Die Anwendung dieses Verfahrens auf ICON-Simulationen mit neu angepasster Wolkenphysik zeigt, dass sowohl Wolkenmaskierung als auch Wolkenrückkopplung den Wassergürtelzustand bestimmen.

Drittens wird dieses Verfahren auf Daten verschiedener Klimamodelle angewendet. Der Wassergürtelzustand in verschiedenen Versionen der ICON und CAM Modelle wird im Hinblick auf die Rolle von blankem Meereis und Wolken analysiert. Vorläufige Ergebnisse bestätigen die Bedeutung der Wolken. Die CAM-Modelle simulieren einen größeren und stabileren Wassergürtelzustand aufgrund einer größeren Wolkenmaskierung sowie einer stabilisierenden kurzwelligen Wolkenrückkopplung.

Die Ergebnisse dieser Arbeit deuten darauf hin, dass der Jormungand-Mechanismus möglicherweise zu schwach ist, um den Wassergürtelzustand allein zu stabilisieren; möglicherweise wird seine Wirkung aufgrund einfacher Meereismodelle überschätzt. Daher könnte er nur ein sekundärer Mechanismus für die Stabilität des Wassergürtelzustands sein. Außerdem unterstreichen die Ergebnisse die Bedeutung der Wolken für die Stabilität des Wassergürtelzustands. Wolken können die Stabilität des Wassergürtels beeinflussen, indem sie die Eis-Albedo-Rückkopplung maskieren und Wolkenstrahlungsrückkopplungen induzieren. Um die mit dem Wassergürtelzustand verbundenen Unsicherheiten zu verringern, muss daher die Unsicherheit der Wolken während des Klimaübergangs zu einer Schneeballerde in zukünftigen Untersuchungen eingegrenzt werden.

# Contents

# 1 Introduction

> *There is considerable geological evidence for an extensive glaciation some 600 million years ago. Its end caused an alteration of climate that made possible the proliferation of animal life in Cambrian times.*
>
> — **Harland and Rudwick (1964)**

Snowball Earth is an inherently interdisciplinary topic. The hypothesis arose from apparently contradictory geological discoveries that were explained using concepts from fundamental climate dynamics. As a first introduction to the topic, this chapter gives a brief chronological overview of the most important discoveries that led to the formation of the Snowball Earth hypothesis. The chronology is based on the books by Catling and Kasting (2017) and Prothero (2018, 2024), and the review paper by Hoffman et al. (2017).

While the discovery of geological evidence for Snowball Earth dates back to the 19th century (Reusch, 1891), the foundation of the Snowball Earth hypothesis was arguably laid by the work of Douglas Mawson (e.g., Mawson & Segnit, 1949). In field studies in southern Australia, they discovered glacial deposits dating back to the Neoproterozoic Era, indicating the existence of glaciers at sea level. Because of modern Australia's proximity to the equator, they proposed that this could only have happened if the Earth had undergone a global glaciation. However, this was controversial at the time because plate tectonics may have moved Australia closer to the poles in the Neoproterozoic.

Harland and Rudwick (1964) strengthened this hypothesis by showing that these glacial deposits are in fact not restricted to Australia, but are found on all continents. Advances in paleomagnetic methods have also made it possible to determine the latitude of origin of these deposits during the Neoproterozoic, tracing the places of origin all over the world, including close to the equator. In addition, they postulated that this global glaciation in the Neoproterozoic could be the reason for the emergence of complex life in the subsequent period, the Cambrian.

The climate dynamicists Budyko (1969) and Sellers (1969) then developed idealized energy balance models of the atmosphere. These models had one important implication for the Snowball Earth hypothesis: Earth's climate is multistable, and when ice cover reaches a critical latitude, a tipping point is passed, and Earth switches from its temperate climate state to a state where ice covers the entire globe. This provided an explanation how the Earth could reach such a global glaciation. However, due to the multistability of the climate, the Earth would be trapped in this "ice catastrophe" indefinitely. This made it impossible for the Earth to have ever been in this state.

Walker et al. (1981) solved this problem by providing a mechanism for Earth to end the ice catastrophe. Silicate weathering is a geochemical process that reduces atmospheric $CO_2$ content and deposits it on the ocean floor, acting as a climate thermostat. When the Earth's continents are covered in ice, this mechanism effectively ceases, resulting in a steady increase in atmospheric $CO_2$ due to natural outgassing by volcanoes. Eventually, the increase in atmospheric $CO_2$ could provide enough warming to allow the Earth to escape its frozen state.

This was also the reasoning that Kirschvink (1992) used to firstly propose the theory of Snowball Earth. The energy balance models of Budyko (1969) and Sellers (1969) explain how Earth can switch between a temperate and ice-covered state in geologically short time scales. Silicate weathering and volcanoes provide a mechanism that enables Earth to escape the Snowball Earth. And the geologically rapid climate transition from a temperate climate to a Snowball Earth and back is able to explain the geological evidence.

Later, Hoffman et al. (1998) and Hoffman and Schrag (2002) extended the hypothesis by postulating that the breakup of the supercontinent Rodinia led to the initial drawdown of atmospheric $CO_2$, causing the Earth's climate to pass the tipping point and enter a cycle of multiple Snowball Earth events. In addition, further geological evidence was presented that strengthened the theory. This brought Snowball Earth into the scientific mainstream, and since then more and more research has been done on the subject (Hoffman et al., 2017).

This thesis adds to the Snowball Earth research by analyzing one possible manifestation of the Snowball Earth climate: a waterbelt state, where Earth's climate has passed the tipping point of glaciation, but is prevented from global ice cover by stabilizing feedback mechanisms, resulting in a strip of open ocean at the equator that provides a refuge for life over the course of the Snowball Earth.

# 2 Scientific background

> *A conclusion on the possibility of complete glaciation of the Earth after ice cover reaches some critical latitude follows from the calculation [...] of the values of decrease in radiation necessary for further movement of ice to the equator.*
>
> — **Budyko (1969)**

## 2.1 Geological evidence

The Neoproterozoic is the geological era that extends from 1000 to 540 million years ago (Ma). It includes the Cryogenian period (from 720 Ma to 635 Ma), during which two global glaciations occurred: The Sturtian, from 717.5-716.3Ma to 659.3-658.5Ma, and shortly after the Marinoan, from 649.9-639.0Ma to 636.0-634.7Ma (Hoffman et al., 2017). This chapter gives a brief overview of the geological and biological features of the Cryogenian that are relevant to the Snowball Earth hypothesis. It is largely based on the review papers of Pierrehumbert et al. (2011) and Hoffman et al. (2017) and the books of Catling and Kasting (2017) and Prothero (2018).

### Breakup of the supercontinent Rodinia

During the Neoproterozoic, Earth's continents clustered together into the supercontinent Rodinia (Z. X. Li et al., 2008). At the beginning of the Cryogenian, at 725 Ma, Rodinia was centered at the equator and began to break up (Pierrehumbert et al., 2011). This breakup may have been responsible for a decrease in atmospheric $CO_2$ and consequent cooling of the climate via increased silicate weathering (Walker et al., 1981). Exposed silicate minerals react with $CO_2$ dissolved in rainwater to form carbonate minerals, which are transported to the ocean and deposited on the seafloor.

The breakup of Rodinia may have accelerated this process in two ways: First, newly emerging continental shelves near the coasts can increase the burial rates of $CO_2$. Second, the humidification of the continental interior resulting from the smaller continent size can increase the efficiency of silicate weathering (Hoffman et al., 1998, 2017; Donnadieu et al., 2004).

### Glacial deposits

Cryogenian glacial deposits include glacial striations, diamictites, and dropstones (Pierrehumbert et al., 2011). Glacial striations are scratches in bedrock caused by flowing glaciers. Diamictites are unsorted sediment consisting of larger particles dispersed in a finer matrix, generally considered to be of glacial origin (Catling & Kasting, 2017; Prothero, 2018). Dropstones are singular, large rocks or boulders dumped into finer-grained sediments of marine origin. These boulders are transported either by icebergs or a continuous ice shelf from continents across the open ocean, and then dropped into the sediment of the ocean floor when the ice melts (Hoffman et al., 2017).

Paleomagnetic data show that these deposits originated globally, including near the equator (e.g., Z. X. Li et al., 2008, 2013; Evans, 2013). This indicates that glaciations were not limited to high latitudes, but instead of global extent. Additionally, radiometric dating with U-Pb and Re-Os chronology confirms that these deposits were created synchronously (e.g., Macdonald et al., 2010; P. Liu et al., 2015; Rooney et al., 2015). The evidence thus suggest two global glaciations during the Cryogenian: The Sturtian, which lasted from 717.5-716.3Ma to 659.3-658.5Ma, and the Marinoan, which is less well constrained with an onset at 649.9-639.0Ma and an end at 636.0-634.7Ma (Hoffman et al., 2017).

Ultimately, the synchronous formation of glacial deposits over all latitudes are a strong indicator for global or near global glaciation.

### Cap carbonates

Another piece of geological evidence unique to the Neoproterozoic are cap-carbonates (Pierrehumbert et al., 2011). These are thick layers of carbonate rock, limestone or dolomite layered on top of the glacial diamictites described above. Features such as giant wave ripples (e.g., Allen & Hoffman, 2005) and crystal structures (e.g., Hoffman, 2011; Grotzinger & Knoll, 1995) indicate that these carbonates were deposited rapidly.

Rapid deposition of carbonate rocks on the ocean floor requires a sudden and massive increase in the carbonate ion content of the water. The end of a Snowball Earth provides a possible explanation for this (Hoffman et al., 1998; Kirschvink, 1992). The high atmospheric $CO_2$ after the end of a Snowball Earth would result in hot acid rain, facilitating the dissolution of carbonate ions from exposed carbonate rocks in the continental interior. The carbonate is then transported to the ocean, where saturation reaches such high levels that rapid rates of carbonate precipitation can occur.

The cap carbonates overlying the glacial diamictites thus indicate that the Neoproterozoic climate underwent a rapid change from an extremely cold climate with equatorial glaciers to a hot climate with high atmospheric $CO_2$.

#### Banded iron formations

The creation of banded iron formations requires ocean water with large amounts of dissolved iron. This is only possible when large parts of the ocean are anoxic and low in sulfate (Pierrehumbert et al., 2011). Banded iron formations then form when iron-rich anoxic water comes into contact with oxygen. These formations are sometimes found mixed with glacial deposits, indicating that they formed during glaciation. This has two implications: First, large parts of the ocean must be covered by ice for the water to become anoxic. Second, small parts of the ocean must be ice-free to provide an oxygen supply and allow mixing between iron-rich anoxic water and oxygen (Pierrehumbert et al., 2011).

Conversely, banded iron formations can also be formed in anoxic environments by phototrophic bacteria (Kappler et al., 2005). While this biological process does not require oxygen, it does require sunlight to reach the seawater. This means that either some parts of the ocean were not covered with ice, or the ice was partially thin enough for sunlight to penetrate.

#### Life

The Cryogenian period marks an important point in the history of life on Earth. It is the last period of the Proterozoic Eon and is followed by the Cambrian period in the Phanerozoic Eon. While life first appeared on Earth much earlier, it was during the Cambrian that a large number of complex, multicellular species first arose (Catling & Kasting, 2017). Thus, the Cryogenian glaciations occurred just before the emergence of complex life on Earth.

In fact, it is hypothesized that the Cryogenian glaciations may have been the cause of the emergence of complex life in the Cambrian (Harland & Rudwick, 1964; Runnegar, 2000; Hoffman & Schrag, 2002; Crockett et al., 2024). The extreme climatic conditions may have acted as an evolutionary filter, accelerating the evolution of life.

However, some of the life forms that existed before and survived the Cryogenian pose a challenge to the Snowball hypothesis, because they would likely not be able to survive a globally ice-covered ocean. These are photosynthetic eukaryotes (green algae) and cyanobacteria (Waldbauer et al., 2009; Pierrehumbert et al., 2011). These species need sunlight penetrating into liquid water in order to survive. In addition, fossil steroids suggests that early animals, specifically sponges, already existed in the Cryogenian (Brocks & Butterfield, 2009; Love et al., 2009; Hoffman et al., 2017).

## 2.2 Snowball Earth hypothesis

This section presents the Snowball Earth hypothesis from the perspective of climate dynamics. It begins with a review of the Budyko-Sellers Energy Balance Model (EBM) (Budyko, 1969; Sellers, 1969). Then, the physical characteristics of the Snowball Earth cycle are explained. Finally, it is discussed how this energy balance model is able to explain the geological evidence and what open questions remain. It is concluded that the survival of life is an open question that motivates the waterbelt hypothesis. This section is based on the review papers North (1975) and Walsh and Rackauckas (2015), as well as Hörner and Voigt (2025).

### Budyko-Sellers Energy Balance Model

The model considers the energy balance at the Top of Atmosphere (TOA) dependent on the latitude $\varphi$. The latitude $\varphi$ is expressed by the variable $x = \sin\varphi$, with $x \in [0, 1]$ or $\varphi \in [0°, 90°]$. This is done for convenience, as the area of an infinitesimal latitude strip at $\varphi$ is proportional to $\sin\varphi$. The TOA energy balance is then given by:

$$\frac{Q}{4}s(x)(1-\alpha(T(x))) = A + BT(x) + C(T(x) - \overline{T}). \tag{2.1}$$

The left side of the equation describes the shortwave energy balance. $Q$ is the solar constant and $s(x)$ describes the zonal distribution of incoming solar radiation. It is determined by the orbital parameters of Earth, approximated with a second Legendre polynomial (North, 1975):

$$s(x) = 1 - 0.482\frac{3x^2 - 1}{2}. \tag{2.2}$$

$\alpha$ is the TOA albedo, determined by the surface albedo as well as the albedo of clouds and the clear sky atmosphere. It is dependent on the surface temperature at each latitude $T(x)$. The right side describes the longwave energy balance. $A + BT(x)$ is a linearization of the Stefan-Boltzmann law, governing the outgoing longwave radiation. $C(T(x) - \overline{T})$ is a representation of the meridional heat transport, dependent on the global mean temperature $\overline{T}$.

The Earth is then assumed to be ice covered from the poles down to an ice-edge latitude of $x = x_i$, and ice-free from the ice-edge latitude $x_i$ to the equator. At the ice-edge latitude itself, surface temperature is set to a critical threshold temperature of ice formation $T(x_i) = T_i$.

From the definition of the ice-edge latitude and the surface temperature, the albedo $\alpha$ is determined. Above the critical temperature, equatorward of the ice edge, the ocean is ice-free and has a low albedo $\alpha_0$. Below the critical temperature, poleward of the ice edge, the ocean is ice-covered and thus has a high albedo $\alpha_i$. At the ice edge itself, a transition albedo is used.

$$\alpha(T(x)) = \begin{cases} \alpha_0 & T > T_i \\ \tilde{\alpha} = \frac{\alpha_0 + \alpha_i}{2} & T = T_i \\ \alpha_i & T < T_i \end{cases} \tag{2.3}$$

Equation 2.1 is integrated globally, resulting in the global energy balance

$$\frac{Q}{4}(1 - \alpha_p(x_i)) = A + B\overline{T} \tag{2.4}$$

with the planetary albedo $\alpha_p$

$$\alpha_p(x_i) = \int_0^{x_i} \alpha_0 s(x) dx + \int_{x_i}^1 \alpha_i s(x) dx. \tag{2.5}$$

Now, Equation 2.1 is solved at the ice-edge $x = x_i$ and substituted into Equation 2.4 to eliminate $\overline{T}$. The model can then be solved either for the shortwave radiation $Q$, or for the longwave radiative forcing $A$. Here, we are doing the latter:

$$A(x_i) = \frac{1}{1+\frac{C}{B}} \left[ \frac{Q}{4} \left( S(x_i)(1-\tilde{\alpha}) + \frac{C}{B}(1-\alpha_p(x_i)) \right) - (B+C)T_i \right]. \qquad (2.6)$$

Ultimately, this equation addresses the question: What amount of longwave radiative forcing $A$ is necessary to achieve equilibrium TOA energy balance when the Earth is ice covered from the poles to the latitude $x_i$? Solving for all possible ice-edge latitudes $x_i \in [0, 1]$ reveals a saddle-node bifurcation: The model exhibits a bistability, which can explain the Snowball Earth cycle (Figure 2.1).

### The Snowball Earth hysteresis loop

The black line in Figure 2.1 depicts the solution of the Budyko-Sellers EBM (Equation 2.6), demonstrating the bistability of Earth's climate. Over a range of longwave radiative forcing $\Delta A$, multiple solutions exist: Two of them are stable (solid lines) and one is instable (dashed line). On the one hand, there is a solution with an ice-edge at high latitudes, the temperate or ice-free climate. On the other hand, a stable solution exists with an ice-edge latitude at 0°, the Snowball Earth. The unstable solution is a separatrix between the attractor basins of the two stable solutions.

Following the blue numbers in Figure 2.1, the Snowball Earth hysteresis is explained. For further details on the feedback process in the Snowball EBM, we refer to Roe and Baker (2010).

1. Starting from a temperate climate, a reduction in the longwave radiative forcing leads to falling temperatures and hence greater ice cover. During the Cryogenian this was caused by a decrease in atmospheric $CO_2$ due to silicate weathering and carbon burial (see section 2.1). The climate has a stable solution until a critical radiative forcing is reached: the tipping point. For radiative forcings below this value, there is no temperate solution, only the Snowball Earth solution.

2. Earth's climate thus transitions from the temperate to the Snowball Earth solution. This transition corresponds to the runaway ice-albedo feedback. Increasing ice cover results in a larger albedo and thus lower temperatures,

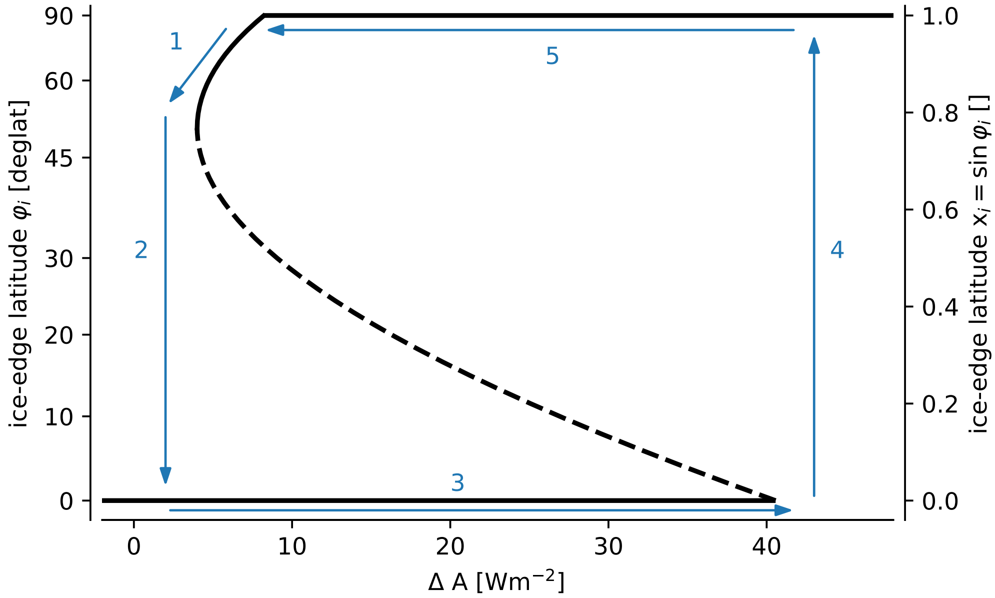


**Fig. 2.1:** Bifurcation diagram of the Budyko-Sellers model. Solid black lines indicate stable solutions, dashed lines unstable solutions. Blue arrows demonstrate the phases of the Snowball cycle. The longwave forcing on the x-axis is expressed as difference to a reference forcing $\Delta A = A_0 - A$, with $A_0 = 210\,\mathrm{W\,m^{-2}}$. Parameters as in Abbot et al. (2011): $B = 1.5\,\mathrm{W\,m^{-2}\,K^{-1}}$, $C = 3.75\,\mathrm{W\,m^{-2}\,K^{-1}}$, $Q = 1285\,\mathrm{W\,m^{-2}}$, $\alpha_0 = 0.3$, $\alpha_i = 0.6$, $T_i = -10\,°\mathrm{C}$.

which is the destabilizing ice-albedo feedback. Conversely, lower temperatures result in less outgoing longwave radiation, which is the stabilizing Planck feedback. The tipping point is characterized by the destabilizing ice-albedo feedback becoming larger than the stabilizing Planck feedback. Thus, with lower radiative forcing, ice cover increases and temperatures fall until ice cover reaches its practical limit: Snowball Earth.

3. In the Snowball Earth, the ice-albedo feedback is stopped, so the climate is stable. Increasing radiative forcing does not change the ice cover initially, the climate is trapped in the "ice catastrophe" as described by Budyko (1969). This changes only when radiative forcing is significantly increased until it passes another tipping point. In the Cryogenian, the increase of radiative forcing resulted from natural $CO_2$ outgassing of the Earth, and the cessation of silicate weathering.

4. As the radiative forcing increases past the deglaciation tipping point, the runaway ice-albedo feedback occurs in the opposite direction. This results in geologically rapid deglaciation of the Earth until the new stable equilibrium

is reached: a completely ice-free "hothouse" climate with large amounts of atmospheric $CO_2$.

5. Now the climate is in a postglacial hothouse state. The extreme amount of atmospheric $CO_2$ is reduced by the fast deposition of cap carbonates. The resulting decrease in radiative forcing does initially not lead to a growth in sea ice, as temperatures are still high. When temperatures are low enough for ice to form at the poles, the hysteresis loop is closed.

**Initiating the Snowball hysteresis loop**

Following the line of reasoning of the previous section, one would expect that this hysteresis loop, once started, would continue indefinitely. However, this is clearly not the case. According to the geological evidence, the Earth went through the Snowball Cycle twice in the Cryogenian, in a time span of about 80 Ma (Hoffman et al., 2017). Before that, a Snowball Earth event probably occurred at the time of the Great Oxidation Event, almost 2 billion years before the Cryogenian, at the beginning of the Proterozoic (Hoffman et al., 2017). And since the end of the Cryogenian, there has been no Snowball Earth. What was so special about the Cryogenian that led to two Snowball Earth events?

According to Pierrehumbert et al. (2011), there is no complete mechanism that can explain the absence of Snowball Earth events during the "boring billion" between the Great Oxidation Event and their reoccurrence in the Cryogenian. However, there are a number of arguments that explain why the Cryogenian was the optimal period for Snowball Earth to occur, and why it did not occur thereafter.

The Sun's luminosity increases over time, and during the Cryogenian it was about 5 % less than today (Gough, 1981). This acts as a background forcing, inhibiting the initiation of a Snowball Earth in more recent climates. In addition, land plants and carbonate precipitating plankton appeared later than the Cryogenian, and both features inhibit the drawdown of atmospheric $CO_2$ and thus the initiation of a Snowball Earth (Pierrehumbert et al., 2011). Land plants enhance the silicate weathering thermostat (Brady & Carroll, 1994), and plankton provide an additional buffer for ocean acidity (Ridgwell et al., 2003). Finally, as explained in section 2.1, the breakup of the supercontinent Rodinia caused a drawdown of atmospheric $CO_2$ during the Cryogenian, favoring the initiation of a Snowball Earth (Pierrehumbert et al., 2011).

### Survival of life

An argument that challenges the Snowball Earth hypothesis is the survival of life. Photosynthetic eukaryotes and cyanobacteria (Waldbauer et al., 2009; Knoll, 1992; Pierrehumbert et al., 2011) existed before and after the Snowball Earth, and they need sunlight penetrating into the ocean in order to survive. Additionally, sponges, one of the first forms of complex animals, survived through the Snowball Earth (Brocks & Butterfield, 2009; Love et al., 2009; Hoffman et al., 2017). The survival of these life forms provides a strong counter argument against the runaway ice-albedo feedback as described in the Budyko-Sellers EBM. Multiple solutions have been brought up for this.

It has been hypothesized that sea ice near the equator or in protected inland seas was thin enough for sunlight to penetrate and allow phototrophic life to survive (McKay, 2000; Pollard & Kasting, 2005). Sunlight penetrating the ice provides a heating rate large enough to offset freezing from below. In addition, the negative Precipitation minus Evaporation (P-E) balance at the equator due to the large seasonal cycle of the Intertropical Convergence Zone (ITCZ) in a Snowball Earth can assist the melting (Pierrehumbert et al., 2011). However, this solution might only be possible only for a very specific choice of parameters in idealized models, limited especially by the dynamic ice flow of thick sea glaciers in higher latitudes (Pierrehumbert et al., 2011; Pollard & Kasting, 2006).

An alternative hypothesis is the survival of life in small refugia. Phototrophic life could survive in cryoconite meltwater ponds on the ice (Vincent et al., 2000; Hoffman, 2016). These ponds or holes in the ice are the result of dust accumulating on the ice, reducing the surface albedo and resulting in the formation of meltwater ponds. In today's polar regions, cryoconite holes harbor life in the summer, but freeze over in winter. In a Snowball Earth, cryoconite holes in the ice near the equator may have contained meltwater throughout the year, providing a refugia for phototrophic life (Hoffman et al., 2017).

However, the survival of sponges remains difficult to reconcile with the Snowball Earth hypothesis (Hoffman et al., 2017; Hoffman, 2016; Pierrehumbert et al., 2011). Cryoconite holes are not a suitable habitat for the sponges that existed during the Cryogenian, neither is the high salinity environment of a fully ice-covered ocean. Thus, the survival of sponges remains a challenge for the Snowball Earth hypothesis (Hoffman et al., 2017; Pierrehumbert et al., 2011).

### Alternative scenarios

Due to the difficulties of reconciling the geological evidence with the survival of life, a number of alternative scenarios to the Snowball Earth have been proposed. In this subsection, a short overview of these scenarios is provided, based on a review by Fairchild and Kennedy (2007).

Eyles and Januszczak (2004) coined the term zipper rift Earth. In this scenario, the breakup of Rodania led to rifting, which enabled the formation of glaciers on rift shoulders. Glacial deposits are then preserved in rift basins. This scenario does not include a runaway ice-albedo feedback. However, this hypothesis fails to explain the global prevalence of cap carbonates (Fairchild & Kennedy, 2007).

Another explanation for tropical glaciers at sea level could be a high obliquity Earth, as suggested by Williams (1975). With increasing obliquity, the poles receive more solar radiation and the equator receives less. At an obliquity of 54°, the meridional temperature gradient is reversed and the poles are warmer than the equator in the annual mean (Ward, 1974). This would allow for the formation of glaciers at sea-level at the equator without a global glaciation.

However, several arguments have been put forward against the high-obliquity hypothesis. Most importantly, there is no known mechanism that could change the Earth's obliquity sufficiently (Kirschvink, 1992). Due to the gravitational coupling of the Earth-Moon system, possible changes in the Earth's obliquity are limited compared to other planets (Fairchild & Kennedy, 2007). In addition, a high-tilt Earth would have an extreme seasonal climate, for which there is no geological evidence (Fairchild & Kennedy, 2007). Also, in a high tilt scenario, glaciers would be confined to low latitudes, which cannot explain the global occurrence of cap carbonates overlying glacial deposits (Kirschvink, 1992).

Finally, waterbelt states are an alternative hypothesis that proposes that Earth was close to a Snowball state, with ice cover stretching from the poles to low latitudes, but with open ocean remaining near the equator (Hyde et al., 2000; Abbot et al., 2011; Rose, 2015). This hypothesis is an attractive alternative, as it can potentially reconcile the geological evidence with the survival of life. It is discussed in detail in the following sections.

## 2.3 Waterbelt states

This sections provides an overview of waterbelt states in the literature. The overview is largely based on Hoffman et al. (2017) and Catling and Kasting (2017). Additionally, the reader is referred to the literature review on waterbelt states in the PhD thesis of Braun (2022).

For waterbelt states to be a valid explanation for the geological evidence, they have to fulfill four criteria.

1. Open ocean water in the tropics. This provides a robust solution for the survival of complex life (Hyde et al., 2000; Abbot et al., 2011).
2. Ice cover that is large enough to explain the evidence of active glaciers in the tropics. According to Rodehacke et al. (2013), with an ice-edge latitude at 20° or lower, tropical temperatures would be low enough for glaciers to form on mountains on tropical continents. These glaciers can stretch to the ocean and lead to the formation of glacial deposits there.
3. There has to be a hysteresis between the waterbelt state and the temperate state. This is a necessary requirement in order to explain the large $CO_2$ content that leads to the formation of cap carbonates. With associated hysteresis, the $CO_2$ has to increase significantly for deglaciation to occur. Without hysteresis, the climate would return to its original state when $CO_2$ is increased to its original value.
4. The waterbelt state must be accessible from a temperate state by a reduction in radiative forcing. This means that the lower end of the stable temperate state must have higher values of radiative forcing than the lower end of the stable waterbelt state. If this is not the case, there is no realistic scenario for Earth to reach this state from a temperate state.

Early studies with simple climate models showed stable states with open water in the tropics (Hyde et al., 2000; Crowley et al., 2001). However, these states had only a small hysteresis associated with them, which would make them unable to explain the high postglacial $CO_2$ content. Due to the lack of hysteresis, these solutions are sometimes called "soft Snowball" or "Slushball" in the literature. However, the naming is not consistent in the literature, a discussion on the naming of climate states is provided in chapter 4.

Two types of waterbelt states have been found that can potentially satisfy all requirements. These are waterbelt states stabilized by ocean heat transport

(Rose, 2015) and waterbelt states stabilized by bare sea ice in the subtropics, the Jormungand mechanism (Abbot et al., 2011).

Rose (2015) found a waterbelt state using the MITgcm model. They used an aquaplanet configuration with a dynamic ocean and without sea-ice dynamics. This setup resulted in a stable waterbelt state with a large hysteresis. The climate is prevented from reaching a Snowball Earth by a wind-driven ocean circulation that converges energy from the equator to the ice edge at low latitudes. In contrast, the Jormungand mechanism is a purely atmospheric mechanism.

## 2.4 Jormungand mechanism

The Jormungand mechanism was proposed by Abbot et al. (2011). When sea ice advances into low-latitudes, it comes into the subtropical desert regions. Here, the descending branch of the Hadley cell results in a negative P-E balance. This leads to net surface ablation, resulting in melting of the snow cover on ice and the exposure of the bare sea ice underneath. Bare sea ice can have a significantly lower surface albedo than snow (Warren et al., 2002; Dadic et al., 2013). Thus, the exposure of dark bare sea ice can weaken the ice-albedo feedback and stabilize the climate with an ice-edge latitude between 5°-15° (Abbot et al., 2011). This can be demonstrated with an adapted Budyko-Sellers EBM.

#### Jormungand mechanism in the Budyko-Sellers EBM

Based on the EBM described in section 2.2, an additional assumption is made, following Abbot et al. (2011). The albedo of ice $\alpha_i$ can change between a high value of snow-covered sea ice $\alpha_i^s$ and a low value of bare sea ice $\alpha_i^i$. When ice reaches a certain threshold latitude of $x_s$, ice is assumed to change from snow-covered to bare over a transition region of $\Delta x_s$:

$$\alpha_i(x) = \alpha_i^i + \left(\frac{\alpha_i^s - \alpha_i^i}{2}\right)\left(1 + \tanh\left(\frac{x - x_s}{\Delta x_s}\right)\right). \tag{2.7}$$

With this equation substituted into Equation 2.3, the model can be solved as before. Depending on the choice of parameters, an additional stable solution appears: the Jormungand state (Figure 2.2). The Jormungand state has an

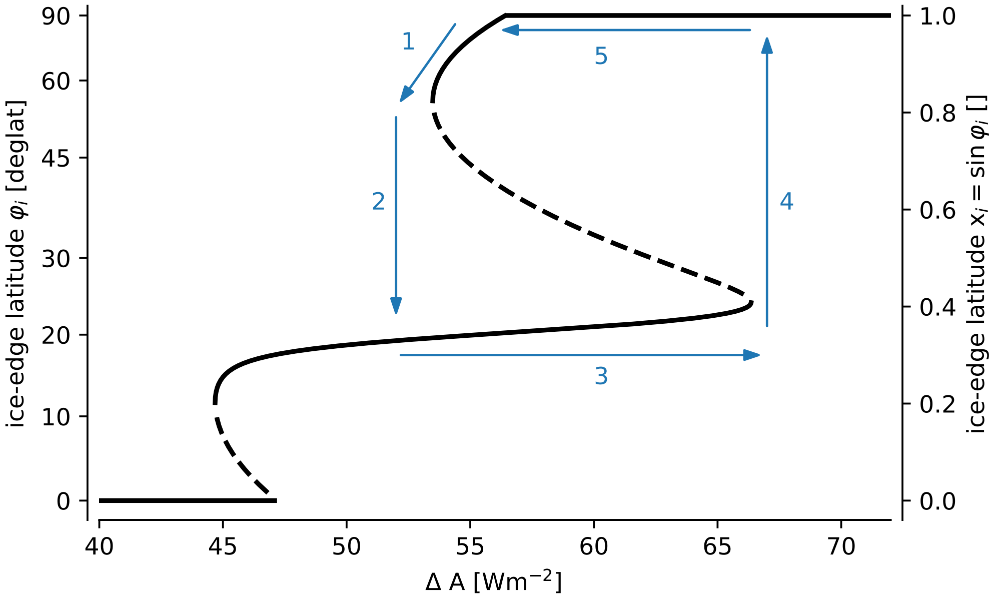


**Fig. 2.2:** Bifurcation diagram of the Budyko-Sellers model with Jormungand adaptation. Solid black lines indicate stable solutions, dashed lines unstable solutions. Blue arrows demonstrate the phases of the Snowball cycle. The longwave forcing on the x-axis is expressed as difference to a reference forcing $\Delta A = A_0 - A$, with $A_0 = 210\,\mathrm{W\,m^{-2}}$. Parameters as in Abbot et al. (2011): $B = 1.5\,\mathrm{W\,m^{-2}\,K^{-1}}$, $C = 2.25\,\mathrm{W\,m^{-2}\,K^{-1}}$, $Q = 1285\,\mathrm{W\,m^{-2}}$, $\alpha_0 = 0.35$, $\alpha_i^i = 0.45$, $\alpha_i^s = 0.8$, $x_s = 0.35$, $\Delta x_s = 0.04$, $T_s = 0\,°\mathrm{C}$.

additional hysteresis associated with it, which can provide an explanation for the Snowball Earth evidence:

1. As in the default Budyko-Sellers EBM, a reduction of atmospheric $CO_2$ in a temperate climate leads to the passing of a tipping point.

2. Once the tipping point is passed, increasing ice cover, decreasing surface albedo and falling temperatures represent a runaway ice-albedo feedback. However, as the ice edge reaches lower latitudes, the negative P-E balance caused by the descending branch of the Hadley cell leads to the exposure of bare, dark sea ice. The lower albedo of the ice at these latitudes weakens the ice-albedo feedback, and the climate stabilizes in a waterbelt state with open water near the equator.

3. The waterbelt state has a significant hysteresis associated with it. Thus, an increase in radiative forcing is required in order for deglaciation to occur. The large ice-cover and the existence of tropical land glaciers provide an argument for the cessation of silicate weathering (Abbot et al., 2011). Due

to this, natural outgassing of $CO_2$ can provide a mechanism that slowly increases longwave radiative forcing, until the tipping point of deglaciation is passed.

4. & 5. Starting from the deglaciation tipping point, the Snowball cycle is the same as in the default Budyko-Sellers EBM. Most notably, the hysteresis of the waterbelt state also results in a post glacial hothouse climate with high atmospheric $CO_2$, which is able to explain the formation of cap-carbonates.

The Jormungand hypothesis thus provides an attractive alternative explanation for the Cryogenian glaciations. Open water in the tropics provides a robust environment for the survival of life. Near global ice cover explains the existence of tropical land glaciers. And the hysteresis explains the high atmospheric $CO_2$ required for the formation of cap carbonates. However, for the Jormungand hypothesis to be a robust solution for the Snowball Earth scenario, it has to be reproducible in climate models.

#### Jormungand mechanism in climate models

A waterbelt state stabilized solely by the Jormungand mechanism was first shown by Abbot et al. (2011), who used the atmospheric models CAM and ECHAM5 in an aquaplanet setup without ice dynamics and with a mixed-layer ocean, neglecting ocean energy transport. In CAM, a stable and accessible waterbelt state with associated hysteresis appeared when applying surface albedo values of 0.45 for bare ice and 0.79 for cold snow. This state clearly showed features of the Jormungand mechanism, with bare sea ice weakening the ice-albedo feedback in low latitudes. In ECHAM5, snow on sea ice was not explicitly resolved. The Jormungand mechanism was thus approximated by letting sea ice take on the higher, snow covered value at latitudes poleward of 20°, and the lower, bare ice value at latitudes equatorward of 20°. These settings also resulted in a stable and accessible waterbelt state with hysteresis.

Voigt and Abbot (2012) investigated the Jormungand mechanism in a more realistic setup, using the ECHAM5/MPI-OM model with Marinoan continents, a dynamic ocean and dynamic sea ice. Here, the Jormungand mechanism proved to be less robust. There was no waterbelt state when sea ice dynamics where active. The viscous spreading of thicker sea ice from higher to lower latitudes and the equatorward wind drag on sea ice destabilized a low-latitude sea-ice edge. Deactivation of sea-ice dynamics in Voigt and Abbot (2012) resulted in a stable low-latitude sea-ice edge. However, this state was a soft snowball rather than a waterbelt state, as there was no hysteresis between the state with a low-latitude sea-ice edge and the temperate state.

Yang et al. (2012a, 2012b, 2012c) found states with a low-latitude sea-ice edge in CCSM3 and CCSM4. Their setup included ocean dynamics as well as sea-ice dynamics, with modern continents. These models featured the Jormungand mechanism, sea ice was bare equatorward of 18°, weakening the ice-albedo feedback. However, these states were not explicitly tested for hysteresis, thus they are considered soft Snowball states instead of waterbelt states.

More recently, Braun et al. (2022a) postulated that clouds can have a significant influence on the stability of waterbelt states by masking the ice-albedo feedback. As sea ice advances into latitudes where TOA albedo is already high due to large cloud cover, the ice-induced increase in surface albedo has a diminishing effect on TOA albedo. Thus, the ice-albedo feedback is weakened by the presence of clouds. This was demonstrated with the atmospheric models CAM and ICON. In contrast to CAM, ICON did not show an accessible waterbelt state, which was due to the fact that ICON simulated less mixed-phased clouds in the subtropics. Braun et al. (2022a) concluded that the uncertainties related to clouds in a Cryogenian climate contribute substantially to the inconsistencies of waterbelt states in different climate models.

In summary, the Jormungand mechanism and its impact on the stability of waterbelt states is still a subject of debate. Climate models show different results for the strength of the Jormungand mechanism and its relevance for the stability of waterbelt states. This thesis aims to address this issue by investigating the Jormungand mechanism in idealized models and developing a framework that allows a quantification of the impact of bare sea ice and clouds on waterbelt state stability.

# Research questions

# 3

This thesis aims to reduce uncertainties associated with the Jormungand mechanism by analyzing the processes that determine its influence on the stability of waterbelt states. First, the strength of the Jormungand mechanism itself, i.e. the existence of subtropical bare sea ice, is analyzed with respect to the sea-ice model used. Second, the shortwave cloud feedback and its interaction with the ice-albedo feedback via cloud masking are investigated. Third, the methods developed in the first two parts are applied to a larger dataset from different climate models. Thus, this thesis answers three overarching research questions:

**RQ1: How robust is the Jormungand mechanism with respect to different sea-ice models?**

The Jormungand mechanism is based on the assumption that snow cover on sea ice melts as it comes under the influence of the descending branch of the Hadley cell, revealing the darker bare sea ice underneath and weakening the ice-albedo feedback (Abbot et al., 2011). However, the melting of sea ice and snow in climate models depends on the sea-ice model used, especially with respect to vertical resolution. Abbot et al. (2010) showed that low vertical resolution of sea ice increases surface melting of ice, due to the poorly resolved diurnal surface temperature cycle. Thus, low vertical resolution enhanced the deglaciation of Snowball Earth. In addition, Yang et al. (2012a) observed a stronger ice-albedo feedback in simulations of Snowball Earth initiation when vertical resolution of sea ice was increased. More recently, a study by the author (Hörner et al., 2022) showed that increasing vertical resolution facilitates Snowball Earth initiation.

Many climate models used to study the Jormungand mechanism have used so-called "0-layer" sea-ice models that neglect the heat capacity of sea ice, such as the ECHAM model in Voigt and Abbot (2012), Abbot et al. (2011), and Voigt and Marotzke (2010), as well as the ICON model in Braun et al. (2022a). These simple sea-ice models may overestimate surface melting and thus overestimate the strength of the Jormungand mechanism. In chapter 5, the first research question therefore tests how different sea-ice models, a 0-layer model (Semtner,

1976) and a 3-layer model (Winton, 2000), affect the Jormungand mechanism and the stability of waterbelt states.

**RQ2: What is the contribution of the Jormungand mechanism, cloud masking, and cloud radiative feedback for the stability of waterbelt states?**

Cloud radiative effects can influence the stability of waterbelt states in multiple ways. First, as cloud properties change during a climate transition, they induce radiative feedbacks (Voigt & Marotzke, 2010; Eisenman & Armour, 2024). Second, they mask the ice-albedo feedback (Braun et al., 2022a). The shortwave cloud radiative effect weakens the ice-albedo feedback of ice growing beneath the clouds. Braun et al. (2022a) thus postulated that optically thick subtropical clouds are required in order to simulate a stable waterbelt state.

In addition to the Jormungand mechanism, cloud masking and cloud radiative feedback thus pose a group of factors that can determine the stability of the climate. The second research questions in chapter 6 decomposes the influence of these 3 factors on waterbelt hysteresis. For this purpose, a new method is defined to calculate the 3 factors directly from model output and decompose their influence on waterbelt stability.

**RQ3: Can the inter-model differences in waterbelt state stability be explained by the sum of contributions of the Jormungand mechanism, cloud masking, and cloud feedback?**

The stability of waterbelt states is extremely model dependent. On the one hand, waterbelt states in the CAM model tend to be stable, accessible and associated with a large hysteresis (Abbot et al., 2011; Braun et al., 2022a). On the other hand, waterbelt states in ICON are often only associated with a small hysteresis or not accessible (chapter 5, chapter 6, Hörner et al. (2022) and Braun et al. (2022a)).

Differences in cloud cover and cloud optical thickness have been proposed as the reason for these large inter-model differences in Braun et al. (2022a). The results of RQ1 in chapter 5 on the other hand suggests that differences in the sea-ice model are responsible. The method developed for RQ2 in chapter 6 allows for the decomposition of the shortwave feedback into the clear-sky ice albedo feedback, cloud masking and cloud feedback. RQ3 compares a large set of simulations from different generations of the ICON and CAM model and analyzes the influence of these factors on waterbelt stability.

# 4 Methods

This chapter provides an overview of the methods used in the papers of this thesis and introduces important research approaches. For a detailed description of the methods, the reader is referred to the corresponding section in the papers in chapters 5, 6 and 7.

## 4.1 Distinction between climate states

The distinction and naming of climate states is not uniform in the literature. To avoid misunderstandings, this section provides a discussion on the distinction and naming of climate states, and defines how these terms are used in this thesis.

A climate state can be defined inductively by its physical properties, such as its global mean temperature or its ice-edge latitude. By this definition, a temperate climate, a hard Snowball and a waterbelt state are different climate states, because their ice-edge latitude is different. A waterbelt state and a soft Snowball however would be the same climate state, as both exhibit a low-latitude sea-ice edge. In the context of Snowball Earth, this is a good definition when examining geological evidence. Because the geological evidence primarily provides information about the physical properties of the climate, and only indirectly about the mechanisms in the climate system.

Conversely, a climate state can be defined deductively by the mechanism that is responsible for its existence. Examples are the Jormungand state in (Abbot et al., 2011) and the waterbelt state in Rose (2015). While their physical properties are similar, both show an ice-edge latitude near the equator, they are stabilized by different processes. The Jormungand state on the one hand is stabilized by bare sea-ice, with no ocean heat transport implemented in the model. And the waterbelt state in (Rose, 2015) on the other hand is stabilized by ocean heat transport, with all ice covered in snow. Thus, although they might be considered the same climate states by an inductive definition, they are different climate states by a deductive definition.

In this thesis, we use a combined approach for defining the different climate states. A waterbelt state is a climate with an ice-edge latitude equatorward of 30°, which is separated via hystereses from a temperate climate as well as a hard Snowball. In contrast, a soft Snowball is a climate state with an ice-edge latitude equatorward of 30°, which is not separated via hysteresis from a temperate climate.

The differences between waterbelt state and soft Snowball are visualized with the Budyko-Sellers EBM in Figure 4.1. Both the waterbelt state solution (blue line) as well as the soft Snowball solution (green line) lead to a climate with an ice-edge latitude equatorward of 30°. At their intersection, both exhibit the same ice-edge latitude given the same radiative forcing. However, while the waterbelt solution is separated from the temperate state by hysteresis, the soft Snowball solution lies on the same stable branch that extends to a temperate and ice-free climate. Thus, the soft Snowball solution does not offer an explanation for the high atmospheric $CO_2$ in a post-glacial climate.

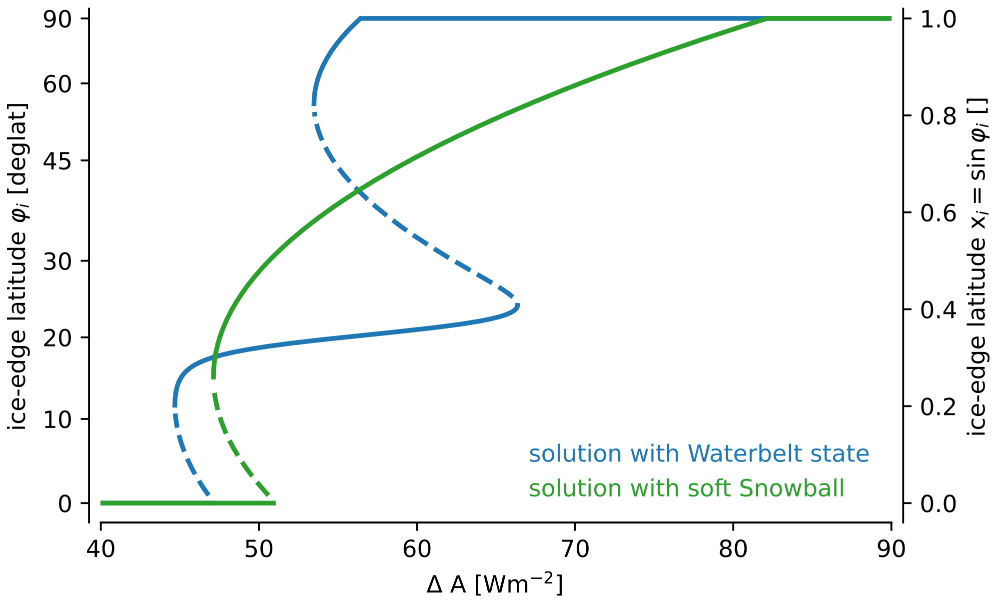


**Fig. 4.1:** Two solutions of the Budyko-Sellers EBM. The blue line shows a solution with the Jormungand adaptation that results in a waterbelt state: a stable state with low ice-edge latitude and a hysteresis. The green line shows a solution without the Jormungand adaptation, but parameters chosen in such a way that a hypothetical soft Snowball state appears: a stable state with low ice-edge latitude but without hysteresis. Parameters for the blue line as in Figure 2.2, and for the green line: $B = 1.5\,\mathrm{W\,m^{-2}\,K^{-1}}$, $C = 1.5\,\mathrm{W\,m^{-2}\,K^{-1}}$, $Q = 1285\,\mathrm{W\,m^{-2}}$, $\alpha_1 = 0.45$, $\alpha_2 = 0.6$, $T_s = 0\,°\mathrm{C}$.

Lastly, a Jormungand state is a waterbelt state that is stabilized solely by the Jormungand mechanism. This is in contrast to e.g. the waterbelt state of Rose (2015), which is stabilized solely by ocean heat transport. This thesis focuses on Jormungand states and the mechanisms responsible for their existence. In fact, the models used in this thesis are by design unable to simulate a waterbelt state as in Rose (2015), as they do not include ocean heat transport.

As the distinction between a Jormungand state and other waterbelt states is dependent on the mechanisms involved, the difference between these states may only exist in idealized models. In a more complex model with more climatic features, multiple mechanisms may interact to stabilize a waterbelt state. This would make it difficult to identify a single process responsible for stabilizing the waterbelt state, and thus render a deductive definition of the climate state impossible.

## 4.2 From EBM to GCM: the model hierarchy

In this thesis, models of varying complexity are employed. They range from the idealized Energy Balance Models (EBMs) as described in chapter 2 to General Circulation Models (GCMs). The goal of this approach is to construct a hierarchy of models with increasing complexity as well as increasing number of represented processes. With this so-called process hierarchy (see Maher et al., 2019), the processes of interest can be implemented one after another and in an increasingly realistic way.

The simplest model used is the Budyko-Sellers EBM to demonstrate the Snowball Earth bistability (section 2.2). The advantage of such a simple model is that it can be solved analytically, and thus can be used to test large ranges of the parameter space. Abbot et al. (2011) extended this model with a representation of the Jormungand mechanism, which lead to the stable Jormungand state (section 2.3). In chapter 6, this model is further extended by a representation of cloud radiative feedback and masking. With this model hierarchy of simple EBMs, the different processes and their impact on waterbelt stability can be described.

#### GCM setup

The next step in model complexity in this thesis are atmospheric GCMs. They provide a much more realistic representation of Earth's climate, because they resolve the dynamics of the atmosphere. The setup is similar to that of Abbot et al. (2011), who firstly postulated the Jormungand mechanism. In the following, the setup is described, with an explanation why certain idealizations where made.

We apply a mixed-layer ocean of 50 m depth, where the sea-surface temperature at each grid point is determined solely by the surface energy balance and the heat capacity of the ocean column. In this setup, ocean dynamics and ocean heat transport is neglected. This is a significant idealization, as ocean heat transport is well known to affect the stability of waterbelt states (Poulsen et al., 2001; Voigt & Abbot, 2012; Rose, 2015). The reason for this idealization is that it allows us to analyze the influence of the Jormungand mechanism on waterbelt stability isolated from influences of the ocean.

The models are run in an aquaplanet setup without continents, which results in a zonally symmetric global atmospheric circulation. This neglects the influence of continents and their topography on the atmospheric circulation (Y. Liu et al., 2018). An aquaplanet setup is often applied when simulating Snowball Earth (see Feulner et al., 2023), it is an alternative to using a reconstructed Neoproterozoic continental configuration (e.g., Voigt et al., 2011; Yang et al., 2012a; Y. Liu et al., 2013) or a present-day continental configuration (e.g., Voigt & Marotzke, 2010; Y. Liu et al., 2018). The caveat of using Neoproterozoic continents is the high uncertainty associated with Neoproterozoic topography (Merdith et al., 2017), and present-day continents are naturally unrepresentative. The aquaplanet setup is thus a compromise that provides an idealized representation of atmospheric processes without introducing additional uncertainties.

Sea ice is represented by thermodynamic models that neglect sea-ice dynamics and horizontal heat transport. While sea-ice dynamics are known to influence the stability of waterbelt states (Voigt & Abbot, 2012), we neglect them to isolate the atmospheric Jormungand mechanism. In addition, the simulation of sea-ice dynamics significantly increases the required runtime of the simulations due to the long timescales of sea-ice dynamical processes.

Surface albedo of snow-covered and bare sea ice is set to 0.79 and 0.45, respectively. These are the same values as in Abbot et al. (2011). While these values are derived from measurements (Warren et al., 2002; Dadic et al., 2013), they are dependent on the atmospheric conditions, melt-ponds, cracks and bubbles in the ice, as well as dust on ice. The albedo value for bare ice is thus at the low end of the range suggested by measurements (Webster & Warren, 2022), and it is chosen to support the the strength of the Jormungand mechanism.

The orbital parameters of Earth are set to zero eccentricity and present-day obliquity of 23.5°, as well as a standard day length of 24 h. These are commonly used parameters because they are similar to today's. It should be noted that changes in orbital parameters have been shown to influence the initiation and termination of Snowball Earth (Wu & Liu, 2023; Eberhard et al., 2023). The solar constant is set to 1285 $W\,m^{-2}$, which represents the weaker sun during the Neoproterozoic (Gough, 1981).

The well-mixed greenhouse gases are removed from the atmosphere, with the exception of $CO_2$, which is constant over time. Thus, the atmospheric $CO_2$ content is used to vary the radiative forcing and to construct the bifurcation diagram.

In conclusion, we apply an idealized atmospheric GCM setup. This allows to analyze the Jormungand mechanism in an environment where the atmosphere is represented in a relatively realistic way, but other processes known to influence the stability of the waterbelt state, such as ocean heat transport and sea-ice dynamics, are still neglected. With this, the influence of the Jormungand mechanism can be isolated, and the results provide a baseline for studies with an increasingly realistic setup.

## 4.3 ICON

The ICON (ICOsahedral Non-hydrostatic) model is a framework for climate modeling and numerical weather prediction developed by the Max Planck Institute for Meteorology (MPI-M), the German Weather Service (DWD), the Karlsruhe Institute of Technology (KIT), and the Center for Climate Systems Modeling (C2SM). It consists of different models for atmosphere, ocean and land. It uses an icosahedral-triangular Arakawa C grid, which allows for a wide range of resolutions (Zängl et al., 2015).

In this thesis, the atmospheric model of the ICON framework ICON-A (Giorgetta et al., 2018) is applied in different versions. It uses the atmospheric physics package derived from the previous ECHAM6 model (Giorgetta et al., 2018). The horizontal icosahedral grid has a mean resolution of 158 km. The vertical dimension is described by a terrain following hybrid sigma coordinate in 47 levels up to 80 km, which we reduced in our setup to 45 levels up to 72 km in order to stabilize the model in a cold climate.

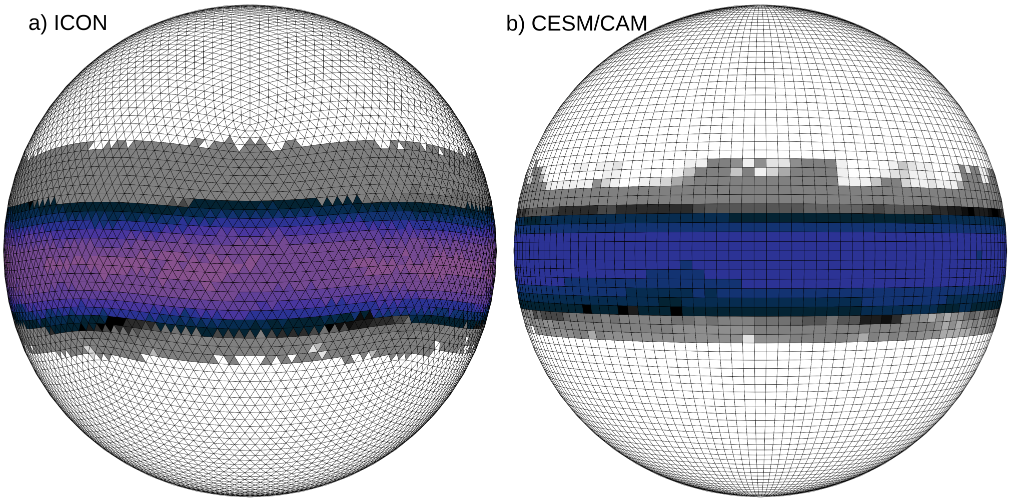


**Fig. 4.2:** Snapshot of a stable waterbelt state in ICON (a) and CESM/CAM (b). Greyscale indicates monthly mean surface albedo of sea ice, colors indicate monthly-mean sea-surface temperature. Black lines show cell boundaries of the irregular ICON grid (a) and the latitude-longitude CAM4 grid (b). Data from chapter 7: a) ICON-ESM 5500 ppmv, April 890, b) CAM4 1200 ppmv, February 267.

Two different thermodynamic sea-ice models are applied: a simple 0-layer Semtner model (Semtner, 1976) and a 3-layer Winton model (Winton, 2000). Whereas the Semtner model neglects the heat capacity of sea ice, the Winton model applies energy-conserving thermodynamics following Bitz and Lipscomb (1999). These models are compared in detail in chapter 5, also see Hörner et al. (2022).

Convection is parameterized by a version of the Tiedtke (1989) mass-flux scheme. Cloud cover is diagnosed from relative humidity following Sundqvist et al. (1989). Radiation is calculated via the PSrad scheme of Pincus and Stevens (2013), which is based on the commonly used Rapid Radiation Transfer Model (RRTM).

## 4.4 CESM/CAM/ExoCAM

The Community Earth System Model (CESM) is a coupled global climate model developed by the National Center for Atmospheric Research (NCAR) (e.g., Danabasoglu et al., 2020). It is the successor of the Community Climate System Model (CCSM). It consists of various models for atmosphere, ocean, land and ice. In chapter 7 of this thesis, we apply the atmospheric model of CESM, the Community Atmosphere Model (CAM), in different versions. These are CAM3

(Collins et al., 2006), CAM4 (Neale et al., 2010), CAM5 (Neale et al., 2012) and ExoCAM (Wolf et al., 2022).

CAM3, CAM4, and CAM5 are later versions of the same model. ExoCAM, as we use it here, is a branch of CAM4 developed for use with exoplanetary atmospheres. The main difference between ExoCAM and CAM is the radiative transfer model. CAM3 is applied with a spectral dynamical core with a nominal horizontal grid spacing of 310 km. CAM4 and CAM5 use the finite-volume dynamical core on a 1.9°x2.5° latitude-longitude grid (see Figure 4.2 b). ExoCAM also uses a finite-volume dynamical core, with a courser horizontal resolution of 4°x5°. CAM3 uses the thermodynamic sea-ice model CSIM, all other versions use the CICE model. The sea-ice models have 5 vertical layers and apply the energy-conserving thermodynamics of Bitz and Lipscomb (1999).

# 5 Sea-ice thermodynamics can determine waterbelt states

The first publication addresses research question 1: How robust is the Jormungand mechanism with respect to different sea-ice models?

Two sets of simulations are performed with the ICON-A model, using a 0-layer Semtner sea-ice model (Semtner, 1976) and a 3-layer Winton sea-ice model (Winton, 2000), respectively. The 0-layer model results in a stable waterbelt state. However, the 3-layer model shows no evidence of a stable waterbelt state. The paper concludes that the 0-layer model overestimates surface melting and thus overestimates the extent of the Bare Sea-Ice Region (BASIR) near the ice edge, which is responsible for stabilizing a waterbelt state. This calls into question the relevance of the Jormungand mechanism for waterbelt states.

This study was designed and written the author and Aiko Voigt. Model setup, simulation runs, data analysis, and visualization were performed by the author. The author's contribution is thus estimated to be about 80%.

The paper was submitted to Earth System Dynamics on 3.9.2023 and published on 15.3.2024.

**Hörner, J., & Voigt, A. (2024). Sea-ice thermodynamics can determine waterbelt scenarios for Snowball Earth. *Earth System Dynamics*, *15*(2), 215–223. DOI:10.5194/esd-15-215-2024**

Earth Syst. Dynam., 15, 215–223, 2024
https://doi.org/10.5194/esd-15-215-2024


Earth System Dynamics
Open Access
EGU

Research article

# Sea-ice thermodynamics can determine waterbelt scenarios for Snowball Earth

**Johannes Hörner and Aiko Voigt**

Department of Meteorology and Geophysics, University of Vienna, Vienna, Austria

**Correspondence:** Johannes Hörner (johannes.hoerner@univie.ac.at)

Received: 9 September 2023 – Discussion started: 4 October 2023
Revised: 22 January 2024 – Accepted: 6 February 2024 – Published: 15 March 2024

**Abstract.** Snowball Earth refers to multiple periods in the Neoproterozoic during which geological evidence indicates that the Earth was largely covered in ice. A Snowball Earth results from a runaway ice–albedo feedback, but there is an ongoing debate about how the feedback stopped: with fully ice-covered oceans or with a narrow strip of open water around the Equator. The latter states are called waterbelt states and are an attractive explanation for Snowball Earth events because they provide a refugium for the survival of photosynthetic aquatic life, while still explaining Neoproterozoic geology. Waterbelt states can be stabilized by bare sea ice in the subtropical desert regions, which lowers the surface albedo and stops the runaway ice–albedo feedback. However, the choice of sea-ice model in climate simulations significantly impacts snow cover on ice and, consequently, surface albedo.

Here, we investigate the robustness of waterbelt states with respect to the thermodynamical representation of sea ice. We compare two thermodynamical sea-ice models, an idealized zero-layer Semtner model, in which sea ice is always in equilibrium with the atmosphere and ocean, and a three-layer Winton model that is more sophisticated and takes into account the heat capacity of ice. We deploy the global icosahedral non-hydrostatic atmospheric (ICON-A) model in an idealized aquaplanet setup and calculate a comprehensive set of simulations to determine the extent of the waterbelt hysteresis. We find that the thermodynamic representation of sea ice strongly influences snow cover on sea ice over the range of all simulated climate states. Including heat capacity by using the three-layer Winton model increases snow cover and enhances the ice–albedo feedback. The waterbelt hysteresis found for the zero-layer model disappears in the three-layer model, and no stable waterbelt states are found. This questions the relevance of a subtropical bare sea-ice region for waterbelt states and might help explain drastically varying model results on waterbelt states in the literature.

## 1 Introduction

The Neoproterozoic glaciations are commonly assumed to be of global extent and have become known under the term "Snowball Earth" (Kirschvink, 1992; Hoffman and Schrag, 2002). A Snowball Earth is initiated by a runaway ice–albedo feedback, where expanding ice, increasing planetary albedo and falling global temperatures compose a feedback loop that leads to rapid glaciation until the Earth is either fully ice-covered or the feedback is stopped by some other stabilizing mechanism (Pierrehumbert et al., 2011).

Climate states where the runaway ice–albedo feedback is stopped with a stable ice border equatorward of 30° have been termed soft Snowball (Hyde et al., 2000; Yang et al., 2012a, b) or waterbelt states (Abbot et al., 2011; Rose, 2015; Brunetti et al., 2019; Ragon et al., 2022; Braun et al., 2022). For waterbelt states to be a feasible explanation for the Cryogenian glaciations, they have to be accessible from a temperate climate state, and they have to be stable over a large range of atmospheric $CO_2$, as only then can they explain the long duration of the Snowball event and the survival of photosynthetic aquatic life (Hoffman et al., 2017). Two major effects have been shown to allow states with low-latitude ice margins: firstly, heat convergence at the sea-ice margin stopping ice growth thanks to the ocean circulation (Rose, 2015) and,

Published by Copernicus Publications on behalf of the European Geosciences Union.

secondly, bare low-albedo sea ice in the subtropics stopping the ice–albedo feedback (Abbot et al., 2011). Here we focus on the latter effect, the Jormungand mechanism.

The Jormungand mechanism is based on the assumption that sea ice will not be covered by snow when it reaches the subtropics, where the descending branch of the Hadley circulation results in net sublimation and evaporation. Consequently, snow melts, and a larger region of darker bare sea ice is exposed, weakening the ice–albedo feedback until a stable state is reached. We refer to this region at the ice margin as the bare sea-ice region (BASIR) in this study. For the BASIR to have an impact on the climate, a strong albedo contrast between dark bare sea ice and bright snow is required (Warren et al., 2002; Dadic et al., 2013). The width of the BASIR then governs the strength of the Jormungand mechanism.

In this study, we assess the robustness of the Jormungand mechanism by examining sea ice and its snow cover in two different thermodynamical sea-ice models. That is, we ask the following question: how robust is the Jormungand mechanism when using different sea-ice schemes? Recently, Braun et al. (2022) also postulated a strong influence of subtropical clouds on waterbelt stability, as the optical thickness of subtropical clouds determines the strength of the ice–albedo feedback when ice grows beneath the clouds. The stabilizing effect of clouds over ice is an overarching effect, as clouds mute the ice–albedo feedback. Here, however, we isolate the effect of the sea-ice scheme on the ice–albedo feedback.

Abbot et al. (2010) showed that using more sea-ice layers generally reduces surface melting by reducing the "melt-ratchet" effect. This is because simple thermodynamic sea-ice models overestimate the daily and seasonal cycle of surface temperature and consequently overestimate surface melting (Semtner, 1984). Specifically for Snowball Earth initiation, using a three-layer sea-ice model instead of a zero-layer sea-ice model results in stronger ice–albedo feedback because the decreased surface melting results in larger ice cover and more snow on ice (Hörner et al., 2022). This results in easier Snowball Earth initiation with a tipping point that is located at 50 % higher $CO_2$ content. In this study, we will extend the results of Hörner et al. (2022) and demonstrate that the same mechanism also influences waterbelt states. Waterbelt states that are stable and accessible using the simple zero-layer model are destabilized and absent when the more sophisticated three-layer model is used.

This paper is structured as follows. In Sect. 2, the methods and the model setup are described. Section 3 presents the impacts of the different sea-ice schemes on the ice–albedo feedback and the waterbelt states. Section 4 discusses the implications for waterbelt states found previously in different climate models and provides a conclusion.

## 2 Methods

### 2.1 ICON-A

We deploy the icosahedral non-hydrostatic atmospheric (ICON-A) model (Giorgetta et al., 2018). There have been multiple studies on Snowball climate using the ICON model (e.g., Braun et al., 2022; Hörner et al., 2022; Ramme and Marotzke, 2022). Its predecessor ECHAM, which to a large extent uses the same physics package (Giorgetta et al., 2018), has also been used in Snowball Earth simulations (e.g., Marotzke and Botzet, 2007; Voigt and Abbot, 2012; Abbot et al., 2012), including studies of waterbelt states (Abbot et al., 2011; Voigt et al., 2011).

The model and model setup are the same as in Hörner et al. (2022) and Braun et al. (2022). We use ICON-A with an effective horizontal resolution of 160 km and 45 atmospheric vertical levels. ICON-A is coupled to a mixed-layer ocean of 50 m depth without any horizontal heat transport to simulate an aquaplanet without continents. A circular Kepler orbit and a solar constant reduced to $1285\,\mathrm{W\,m^{-2}}$, as well as an idealized 360 d year, are applied to represent Neoproterozoic boundary conditions (Gough, 1981). The albedo for cold snow and ice is 0.79 and 0.45, respectively. These values are linearly decreased to 0.66 for warm snow and 0.38 for warm ice, starting from 1 K below melting temperature.

The value of bare-ice albedo is at the lower end of the range suggested by observations (Dadic et al., 2013; Webster and Warren, 2022). Consequently, our choice of albedo values works in favor of a stable waterbelt state because of the large albedo difference between snow and bare ice. The main reason for our choice is to ensure comparability with the previous studies of Braun et al. (2022), Hörner et al. (2022) and Abbot et al. (2011), which employed precisely the same albedo values. Overall, the model setup follows Abbot et al. (2011), who first postulated the Jormungand state in idealized aquaplanet slab–ocean simulations with varying longwave forcing using the CAM and ECHAM models. Following Braun et al. (2022), we adapt the cloud scheme to allow ICON-A to simulate stable waterbelt states.

We compare simulations with two different sea-ice schemes: the Semtner zero-layer scheme (Semtner, 1976), hereafter Semtner-0L, and the Winton three-layer scheme (Winton, 2000), hereafter Winton-3L. Semtner-0L only considers surface temperature and does not predict internal ice temperatures. This means that the heat capacity of ice and brine pockets is neglected. Winton-3L, on the other hand, takes into account the heat capacity. The model follows the energy-conserving approach of Bitz and Lipscomb (1999) and predicts ice temperatures at two internal levels and at the surface. Energy stored in brine pockets is considered through a temperature-dependent enthalpy of fusion for ice. In the case of bare ice, Winton-3L allows a portion of incoming solar radiation to penetrate the ice. In both models, snow is converted to ice when the snow cover is submerged below

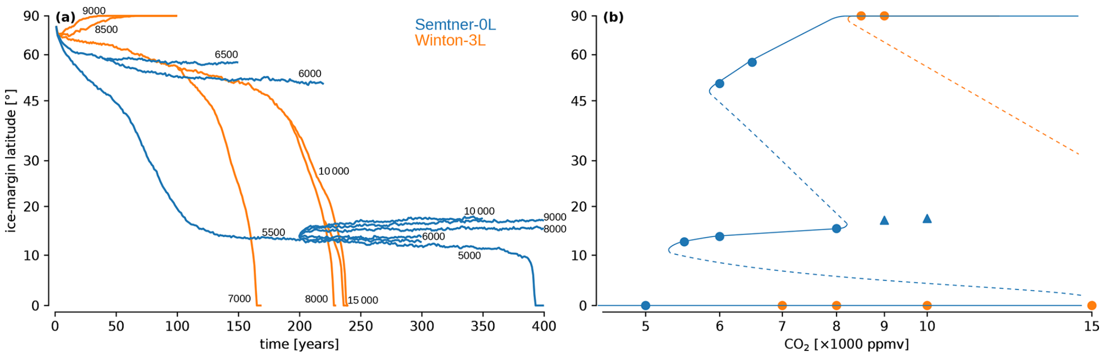


**Figure 1. (a)** Evolution of the yearly mean ice-margin latitude for simulations with Semtner-0L (blue) and Winton-3L (orange). Each line is labeled with its atmospheric $CO_2$ content in units of parts per million by volume (ppmv). **(b)** Estimated bifurcation diagrams. For equilibrated simulations, the ice-margin latitude is shown by solid circles. Simulations that continuously drift in snow cover are expected to melt and are depicted by upward-pointing triangles. Solid lines indicate the branches of stable equilibrium states, while dashed lines are for unstable equilibrium states. The exact positions of the tipping point and the branches of the unstable states are uncertain and should be considered best guesses.

the water level. For a more in-depth comparison of the ice models in the context of Snowball Earth initiation, we refer the reader to Hörner et al. (2022).

ICON-A tends to become more unstable in colder climates. We therefore decrease the time step from the initial 10 to 8 min and finally to 6 min. All stable simulations on the temperate branch of the bifurcation diagram use a time step of 10 min, and the waterbelt and Snowball Earth branches use a time step of 6 min (see Fig. 1). As in Ramme and Marotzke (2022), we increase the Rayleigh damping in the uppermost levels of the atmosphere for time steps smaller than 10 min (Klemp et al., 2008).

### 2.2 Simulation design

Two sets of simulations are performed: one using the Semtner-0L model (Semtner, 1976) and the other using the Winton-3L model (Winton, 2000). Each simulation is characterized by its constant atmospheric $CO_2$ content and its initial condition. Most simulations are started from ice-free initial conditions, with sea-surface temperatures (SSTs) derived from AMIP runs of the present-day climate. The initial SST profile is zonally symmetric and symmetric with respect to the Equator. The global average SST is 291 K, ranging from 273 K at the poles to 301 K at the Equator. Some simulations are branched off from other simulations after a certain ice-margin latitude has been reached. In these cases, a new simulation with a different constant atmospheric $CO_2$ content is started from a restart file of the parent simulation. This is done to find potentially hidden waterbelt states, to determine the width of the waterbelt hysteresis in the bifurcation diagram and to save computing time.

## 3 Results

### 3.1 Simulation overview

Stable waterbelt states are found with the zero-layer Semtner sea-ice model but not with the three-layer Winton model. Figure 1a shows the evolution of the ice margin for all simulations. All Winton-3L simulations either stay at an ice-free state or fall into a Snowball state in less than 250 years. Semtner-0L, in contrast, results in a waterbelt state when starting from ice-free initial conditions with a $CO_2$ content of 5500 ppmv. From there, more simulations are branched off with different $CO_2$ content to assess the width of the waterbelt hysteresis.

A best guess of the bifurcation diagram is constructed from these simulations in Fig. 1b. The waterbelt hysteresis in Semtner-0L extends over a range of $CO_2$ from 5500 to 8000 ppmv. The Semtner-0L bifurcation diagram is the same as in Braun et al. (2022) (their Fig. 1a), since we are using the same model and model setup. In Winton-3L no waterbelt state is found up to a $CO_2$ value of 15 000 ppmv. We cannot formally exclude the possibility of a hidden waterbelt state at even higher values of $CO_2$ forcing. However, even if such a state existed, it would be geologically irrelevant because it would be inaccessible from a temperate state. The atmospheric $CO_2$ to reach that state would be much higher than that of the tipping point of Snowball Earth initiation (between 8000 and 8500 ppmv). Additionally, the strong ice–albedo feedback in Winton-3L for a low-latitude ice margin (see Sect. 3.4) makes such a state unlikely.

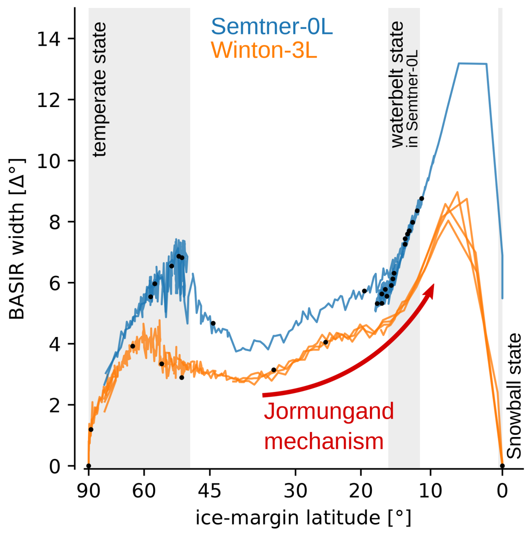


**Figure 2.** Width of the bare sea-ice region (BASIR) at the ice margin in degree latitude as a function of the transient latitude of the ice margin. For example, for an ice-margin latitude of 10° and a BASIR width of 10°, sea ice extends from the poles to 10° N/S, with bare ice between 10–20° N/S and snow-covered ice between 20 and 90° N/S. Gray boxes indicate the ranges of ice-margin latitudes where stable states are found in Semtner-0L (see Fig. 1b). Black points are plotted every 50 years after the start of each simulation to emphasize the position of stable states with a constant ice-margin latitude.

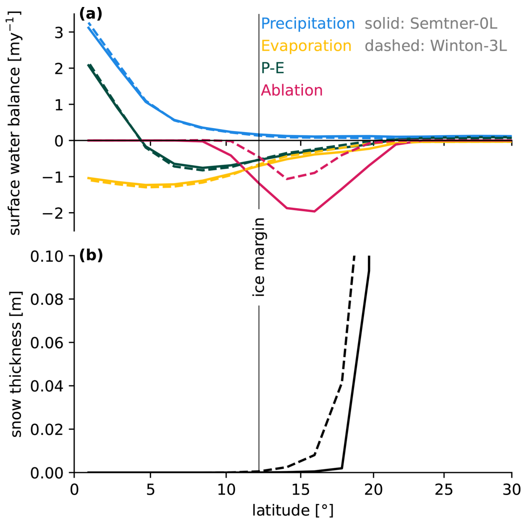


**Figure 3.** Zonal averages of precipitation, evaporation, precipitation–evaporation, surface ablation of sea ice and snow **(a)**, and snow thickness **(b)** in simulations using Semtner-0L (solid lines) and Winton-3L (dotted lines). The data are time-averaged over simulations from Semtner-0L and Winton-3L that have a sea-ice margin in the range between 11.25 and 13.125°, corresponding to one bin in Fig. 4. Vertical black lines indicate the center of the bin.

## 3.2 Jormungand mechanism

The difference between Semtner-0L and Winton-3L results from a strong difference in snow cover. Figure 2 shows the BASIR width for all simulations as a function of the ice-margin latitude. Independent of $CO_2$, Semtner-0L results in a wider BASIR than Winton-3L. In Semtner-0L, the BASIR widens with increasing global ice cover and reaches its maximum between 60 and 50°, near the tipping point marking the edge of the attractor of the temperate state. Following this, the BASIR width sharply decreases as sea ice reaches the midlatitudinal precipitation maximum. When sea ice passes 30°, the Jormungand mechanism becomes apparent. The BASIR width increases, as the negative P–E balance in the subtropics results in net snow melt. Ultimately, this results in stable waterbelt states at an ice-margin latitude between 12 and 15°, with a BASIR width of around 6.5°.

In Winton-3L, the BASIR width shows the same general features, but the BASIR is narrower for all sea-ice margins, as there is a larger snow cover on the ice. Although the Jormungand effect leads to a widening of the BASIR when sea ice reaches the subtropics in Winton-3L as well, the effect is much smaller than in Semtner-0L. This is caused by a large difference in surface melting near the ice margin, as can be seen in Fig. 3.

Figure 3a shows the zonal mean P–E balance and its components, as well as surface ablation when the sea-ice margin is at 12° in both models. Surface ablation includes melting and sublimation of both sea ice and snow, with melting being the dominant contribution. The P–E balance and its components, precipitation and evaporation, are almost identical in both models. Surface ablation, on the other hand, is up to twice as large in Semtner-0L as in Winton-3L in the region directly poleward of the sea-ice margin. This is a manifestation of the melt-ratchet effect. The neglected heat capacity in Semtner-0L results in a larger diurnal cycle of surface temperature and consequently larger surface melting. Ultimately, this results in thinner snow cover on ice (Fig. 3b), leading to a smaller BASIR width.

The difference in BASIR width modulates the ice–albedo feedback and hence determines waterbelt stability. To demonstrate this, we analyze the meridional structure of top-of-atmosphere (TOA) albedo as a function of the ice-margin latitude. More specifically, we aggregate data from two transient simulations with Semtner-0L and Winton-3L to cover the range from ice-free to Snowball states. For Semtner-0L, we aggregate the simulations with 5000 and 5500 ppmv $CO_2$ and for Winton-3L the simulations with 8000 and 8500 ppmv $CO_2$. Monthly and zonal mean output data of the simulations are binned according to the latitude of the ice margin, and data in each ice-margin latitude bin are averaged over all months in that bin. The result is the meridional distribution of TOA albedo as a function of ice-margin latitude shown in Fig. 4. The number of values per bin varies significantly, depending on how long the ice margin stays in that bin. This is illustrated by the histograms on top of panels (a) and (b) in Fig. 4.

The differences in BASIR width at the ice margin result in different TOA albedos in Semtner-0L compared to Winton-3L (Fig. 4c). The largest difference is located directly poleward of the ice margin. The albedo difference around the ice margin increases strongly as soon as the ice margin moves equatorward of 30°. This indicates the larger BASIR widening and thus stronger Jormungand mechanism in Semtner-0L. Importantly, strong differences in the TOA albedo occur for subtropical sea ice equatorward of 20°. This is because subtropical sea ice is bare in Semtner-0L as demanded by the Jormungand mechanism, but some snow is in fact able to persist on top of subtropical sea ice in Winton-3L. Consequently, waterbelt states are found in Semtner-0L with stable ice margins between 15 and 20°, and no waterbelt states are found in Winton-3L.

### 3.3 TOA energy budget

The widening of the BASIR when ice enters the subtropics lowers the TOA albedo and leads to a weakening of the ice–albedo feedback. In Semtner-0L, but not in Winton-3L, the weakening is strong enough to bring the TOA energy budget into equilibrium for waterbelt states. This behavior is illustrated in Fig. 5, which shows the global mean TOA energy budget in panel (a) and its shortwave and longwave components in panels (b) and (c).

Both ice models start out with a TOA energy budget close to equilibrium for ice margins corresponding to temperate climate states. When ice advances equatorward of 50°, the energy budget becomes more and more negative due to the runaway ice–albedo feedback. For Semtner-0L, the Jormungand mechanism becomes evident as the TOA energy budget reaches a local minimum for an ice margin of 30° and subsequently increases again until equilibrium is reached in a waterbelt state. Instead, for Winton-3L the TOA energy budget only shows a slight slowdown, and the Jormungand mechanism is not strong enough to restore the TOA energy budget into equilibrium.

The longwave component of the TOA energy budget depicted in Fig. 5c is mostly determined by temperature and the Planck feedback and is hence essentially the same in Semtner-0L and Winton-3L. Small differences are due to the different atmospheric $CO_2$ content in the simulations. For temperate states, Winton-3L emits marginally less longwave radiation compared to Semtner-0L since a larger $CO_2$ content is used in the Winton-3L simulations. In the region of the Jormungand state, Semtner-0L and Winton-3L have similar values of atmospheric $CO_2$ (see Fig. 1b) and hence a very similar longwave radiative flux.

The diverging evolution of the TOA energy budget between Semtner-0L and Winton-3L is driven by the shortwave component, i.e., the ice albedo. The global mean of the absorbed shortwave radiative flux as a function of ice-margin latitude is depicted in Fig. 5b. The slope of this line measures the strength of the ice–albedo feedback. The amount of absorbed shortwave radiation slowly diverges between the two ice models as sea ice expands from the midlatitudes into the subtropics, with Semtner-0L absorbing more shortwave radiation. This is a consequence of the increasing difference in surface albedo due to the difference in BASIR width shown in Fig. 4. In the waterbelt state, the difference is up to $2.5\,\mathrm{W\,m^{-2}}$ and increases further for ice margins closer to the Equator as the difference in the BASIR increases. The difference between Semtner-0L and Winton-3L is not driven by clouds, as the clear-sky energy budget exhibits the same behavior (not shown).

In summary, the larger surface melting in Semtner-0L due to the stronger melt-ratchet effect results in less snow on the ice and a wider BASIR. This weakens the ice–albedo feedback and strengthens the Jormungand mechanism by decreasing surface and TOA albedo near the sea-ice margin. Consequently, in Semtner-0L the TOA energy budget can be in equilibrium for low-latitude sea-ice margins, and waterbelt states are possible, whereas Winton-3L falls into a Snowball state.

### 3.4 Effect of ice model on snow cover

To further illustrate that Winton-3L favors more snow on ice, we perform an additional simulation with Winton-3L that is restarted from a stable waterbelt state simulated with Semtner-0L. The Winton-3L simulation is branched off from year 400 of the Semtner-0L simulation with 8000 ppmv $CO_2$ at year 400 (see Fig. 1). The initial internal ice temperatures that are required for the Winton-3L model are obtained from the ice surface temperatures from the restart file of the Semtner-0L simulation.

The 3L-Winton simulation falls into a Snowball state after 6 years. This is shown in terms of surface albedo in Fig. 6. The lower part of the figure depicts the first year in higher temporal resolution and the upper part the subsequent years until global glaciation is achieved. In Winton-3L surface albedo increases quickly within the first few months in the region of ice that is bare in Semtner-0L. This indicates that snow quickly accumulates on ice in Winton-3L and that the BASIR narrows. After 6 months the border between snow-free and snow-covered ice has clearly shifted towards the Equator in Winton-3L (dotted lines), and the increase in surface albedo has led to global cooling and more ice growth also in the summer (northern) hemisphere. In the following months and years until glaciation, this poses a feedback loop of increased snow cover in both summer and winter hemispheres, larger ice cover in the summer hemisphere, higher surface albedo, and lower temperatures.

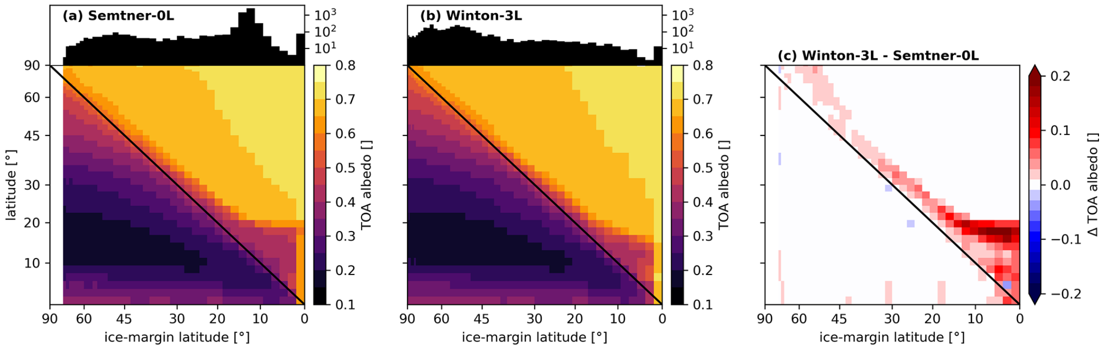


**Figure 4.** Meridional distribution ($y$ axis) of zonal mean top-of-atmosphere (TOA) albedo (colors) as a function of the transient ice-margin latitude ($x$ axis). The histograms on top of panels **(a)** and **(b)** show the number of data points per bin. **(a)** Semtner-0L. **(b)** Winton-3L. **(c)** Difference between Winton-3L and Semtner-0L.

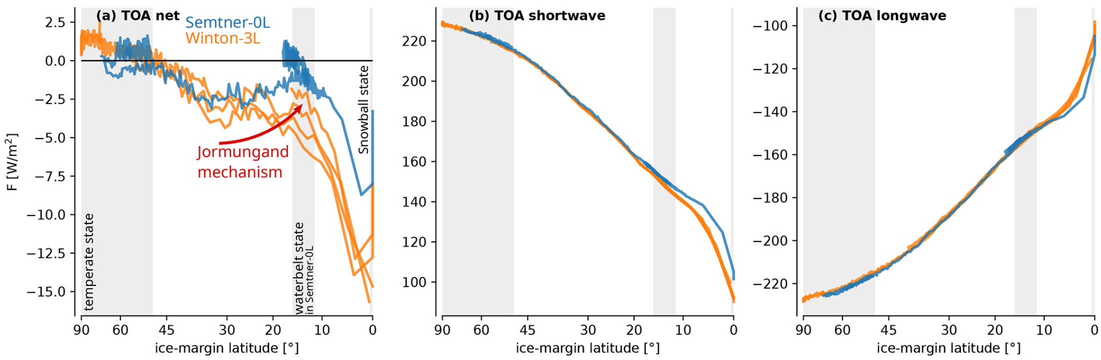


**Figure 5.** Components of the global mean top-of-atmosphere (TOA) energy budget as a function of the transient ice-margin latitude for all simulations with Semtner-0L (blue) and Winton-3L (orange). **(a)** Net energy budget. **(b)** Absorbed shortwave radiation. **(c)** Outgoing longwave radiation. Fluxes are defined as positive downward for all components. Gray boxes indicate the regions where stable states were found. Note that the TOA net energy balance in the Snowball state is not zero because the simulations were stopped as soon as global ice cover was reached. The TOA net energy balance at this point is not yet in equilibrium.

## 4 Conclusions

Previous work proposed that waterbelt states with low-latitude ice margins are possible thanks to the Jormungand mechanism. The Jormungand mechanism is based on a widening of the region of bare sea ice (abbreviated as BASIR) near the sea-ice margin when sea ice enters the subtropics, which decreases subtropical ice albedo and can stop the runaway ice–albedo feedback and stabilize the ice margin at around 15° (Abbot et al., 2011). In this study, we investigate the robustness of such waterbelt states with respect to the representation of the thermodynamics of sea ice. To this end, we conduct simulations with the ICON-A atmosphere model in an idealized aquaplanet setup using the simple zero-layer Semtner sea-ice model and the more sophisticated energy-conserving three-layer Winton model.

The main finding of our work is that stable waterbelt states are possible and accessible in the zero-layer Semtner model but not in the three-layer Winton model. We show that the lack of waterbelt states in the three-layer Winton model results from a narrower BASIR, which weakens the Jormungand mechanism and strengthens the ice–albedo feedback compared to the simulations with the zero-layer Semtner model. The BASIR is narrower in the three-layer Winton model because taking into account the vertical resolution and ice heat capacity decreases surface melting and allows more snow to accumulate on top of sea ice, in particular in the subtropics.

That ice vertical resolution is important to correctly simulate surface melting and hence Snowball Earth climates has been shown before by Abbot et al. (2010), Yang et al. (2012a, b) and Hörner et al. (2022), who demonstrated that insufficient vertical resolution overestimates surface melting

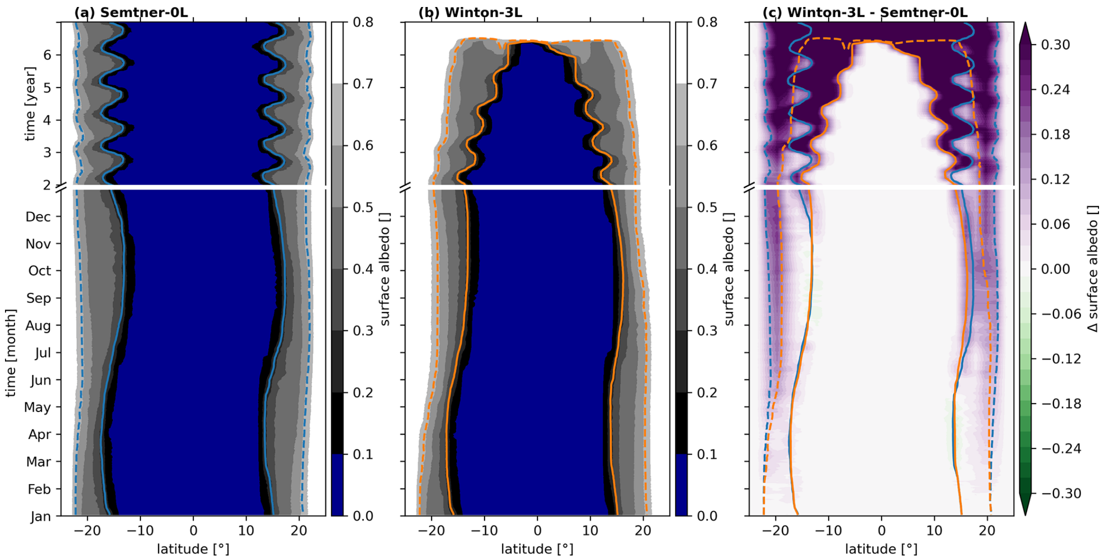


**Figure 6.** Zonal mean surface albedo for Semtner-0L **(a)** and Winton-3L **(b)** simulations as a function of time. The Winton-3L simulation is restarted from the stable Semtner-0L waterbelt simulation. Both simulations use 8000 ppmv $CO_2$. Solid lines indicate the ice margin, and dashed lines indicate the snow margin. **(c)** Difference in surface albedo between the Winton-3L and Semtner-0L simulations, with the ice and snow margin lines of both simulations overlaid. The initial year is shown with an enlarged time axis, and the following 5 years is depicted with a squeezed time axis.

due to a melt-ratchet effect. In Hörner et al. (2022) we specifically showed that insufficient vertical resolution enhances Snowball Earth initiation by allowing more ice and snow to persist into the summer months. Here, we study the effect of ice vertical resolution on the ice–albedo feedback over a wider range of climate states and find that the impact of vertical resolution becomes increasingly important as the ice margin moves toward the Equator. As a result, the vertical resolution of sea ice can determine the existence and stability of a waterbelt state by controlling the width of the BASIR.

Our results question the validity of waterbelt states. However, previous studies with a range of different sea ice models found waterbelt states. So, how important is the Jormungand mechanism, and how does it compare to other mechanisms? We briefly discuss this question in the following and note that, although the Jormungand mechanism may not be able to stabilize a waterbelt state on its own, it might add to other stabilizing mechanisms so that a waterbelt state might be possible.

- Multiple studies found waterbelt states in the atmospheric model CAM and the Earth system model family CCSM/CESM that CAM is part of (Abbot et al., 2011; Yang et al., 2012a, b; Wolf et al., 2017; Braun et al., 2022). These studies used a five-layer sea-ice scheme, which, based on our results, should lead to an even narrower BASIR and weaker Jormungand mechanism than in our three-layer Winton simulations. Braun et al. (2022) argued that optically thick mixed-phased clouds in the subtropics are in fact needed to stabilize the waterbelt state by muting the ice–albedo feedback in the CAM-idealized aquaplanet simulations of Abbot et al. (2011). On the other hand, it seems likely that the stable waterbelt states simulated in the coupled simulations of Yang et al. (2012a) and Yang et al. (2012b) are possible thanks to heat convergence near the ice margin by the ocean circulation.

- Continental configuration and surface topography might influence the stability of waterbelt states through snow cover on land. For example, Liu et al. (2018) showed with CESM that snow cover on land can decrease as the climate cools when surface topography blocks the moisture import from oceans onto the continental interiors. This could provide a stabilizing feedback that works in favor of waterbelt states.

- The Massachusetts Institute of Technology General Circulation Model (MITgcm) (e.g., Marshall et al., 2004) allows for waterbelt states that are solely stabilized by ocean heat transport (e.g., Rose, 2015; Brunetti et al., 2019; Ragon et al., 2022; Zhu and Rose, 2022). MITgcm uses the same thermodynamic three-layer Winton sea-ice model as our study. The waterbelt state in these studies does not show any BASIR. According to Rose

(2015), this is because the ice margin is located further poleward, between 21 and 30° latitude. This is outside the influence of the descending branch of the Hadley cell and thus outside the influence of the Jormungand mechanism. As they are stabilized by different mechanisms, they can be considered different climate states. This demonstrates that both mechanisms can stabilize a waterbelt state on their own.

- The atmosphere model ECHAM5 was used by Abbot et al. (2011) to first demonstrate the Jormungand mechanism in an idealized aquaplanet simulation, and its coupled atmosphere–ocean version ECHAM5-MPIOM was used by Voigt and Abbot (2012) to test the robustness with respect to sea-ice dynamics. Both ECHAM5 and ECHAM5-MPIOM used a zero-layer Semtner model. ECHAM5 did not track snow on the ice, and, because of this, the BASIR had to be hard-coded into the model. The ECHAM5-MPIOM simulations showed that, while the Jormungand mechanism appeared to be active, it was not strong enough to allow for waterbelt states that are separated from temperate states by a bifurcation, and the strong sea ice dynamics in the model inhibited stable subtropical ice margins.

- The ICON model is the successor of ECHAM5 and ECHM5-MPIOM and also uses the zero-layer Semtner sea-ice scheme in its standard version. Braun et al. (2022) demonstrated that the ICON model has difficulties in simulating stable waterbelt states because subtropical clouds are not reflective enough in the model. If cloud optical thickness and cloud reflectivity are increased, the Jormungand mechanism leads to waterbelt states in ICON.

Our results show that, in order for the Jormungand mechanism to lead to stable waterbelt states, the region of bare sea ice needs to be sufficiently wide. Simulations with simplified sea-ice models overestimate the width of the bare sea-ice region and therefore likely overestimate the stability of waterbelt states. Consequently, waterbelt states that rely exclusively on the Jormungand mechanism might only be possible for rather peculiar combinations of a coarse vertical resolution of ice and optically thick subtropical clouds. This suggests that the Jormungand mechanism itself might be secondary and robust waterbelt states are only possible if other stabilizing mechanisms, particularly those from ocean heat transport, are also active.

**Code and data availability.** The data required to create the figures and the code for simulations runs and the postprocessing and creation of figures are available at https://doi.org/10.25365/phaidra.429 (Hörner and Voigt, 2024).

**Author contributions.** JH performed the simulations and analysis and wrote the initial draft. JH and AV wrote the final draft. AV supervised the project.

**Competing interests.** The contact author has declared that neither of the authors has any competing interests.

**Disclaimer.** Publisher's note: Copernicus Publications remains neutral with regard to jurisdictional claims made in the text, published maps, institutional affiliations, or any other geographical representation in this paper. While Copernicus Publications makes every effort to include appropriate place names, the final responsibility lies with the authors.

**Acknowledgements.** The computational results presented have been achieved using the Vienna Scientific Cluster (VSC). AI tools (DeepL and ChatGPT) were used to improve the grammar, writing style and wording for parts of an earlier version of the paper. We thank Tobias Necker for his input on how to clarify the paper. We thank the reviewers Stephen Warren and Yonggang Liu for their constructive feedback.

**Financial support.** Open-access funding was provided by University of Vienna.

**Review statement.** This paper was edited by Roberta D'Agostino and reviewed by Stephen Warren and Yonggang Liu.

## References

Abbot, D. S., Eisenman, I., and Pierrehumbert, R. T.: The Importance of Ice Vertical Resolution for Snowball Climate and Deglaciation, J. Climate, 23, 6100–6109, https://doi.org/10.1175/2010JCLI3693.1, 2010.

Abbot, D. S., Voigt, A., and Koll, D.: The Jormungand global climate state and implications for Neoproterozoic glaciations, J. Geophys. Res., 116, D18103, https://doi.org/10.1029/2011JD015927, 2011.

Abbot, D. S., Voigt, A., Branson, M., Pierrehumbert, R. T., Pollard, D., Hir, G. L., and Koll, D. D. B.: Clouds and Snowball Earth deglaciation, Geophys. Res. Lett., 39, L20711, https://doi.org/10.1029/2012GL052861, 2012.

Bitz, C. M. and Lipscomb, W. H.: An energy-conserving thermodynamic model of sea ice, J. Geophys. Res.-Oceans, 104, 15669–15677, https://doi.org/10.1029/1999JC900100, 1999.

Braun, C., Hörner, J., Voigt, A., and Pinto, J. G.: Ice-free tropical waterbelt for Snowball Earth events questioned by uncertain clouds, Nat. Geosci., 15, 489–493, https://doi.org/10.1038/s41561-022-00950-1, 2022.

Brunetti, M., Kasparian, J., and Vérard, C.: Co-existing climate attractors in a coupled aquaplanet, Clim. Dynam., 53, 6293–6308, https://doi.org/10.1007/s00382-019-04926-7, 2019.

Dadic, R., Mullen, P. C., Schneebeli, M., Brandt, R. E., and Warren, S. G.: Effects of bubbles, cracks, and volcanic tephra on the spectral albedo of bare ice near the Transantarctic Mountains: Implications for sea glaciers on Snowball Earth, J. Geophys. Res.-Earth Surf., 118, 1658–1676, https://doi.org/10.1002/jgrf.20098, 2013.

Giorgetta, M. A., Brokopf, R., Crueger, T., Esch, M., Fiedler, S., Helmert, J., Hohenegger, C., Kornblueh, L., Köhler, M., Manzini, E., Mauritsen, T., Nam, C., Raddatz, T., Rast, S., Reinert, D., Sakradzija, M., Schmidt, H., Schneck, R., Schnur, R., Silvers, L., Wan, H., Zängl, G., and Stevens, B.: ICON-A, the Atmosphere Component of the ICON Earth System Model: I. Model Description, J. Adv. Model. Earth Sy., 10, 1613–1637, https://doi.org/10.1029/2017MS001242, 2018.

Gough, D. O.: Solar Interior Structure and Luminosity Variations, Sol. Phys., 74, 21–34, https://doi.org/10.1007/978-94-010-9633-1_4, 1981.

Hoffman, P. and Schrag, D.: The snowball Earth hypothesis: testing the limits of global change, Terra Nova, 14, 129–155, https://doi.org/10.1046/J.1365-3121.2002.00408.X, 2002.

Hoffman, P. F., Abbot, D. S., Ashkenazy, Y., Benn, D. I., Brocks, J. J., Cohen, P. A., Cox, G. M., Creveling, J. R., Donnadieu, Y., Erwin, D. H., Fairchild, I. J., Ferreira, D., Goodman, J. C., Halverson, G. P., Jansen, M. F., Hir, G. L., Love, G. D., Macdonald, F. A., Maloof, A. C., Partin, C. A., Ramstein, G., Rose, B. E. J., Rose, C. V., Sadler, P. M., Tziperman, E., Voigt, A., and Warren, S. G.: Snowball Earth climate dynamics and Cryogenian geology-geobiology, Sci. Adv., 3, e1600983, https://doi.org/10.1126/sciadv.1600983, 2017.

Hörner, J. and Voigt, A.: Sea-ice thermodynamics can determine waterbelt scenarios for Snowball Earth, University of Vienna [code and data set], https://doi.org/10.25365/phaidra.429, 2024.

Hörner, J., Voigt, A., and Braun, C.: Snowball Earth initiation and the thermodynamics of sea ice, J. Adv. Model. Earth Sy., e2021MS002734, e2021MS002734, https://doi.org/10.1029/2021MS002734, 2022.

Hyde, W. T., Crowley, T. J., Baum, S. K., and Peltier, W. R.: Neoproterozoic "snowball Earth" simulations with a coupled climate/ice-sheet model, Nature, 405, 425–429, https://doi.org/10.1038/35013005, 2000.

Kirschvink, J. L.: Late Proterozoic Low-Latitude Global Glaciation: the Snowball Earth, in: The Proterozoic Biosphere: A Multidisciplinary Study, edited by: Schopf, J. W. and Klein, C., pp. 51–52, Cambridge University Press, New York, ISBN 978-0-521-36615-1, 1992.

Klemp, J. B., Dudhia, J., and Hassiotis, A. D.: An Upper Gravity-Wave Absorbing Layer for NWP Applications, Mon. Weather Rev., 136, 3987–4004, https://doi.org/10.1175/2008MWR2596.1, 2008.

Liu, Y., Peltier, W. R., Yang, J., and Hu, Y.: Influence of Surface Topography on the Critical Carbon Dioxide Level Required for the Formation of a Modern Snowball Earth, J. Climate, 31, 8463–8479, https://doi.org/10.1175/JCLI-D-17-0821.1, 2018.

Marotzke, J. and Botzet, M.: Present-day and ice-covered equilibrium states in a comprehensive climate model, Geophys. Res. Lett., 34, L16704, https://doi.org/10.1029/2006GL028880, 2007.

Marshall, J., Adcroft, A., Campin, J.-M., Hill, C., and White, A.: Atmosphere–Ocean Modeling Exploiting Fluid Isomorphisms, Mon. Weather Rev., 132, 2882–2894, https://doi.org/10.1175/MWR2835.1, 2004.

Pierrehumbert, R. T., Abbot, D. S., Voigt, A., and Koll, D.: Climate of the Neoproterozoic, Annu. Rev. Earth Pl. Sc., 39, 417–460, https://doi.org/10.1146/annurev-earth-040809-152447, 2011.

Ragon, C., Lembo, V., Lucarini, V., Vérard, C., Kasparian, J., and Brunetti, M.: Robustness of Competing Climatic States, J. Climate, 35, 2769–2784, https://doi.org/10.1175/JCLI-D-21-0148.1, 2022.

Ramme, L. and Marotzke, J.: Climate and ocean circulation in the aftermath of a Marinoan snowball Earth, Clim. Past, 18, 759–774, https://doi.org/10.5194/cp-18-759-2022, 2022.

Rose, B. E. J.: Stable "Waterbelt" climates controlled by tropical ocean heat transport: A nonlinear coupled climate mechanism of relevance to Snowball Earth, J. Geophys. Res.-Atmos., 120, 1404–1423, https://doi.org/10.1002/2014JD022659, 2015.

Semtner, A. J.: A Model for the Thermodynamic Growth of Sea Ice in Numerical Investigations of Climate, J. Phys. Oceanogr., 6, 379–389, https://doi.org/10.1175/1520-0485(1976)006<0379:AMFTTG>2.0.CO;2, 1976.

Semtner, A. J.: On modelling the seasonal thermodynamic cycle of sea ice in studies of climatic change, Clim. Change, 6, 27–37, https://doi.org/10.1007/BF00141666, 1984.

Voigt, A. and Abbot, D. S.: Sea-ice dynamics strongly promote Snowball Earth initiation and destabilize tropical sea-ice margins, Clim. Past, 8, 2079–2092, https://doi.org/10.5194/cp-8-2079-2012, 2012.

Voigt, A., Abbot, D. S., Pierrehumbert, R. T., and Marotzke, J.: Initiation of a Marinoan Snowball Earth in a state-of-the-art atmosphere-ocean general circulation model, Clim. Past, 7, 249–263, https://doi.org/10.5194/cp-7-249-2011, 2011.

Warren, S. G., Brandt, R. E., Grenfell, T. C., and McKay, C. P.: Snowball Earth: Ice thickness on the tropical ocean, J. Geophys. Res.-Oceans, 107, 3167, https://doi.org/10.1029/2001JC001123, 2002.

Webster, M. A. and Warren, S. G.: Regional Geoengineering Using Tiny Glass Bubbles Would Accelerate the Loss of Arctic Sea Ice, Earth's Future, 10, e2022EF002815, https://doi.org/10.1029/2022EF002815, 2022.

Winton, M.: A Reformulated Three-Layer Sea Ice Model, J. Atmos. Ocean. Tech., 17, 525–531, https://doi.org/10.1175/1520-0426(2000)017<0525:ARTLSI>2.0.CO;2, 2000.

Wolf, E. T., Shields, A. L., Kopparapu, R. K., Haqq-Misra, J., and Toon, O. B.: Constraints on Climate and Habitability for Earth-like Exoplanets Determined from a General Circulation Model, ApJ, 837, 107, https://doi.org/10.3847/1538-4357/aa5ffc, 2017.

Yang, J., Peltier, W. R., and Hu, Y.: The Initiation of Modern "Soft Snowball" and "Hard Snowball" Climates in CCSM3. Part I: The Influences of Solar Luminosity, $CO_2$ Concentration, and the Sea Ice/Snow Albedo Parameterization, J. Climate, 25, 2711–2736, https://doi.org/10.1175/JCLI-D-11-00189.1, 2012a.

Yang, J., Peltier, W. R., and Hu, Y.: The Initiation of Modern "Soft Snowball" and "Hard Snowball" Climates in CCSM3. Part II: Climate Dynamic Feedbacks, J. Climate, 25, 2737–2754, https://doi.org/10.1175/JCLI-D-11-00190.1, 2012b.

Zhu, F. and Rose, B. E. J.: Multiple Equilibria in a Coupled Climate-Carbon Model, J. Climate, 36, 547–564, https://doi.org/10.1175/JCLI-D-21-0984.1, 2022.

# 6 Making sense of bifurcation diagrams

The second publication addresses research question 2: What is the contribution of the Jormungand mechanism, cloud masking, and cloud radiative feedback for the stability of waterbelt states?

A new framework is introduced that allows for the quantification of the three factors that influence waterbelt stability. First, these factors are demonstrated in an adapted EBM. Then, a method is presented to quantify these factors from GCM output by using the Approximate Partial Radiative Perturbation (APRP) method. Finally, the method is applied to output of three different versions of the ICON model

This study was designed and written by the author and Aiko Voigt. Model setup, simulation runs, data analysis, and visualization were performed by the author. The author's contribution is thus estimated to be about 75%.

The paper was submitted to the Journal of Geophysical Research - Atmospheres on 7.2.2025 and is publicly available as a preprint.

**Hörner, J., & Voigt, A. (2025). Making sense of bifurcation diagrams: A new framework to understand the role of clouds and bare sea ice for waterbelt states. *ESS Open Archive, under review for JGR-A*. DOI:10.22541/essoar.173924231.15255244/v1**

# Making sense of bifurcation diagrams: a new framework to understand the role of clouds and bare sea ice for waterbelt states

**Johannes Hörner[1], Aiko Voigt[1]**

[1]Department of Meteorology and Geophysics, University of Vienna, Vienna, Austria

**Key Points:**

- A new framework is established to quantify three atmospheric factors that influence waterbelt states.
- The width of the Hadley circulation determines the boundary between snow-covered and bare sea ice, modulating the ice-albedo feedback.
- Clouds can weaken the ice-albedo feedback through cloud masking, but can also induce a destabilizing shortwave cloud feedback.

Corresponding author: Johannes Hörner, `johannes.hoerner@univie.ac.at`

## Abstract

Earth has experienced several pan-glaciations in its history, often interpreted as hard Snowball Earth periods with complete global ice cover. Alternatively, waterbelt states with a narrow equatorial strip of ice-free ocean provide a compelling explanation for the survival of life during these extreme glaciations. In this study, we establish a framework to quantify three atmospheric factors that influence waterbelt states: the spatial extent of bare dark sea ice, cloud masking of the ice-albedo feedback, and cloud shortwave feedback. We first explore these factors in the Budyko-Sellers energy balance model, and then investigate them in simulations with three versions of the three-dimensional climate model ICON. This allows us to relate differences in the waterbelt states between climate model versions to differences in the three factors.

A broader Hadley circulation shifts the boundary between snow-covered and bare sea ice poleward, leading to waterbelt states with an ice line at higher latitudes. Clouds work in favor of stable waterbelt states by weakening the ice-albedo feedback through cloud masking. A positive shortwave cloud feedback due to increasing cloud condensate over the open ocean destabilizes waterbelt states. While our study does not answer which of the model versions is most realistic, it provides a quantitative framework for understanding the atmospheric mechanisms that govern the existence and hysteresis of waterbelt states.



## Plain Language Summary

Scientists have long debated whether Earth was completely covered in ice during past extreme ice ages (Snowball Earth) or if a narrow strip of ocean remained ice-free near the equator (a "waterbelt state"). Waterbelt states are an attractiv hypothesis, as the open water provides an easy explanation for the survival of life. This study examines three key atmospheric factors that influence these waterbelt states: how much dark sea ice is exposed, how clouds affect ice reflectivity, and how changes in clouds itself influence reflectivity.

Using climate models in different versions, this study shows that a wider tropical circulation increases the area of exposed dark sea ice. Clouds help stabilize waterbelt states by reducing the impact of ice reflectivity but can also make them less stable by increasing reflectivity over open water. While the study does not determine which model is most

accurate, it provides a framework for understanding the atmospheric processes that control these climate states.

## 1 Introduction

The climate of Earth can exist in multiple stable states that result from the interplay of feedback mechanisms. Central to these mechanisms is the positive ice-albedo feedback, which allows Earth to sustain, for the same insolation and greenhouse gas levels, a temperate climate with ice cover limited to the polar regions, similar to today, and a much colder Snowball Earth climate with global or near-global ice cover. As temperatures drop and ice expands towards lower latitudes, the ice-albedo feedback can become so strong that a runaway glaciation is triggered. Geological evidence indicates that such dramatic climatic transitions have occurred several times in Earth's history, most notably in the Neoproterozoic (1,000 - 540 million years before present) (Hoffman et al., 2017; Pierrehumbert et al., 2011).

Fundamental characteristics of these extreme glaciations remain a subject of debate, however. One key question is whether Earth transitioned to a so-called "hard" Snowball Earth with global ice cover, or whether it was able to avoid complete glaciation by retaining a narrow equatorial band of open ocean, a scenario known as waterbelt states (Hoffman et al., 2017; Abbot et al., 2011; Rose, 2015; Wolf et al., 2017). Waterbelt states are separated from present-day-like and hard Snowball states by additional bifurcations and can explain the geological evidence without invoking global ice cover. Because they provide an easy explanation for the survival of life, they are considered an attractive alternative to the hard snowball states.

Two main mechanisms have been proposed that lead to waterbelt states. The first involves ocean dynamics: energy transport by the wind-driven ocean circulation from the equator into the subtropics can maintain an ice-free margin at low latitudes, preventing complete glaciation (Rose, 2015). The second mechanism is purely based on atmospheric processes and has been dubbed "Jormungand mechanism" by Abbot et al. (2011): as sea ice enters the dry regions of the descending branch of the Hadley circulation, the lack of precipitation leads to snow-free sea ice that is much darker than the snow-covered sea ice at higher latitudes. This weakens the ice-albedo feedback and can allow the ice edge to stabilize in the subtropics. In this study, we investigate waterbelt states that result from the Jormungand mechanism.

The Jormungand mechanism is based on the basic physics of the Hadley circulation, its effect on low-latitude atmospheric moisture transport and precipitation, and the robust creation of a bare sea ice region when sea ice enters the subtropics (termed BASIR by Hörner and Voigt (2024)). Yet, the strength of the Jormungand mechanism and its ability to generate waterbelt states were found to vary considerably between climate models. Abbot et al. (2011) found robust waterbelt states over a wide range of atmospheric carbon dioxide in both the CAM3 and ECHAM5 models. Waba (2024), using the ExoCAM model based on CAM4, also found robust waterbelt states. In contrast, waterbelt states were found to be less robust in the ICON climate model and to depend on the treatment of cloud processes (Braun et al., 2022) and sea-ice thermodynamics (Hörner & Voigt, 2024). All these studies used an aquaplanet slab ocean setup without ocean heat transport and ocean dynamics, and focused on the Jormungand mechanism.

In this study we aim to develop a framework that brings order into this model diversity. That is, can we relate differences between models to differences in their treatment of clouds and the BASIR. And can we do this in a quantitative manner? We specifically focus on three factors that are intimately tied to the Jormungand mechanism and are illustrated in Figure 1:

1. BASIR: The bare sea-ice region near the ice edge is key to the Jormungand mechanism, because it underlies the weakening of the ice-albedo feedback. Without a BASIR, the Jormungand mechanism could not operate. A wider BASIR works in favor of waterbelt states.
2. Cloud masking: Ice growth has a stronger effect on the top-of-atmosphere albedo under clear-sky than cloudy-sky conditions. By masking surface changes, the presence of clouds reduces the strength of the ice-albedo feedback (Soden et al., 2004). If clouds at or just equatorward of the subtropical ice margin are more abundant and reflect more shortwave radiation, cloud masking is stronger, working in favor of waterbelt states.
3. Cloud feedbacks: Changes in clouds lead to radiative feedbacks that can amplify or dampen climate change, depending on the cloud change. If clouds change to reflect more shortwave radiation, this leads to a positive shortwave cloud feedback.

This feedback might be strong enough to overwhelm the reduction of the ice-albedo feedback by the Jormungand mechanism. In this case, waterbelt states would be destabilized and may even be impossible.

That the three factors are important for waterbelt states is known from previous work. Hörner and Voigt (2024) demonstrated the importance of the BASIR, while Braun et al. (2022) highlighted the role of cloud masking. Moreover, model simulations of the transition from a temperate Earth to a Snowball Earth discussed the effect of cloud-radiative feedbacks (Yang et al., 2012). The contribution of our work is therefore to develop the framework as a toolkit to explain why waterbelt states are present in some climate models and absent in others. The framework requires only standard model output and can be easily applied to future simulations as well as archived past simulations.

We develop the framework first by considering extended versions of the Budyko-Sellers energy balance model in Section 2. This allows us to understand how the three factors affect the existence of waterbelt states and the overall structure of the bifurcation diagram of Earth's climate. We then describe how the factors can be quantified from the output of global climate model simulations in Section 3. In Section 4 we illustrate this quantification for simulations with three different versions of the ICON model. The paper concludes in Section 5. We emphasize that the focus of the paper is to present the framework. We have concrete plans to apply the framework to a larger set of model simulations, including those with different climate models, in future work.

## 2 The three factors in an energy balance model

In this section we study the three factors in an Budyko-Sellers energy balance model (EBM) (Budyko, 1969; Sellers, 1969). The EBM is adapted to include the Jormungand mechanism following Abbot et al. (2011) and further adapted to include a shortwave cloud feedback. The cloud masking factor does not require any particular adaptation. For reference, we first briefly recall the original version of the model. For detailed descriptions of the original Budyko-Sellers EBM, we refer the reader to North (1975) and Held and Suarez (1974).

The model uses the the energy balance at the top of the atmosphere (TOA) to predict surface temperature $T$ at each latitude $0° \leq \varphi \leq 90°$. Instead of latitude, it is convenient to use the sine of latitude $x = \sin\varphi$, which increases from 0 at the equator

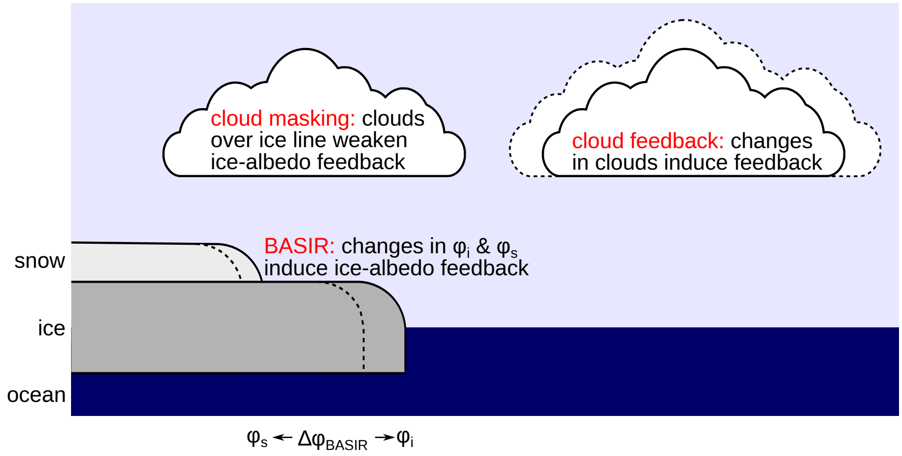


**Figure 1.** Schematic of the three factors that govern waterbelt states generated by the Jormungand mechanism. The bare sea-ice region (BASIR) is the defining feature of the Jormungand mechanism. Clouds around the ice and snow lines mask changes in surface albedo from expanding ice. Changes in clouds, depicted by the dots, can create a cloud feedback.

to 1 at the pole. The energy balance is

$$\frac{Q}{4}s(x)\,(1-\alpha)) = A + BT(x) + C(T(x) - \overline{T}), \tag{1}$$

where $Q$ is the solar constant, $s(x) = 1 - 0.241 \cdot (3x^2 - 1)$ describes the meridional profile of incoming solar radiation, and $\alpha$ is the TOA albedo. Outgoing longwave radiation is linearized as $A + B(T)$. The last term on the r.h.s. describes the effect of meridional heat transport, assumed to be proportional to the difference between the local surface temperature and the global-mean temperature $\overline{T} = \int_0^1 T(x)dx$.

The TOA albedo is the result of shortwave reflection by the surface and the atmosphere, most notably clouds. The difference in surface reflection between bright ice and dark ocean is accounted for by making $\alpha$ a function of surface temperature $T$. For temperatures above the threshold for ice formation, $T > T_i$, a low value of $\alpha = \alpha_o$ represents the open ocean with clouds above. Below $T_i$, the surface is covered by ice and a high value of $\alpha = \alpha_i$ is used. Because the additional reflection from clouds over bright ice surfaces is small, $\alpha_i$ is set equal to the surface albedo. At the ice line $x_i$, for which $T(x_i) = T_i$, the albedo is set to the mean of the ocean and ice albedos. In summary,

$$\alpha = \begin{cases} \alpha_o & T > T_i \\ \tilde{\alpha} = \frac{\alpha_o + \alpha_i}{2} & T = T_i \\ \alpha_i & T < T_i \end{cases} \tag{2}$$

The global energy balance is obtained by integrating Equation 1 over latitude,

$$\frac{Q}{4}(1 - \alpha_p(x_i)) = A + B\overline{T}. \tag{3}$$

$\alpha_p = \int_0^1 \alpha(x)s(x)dx$ is the global-mean TOA albedo, given by the ratio of the global-mean reflected and incoming shortwave radiative fluxes at TOA. Equation 3 expresses the competing effects of the positive shortwave feedback on the l.h.s., caused by the albedo change from dark ocean to bright ice, and the stabilizing Planck feedback on the r.h.s, acting on longwave radiation. The global-mean TOA albedo depends on the latitude of the ice line and is calculated from the integral

$$\alpha_p(x_i) = \int_0^{x_i} \alpha_o s(x)dx + \int_{x_i}^1 \alpha_i s(x)dx. \tag{4}$$

As described by Abbot et al. (2011), the model is solved by finding the value of $A$ that satisfies Equation 1 at the ice line $x_i$. By writing $A$ as the difference from a reference value, $A = A_0 - \Delta A$, one obtains the solutions as $\Delta A(x_i)$. $\Delta A(x_i)$ can be thought of as the TOA longwave radiative forcing from changes in atmospheric $CO_2$ that allows for a climate state with ice limited to latitudes poleward of $x_i$.

The result is the bifurcation diagram shown by the black line in Figure 3 for typical parameter values: $T_i = 0°\mathrm{C}$, $\alpha_i = 0.8$, $\alpha_o = 0.35$, $B = 1.5\,\mathrm{W\,m^{-2}\,K^{-1}}$, $C = 1.5B$, and $A_0 = 210\,\mathrm{W\,m^{-2}}$. A reduced insolation of $Q = 1285\,\mathrm{W\,m^{-2}}$ (96% of present-day) is used to account for the weaker Neoproterozoic sun.

For a range of radiative forcings, $55\,\mathrm{W\,m^{-2}} \leq \Delta A \leq 105\,\mathrm{W\,m^{-2}}$, the model has three solutions. Two of them are stable: present-day-like states with no ice or ice confined to high latitudes on the one hand, and Snowball Earth states with ice extending to the equator on the other hand. The two stable states are separated by a third solution that is unstable because its total feedback is positive, as shown further below, and that is unphysical because its ice line moves equatorward when the radiative forcing is increased.

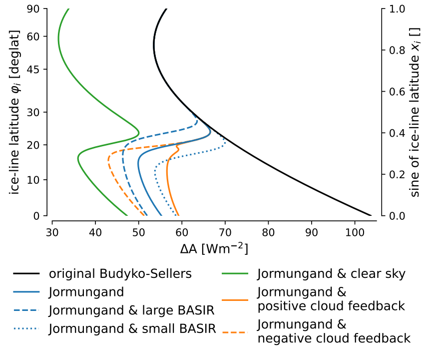


**Figure 2.** Bifurcation diagrams for different versions of the EBM. Black: original Budyko-Sellers model for parameter values as given in the main text. Blue: Jormungand version for three values of the snow-line latitude that lead to different widths of the BASIR ($x_s = 0.35$ in solid, 0.4 in dashed, 0.3 in dotted). Parameter values as for the original model and $\alpha_i^s = 0.8$, $\alpha_i^i = 0.5$, $\Delta x_s = 0.04$. Green: Jormungand version with lower TOA ocean albedo, representing clear-sky conditions. Parameter values are the same as for the Jormungand version with $x_s = 0.35$, and $\alpha_o = 0.25$. Orange: Jormungand version with a positive (solid) and a negative (dashed) cloud feedback. Parameter values are the same as for the Jormungand version with $x_s = 0.35$, and $\alpha_o^{ref} = 0.35$, $\Delta x_c = 0.015$, $x_c = 0.33$, $\Delta\alpha_o^c = \pm 0.05$ (positive value for the positive cloud feedback, negative value for the negative cloud feedback).

### 2.1 Jormungand mechanism and BASIR width

Abbot et al. (2011) modified the EBM to include the Jormungand mechanism. To do this, they allowed the TOA albedo of ice-covered regions, $\alpha_i$, to vary with latitude. At high latitudes, the ice is covered by snow and has the same high albedo as in the original model. At low latitudes, however, the ice is in the descending branch of the Hadley cell, where large-scale subsidence leads to net evaporation ($P - E < 0$, with precipitation $P$ and evaporation $E$). Net evaporation means that low-latitude ice is snow-free and darker than snow-covered ice at higher latitudes, and a lower TOA albedo must be assumed for ice equatorward of the snow line that separates snow-covered from bare ice. In the following, we use $x_s$ as the sine of the snow-line latitude.

Mathematically, the TOA albedo of ice-covered regions is written as

$$\alpha_i(x) = \alpha_i^i + \left(\frac{\alpha_i^s - \alpha_i^i}{2}\right)\left(1 + \tanh\left(\frac{x - x_s}{\Delta x_s}\right)\right), \tag{5}$$

where $\alpha_i^i$ stands for bare dark ice in the subtropics and $\alpha_i^s$ for snow-covered light ice further poleward of the snow line. Hence, $\alpha_i^i < \alpha_i^s$. A typical choice is $\alpha_i^i = 0.5$ and $\alpha_i^s = 0.8$. The transition from bare to snow-covered ice occurs over a region with width $\Delta x_s$. Note that while the snow line $x_s$ is a model parameter in the EBM, it depends on the width of the Hadley cell (Section 4; Abbot et al. (2011)) and the thermodynamics of sea ice (Hörner & Voigt, 2024) in global climate models.

When Equation 5 is substituted into Equation 2, one can calculate the bifurcation diagram in the same way as for the original model. For ice poleward of the snow line, the Jormungand adaptation has no effect and the solutions are the same as in the original model. When ice reaches the subtropics, the lower TOA albedo of bare ice regions weakens the ice-albedo feedback so that the runaway glaciation is stopped and stable states with ice lines around 20 degrees latitude become possible. The Jormungand adaptation hence leads to a third stable state: the waterbelt state, shown as the blue line in Figure 2.

The snow-line latitude defines the latitude where ice begins to be bare and determines the width of the BASIR. We define the BASIR as the difference between the snow-line latitude and the ice-line latitude, $\varphi_s - \varphi_i$, with $x_s = \sin\varphi_s$. In the EBM, $\varphi_s$ is fixed. The BASIR width is zero as long as ice is poleward of the snow-line latitude and increases linearly with the ice-line latitude thereafter (Figure 3).

The snow-line latitude, and with it the BASIR width, determines the latitudinal position of the waterbelt hysteresis and the accessibility of waterbelt states. This is shown by the blue lines in Figure 2. When the Jormungand mechanism sets in earlier, the snow line is shifted poleward and the BASIR is wider (for the same ice line), for example because of a wider Hadley circulation, waterbelt states occur at higher latitudes and for lower radiative forcings. As a result, waterbelt states co-exist with the present-day-like states over a smaller range of radiative forcings and are easier to access (dashed blue line). In contrast, when the Jormungand mechanism sets in later, the snow line is closer to the equator and the BASIR is narrower, waterbelt states are shifted to higher radiative forcings (dotted blue line). In the example shown in Figure 2, the shift is so strong that waterbelt states become "hidden": they can no longer be accessed from present-day-like states by a time-constant reduction in radiative forcing.

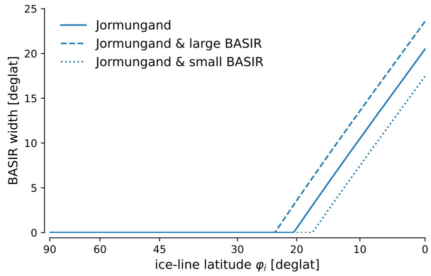


**Figure 3.** BASIR width in the Jormungand version of the EBM as a function of the ice-line latitude for the three cases shown in Figure 2.

### 2.2 Cloud masking

Cloud masking refers to the reduction in the strength of the ice-albedo feedback due to the presence of clouds. Cloud masking can stabilize waterbelt states, broaden the range of radiative forcings over which they exist, and increase their accessibility Braun et al. (2022).

It is straightforward to investigate the effect of cloud masking in the EBM. To do so, we compare the model to a clear-sky version that uses a lower TOA ocean albedo $\alpha_o^{cs} < \alpha_o$. The TOA albedo is changed only over the ocean, since the effect of cloud masking is much smaller for ice- and snow-covered regions due to their higher surface albedo. Although a simplification, this choice is supported by the GCM simulations presented later.

The clear-sky solutions are shown as green lines in Figure 2. The lower TOA ocean albedo in the clear-sky version is equivalent to a positive radiative forcing, and as a result the bifurcation diagram as a whole is shifted to lower radiative forcings. Importantly, removing clouds shifts the waterbelt states less than the present-day-like states, and so waterbelt states can become hidden in the absence of clouds. In other words, cloud masking makes waterbelt states more accessible.

### 2.3 Shortwave cloud feedback

We now adapt the EBM to also account for changes in shortwave reflection by clouds. These can result from changes in cloud cover and cloud condensate as ice expands towards the equator. Although cloud feedbacks are subject to considerable uncertainty and are known to affect the transition from present-day-like climates into a Snowball Earth (Poulsen & Jacob, 2004; Voigt & Marotzke, 2010; Eisenman & Armour, 2024; Renoult et al., 2024), no previous work has explored their impact on waterbelt states. In both the original and Jormungand versions of the EBM, shortwave reflection by clouds is included in the TOA albedo. But because the TOA albedo of each of the three surface types is constant, there is no shortwave cloud feedback.

We develop a model version to capture the shortwave cloud feedback in a qualitative manner. We focus on the shortwave component of the cloud feedback because the GCM simulations presented later show that the shortwave component dominates model differences in the cloud feedback. We do not consider the longwave component; accounting for it would require a more complex approach that includes cloud height and the temperature difference between the cloud and the surface.

We implement the shortwave cloud feedback as follows. Cloud reflectivity is assumed to remain constant as long as ice has not reached a certain latitude $x_c$. Once ice surpasses this latitude, cloud reflectivity increases. While clouds affect the TOA albedo over both ice and ocean surfaces, their effect is much smaller over ice surfaces due to the higher surface albedo. Consequently, and in line with our implementation of cloud masking, we restrict the cloud feedback to ocean regions and implement it by allowing the TOA ocean albedo $\alpha_o$ to vary with the ice-line latitude. As for cloud masking, this simplification is supported by the GCM results presented later.

When the ice line reaches the latitude where the cloud feedback is triggered, $x_i = x_c$, the TOA albedo over open ocean is changed by $\Delta\alpha_1^c$ from a reference value $\alpha_o^{ref}$. $\Delta\alpha_1^c > 0$ implies an albedo increase and a positive (destabilizing) cloud feedback; for $\Delta\alpha_1^c < 0$ the feedback is negative (stabilizing). We implement the feedback analogous to the Jormungand mechanism,

$$\alpha_o(x_i) = \alpha_o^{ref} + \left(\frac{\Delta\alpha_o^c}{2}\right)\left(1 - \tanh\left(\frac{x_c - x_i}{\Delta x_c}\right)\right). \tag{6}$$

The albedo increase occurs gradually over a transition zone with width $\Delta x_c$. Except for the TOA ocean albedo, the model version is identical to the Jormungand version.

The bifurcation diagram with the cloud feedback included in addition to the Jormungand mechanism is shown in Figure 2. By design, the cloud feedback has no effect as long as the ice line is poleward of $x_c$. When the ice line approaches $x_c$ and the cloud feedback is assumed to be positive, the TOA ocean albedo increases, the shortwave feedback becomes more positive, and waterbelt states are destabilized. A positive shortwave cloud feedback, therefore, reduces the range of radiative forcing over which waterbelt states exist and reduces their accessibility. A negative cloud feedback has the opposite effect.

### 2.4 Feedback analysis from the ice-line perspective

In the original version of the EBM, the shortwave feedback results only from the constant difference in the TOA albedo between ice and ocean regions. With the adaptations for the Jormungand mechanism and the cloud feedback, the TOA albedo becomes a function of snow cover and cloud properties, and even for the same surface type changes as a function of the ice-line latitude. This makes the shortwave feedback more complex. We therefore now study the shortwave feedback in more detail, including a decomposition into its individual components.

We follow Roe and Baker (2010) and consider the shortwave feedback from the ice-line perspective. In studies of anthropogenic global warming as well as in previous Snowball studies (Renoult et al., 2024; Eisenman & Armour, 2024), feedbacks are typically considered from a temperature perspective, with units of $\mathrm{W\,m^{-2}\,K^{-1}}$. In the ice-line perspective, in contrast, feedbacks have units of $\mathrm{W\,m^{-2}\,deglat^{-1}}$. This perspective focuses on the position of the ice line and asks how the global-mean TOA energy balance in $\mathrm{W\,m^{-2}}$ changes when the ice line advances towards the equator or retreats poleward by 1 degree latitude. In the ice-line perspective, it is straightforward to analytically derive the shortwave feedback in the EBM. We also use this perspective later for the GCM simulations.

The shortwave feedback is given by the change in the TOA global-mean net incoming shortwave radiation $S$,

$$S = \frac{Q}{4}(1 - \alpha_p(x_i)), \tag{7}$$

per degree latitude change of the ice line,

$$\lambda_{sw} = \frac{dS}{dx_i} = -\frac{Q}{4}\frac{d\alpha_p}{dx_i} > 0. \tag{8}$$

$\lambda_{sw}$ is positive because $\alpha_p$ decreases as the ice line retreats poleward. Here and in the following, we derive the feedback as derivative with respect to the sine of the ice-line latitude $x_i$, and then convert it from units of $\mathrm{W\,m^{-2}}$ to the desired units of $\mathrm{W\,m^{-2}\,deglat^{-1}}$ by multiplying with $\cos\varphi_i/90\,\mathrm{deg\,lat}$. The conversion uses that $dx_i = \cos\varphi_i d\varphi_i$ and that $x_i$ varies from 0 to 1, while $\varphi_i$ varies from 0 to 90 degrees latitude.

We aim to to separate the shortwave feedback into contributions from the ice-albedo feedback, the cloud feedback and cloud masking. Computing the shortwave feedback requires the derivative of the TOA global-mean albedo. With Equation 4 and the mathematical identity $\frac{d}{dx}\int_a^x f(y)dy = f(x)$, we write

$$\frac{d\alpha_p(x_i)}{dx_i} = (\alpha_o(x_i) - \alpha_i(x_i))s(x_i) + \frac{d\alpha_o(x_i)}{dx_i}\int_0^{x_i} s(x)dx. \tag{9}$$

The first term on the r.h.s. is the ice-albedo feedback in all-sky conditions (with clouds and cloud masking); the second term is the cloud feedback. With Equation 6 and $\frac{d}{dx}\tanh(x) = 1 - \tanh^2(x)$, the cloud feedback is

$$\frac{d\alpha_o(x_i)}{dx_i} = -\frac{\Delta\alpha_o^c}{2\Delta x_c}\left(1 - \tanh^2\left(\frac{x_i - x_c}{\Delta x_c}\right)\right), \tag{10}$$

and the shortwave feedback is

$$\lambda_{sw} = \frac{Q}{4}\left\{(\alpha_i(x_i) - \alpha_o(x_i))s(x_i) + \frac{\Delta\alpha_o^c}{2\Delta x_c}\left(1 - \tanh^2\left(\frac{x_i - x_c}{\Delta x_c}\right)\right)\int_0^{x_i} s(x)dx\right\}. \tag{11}$$

To compute the cloud masking contribution, we introduce the clear-sky TOA ocean albedo

$$\alpha_o^{clr} < \alpha_o, \tag{12}$$

which is a constant model parameter independent of the position of the ice line. From this, we define the clear-sky ice-albedo feedback (without clouds and cloud masking, indicated by the superscript $clr$) as

$$\lambda_{ice}^{clr} = \frac{Q}{4}(\alpha_i(x_i) - \alpha_o^{clr})s(x_i). \tag{13}$$

The above computations result in the decomposition of the shortwave feedback into the sum of the clear-sky ice-albedo feedback, the cloud feedback, and cloud masking

$$\lambda_{sw} = \lambda_{ice}^{clr} + \lambda_{cld} + \lambda_{mask}. \tag{14}$$

The clear-sky ice-albedo feedback is positive and given by Equation 13. The cloud feedback, as derived above, is given by

$$\lambda_{cld} = \frac{Q}{4}\frac{\Delta\alpha_o^c}{2\Delta x_c}\left(1-\tanh^2\left(\frac{x_i-x_c}{\Delta x_c}\right)\right)\int_0^{x_i} s(x)dx \tag{15}$$

and can be positive or negative depending on the sign of $\alpha_o^c$. Cloud masking is negative and given by

$$\lambda_{mask} = \lambda_{ice} - \lambda_{ice}^{clr} = \frac{Q}{4}(\alpha_o(x_i) - \alpha_o^{clr})s(x_i). \tag{16}$$

Note that all three contributions depend on the position of the ice line.

The stability of the EBM solutions is determined by the total feedback, which is the sum of the shortwave and the longwave feedback. In the temperature perspective, the longwave feedback is simply the negative of the model parameter $B$. In the ice-line perspective, it is

$$\lambda_{lw} = -B\frac{d\overline{T}}{dx_i}, \tag{17}$$

where the derivative of the global-mean temperature can be calculated by evaluating Equation 1 at the ice line,

$$\frac{d\overline{T}}{dx_i} = -\frac{Q}{4C}\left((1-\tilde{\alpha}(x_i))\frac{ds(x_i)}{dx_i} - \frac{d\tilde{\alpha}(x_i)}{dx_i}s(x_i)\right). \tag{18}$$

Recall that at $x_i$, the TOA albedo is the arithmetic mean $\tilde{\alpha}(x_i)$ of the TOA ocean and ice albedos (cf. Equation 2). $\lambda_{lw}$ is negative because the insolation decreases towards the pole.

Ice lines for which the total feedback, given by the sum of the positive shortwave and the negative longwave feedback, is negative are stable solutions. On the other hand, instability occurs when the total feedback changes from negative to positive, that is, when the positive shortwave feedback starts to overwhelm the negative longwave feedback. At the bifurcations, the total feedback equals zero. We note that one can also express (in-)stability by the feedback factor

$$f(x_i) = -\frac{\lambda_{sw}}{\lambda_{lw}}, \tag{19}$$

with $f < 1$ corresponding to stable solutions, and $f > 1$ to unstable solutions. One can easily show that $f$ is the same as the feedback factor derived by Roe and Baker (2010) in their Eq. 13, provided that one takes into account that $\frac{d\tilde{\alpha}}{dx_i}$ is nonzero due to the Jormungand effect and the shortwave cloud feedback. In the following, however, we will base our discussion on the total feedback.

The feedbacks are illustrated in Figure 4. The top row shows the case of a positive cloud feedback. From the bifurcation diagram we know that waterbelt states exist but are hidden, and that the cloud feedback creates an additional small hysteresis between waterbelt states that is absent when only the Jormungand mechanism is considered. The feedback analysis helps to understand this behavior. The strength of the shortwave feedback increases as the ice line advances towards the equator because the increasing insolation leads to a stronger clear-sky ice albedo feedback. Cloud masking damps the increase in the shortwave feedback. When the ice line passes the snow line $x_s$ and enters the subtropics, the Jormungand mechanism leads to a decrease of the clear-sky ice-albedo feedback and the shortwave feedback. In the figure, the Jormungand mechanism is quantified as the decrease in the clear-sky ice-albedo feedback that occurs when the lower bare ice albedo is used in Equation 13 instead of the high snow albedo. This leads to a negative total feedback and makes stable waterbelt states possible. Shortly thereafter, however, when the ice line is near $x_c$, the strong positive cloud feedback again leads to a positive total feedback and waterbelt states are unstable. When the ice line advances beyond $x_c$, the cloud feedback ceases, the total feedback is negative again and stable waterbelt states are possible.

A positive cloud feedback leads to waterbelt states that exist only over a narrow range of radiative forcing, can be hidden, and are separated from each other by an additional small hysteresis. The opposite happens when the cloud feedback is negative, as shown in the bottom row of Figure 4. Overall, this shows that the cloud feedback can strongly modify waterbelt states, working in their favor when the feedback is negative and making them less robust when it is positive. On the other hand, cloud masking always works in favor of waterbelt states by weakening the shortwave feedback, and its stabilizing effect is stronger when clouds are more prevalent.

## 3 Diagnostics of the three factors in general circulation models

We now describe how to diagnose the three factors in simulations with general circulation models (GCM) of climate that use a three-dimensional grid to represent the large-scale fluid dynamics and small-scale physical processes of the atmosphere, ocean and land. Unlike EBMs, the position of the snow line, the TOA albedo of ocean, ice and snow-covered regions, and the distribution and radiative effects of clouds are not prescribed but computed in the GCMs. Still, as we will show, the diagnostics can be obtained from stan-

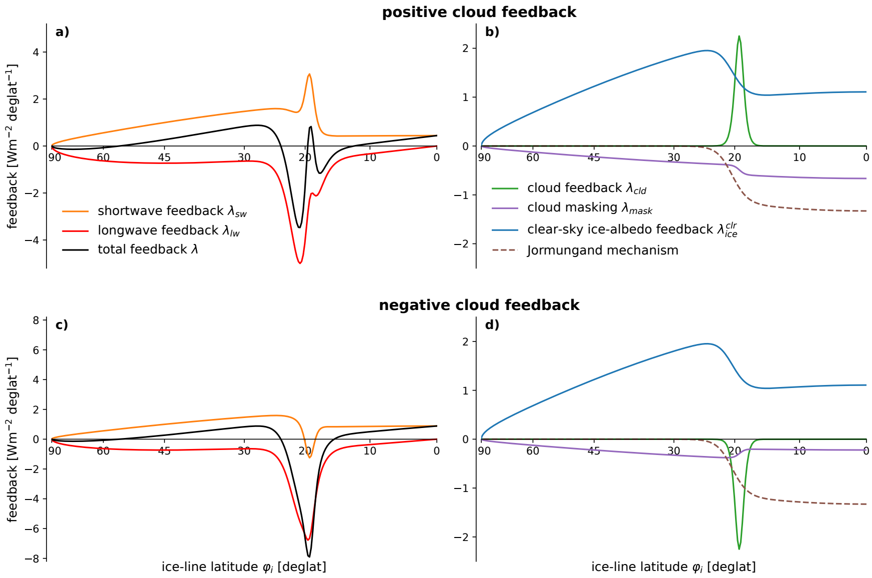


**Figure 4.** Feedback analysis in the EBM with the Jormungand mechanism and a shortwave cloud feedback. The top row shows the case of a positive shortwave cloud feedback, the bottom row the case of a negative feedback. The left panels show the total feedback and its contributions from the shortwave and longwave feedback. The right panel shows the different components of the shortwave feedback. EBM parameter values are the same as for the orange lines in Figure 2.

dard model outputs and do not require modifications to the models, making them well-suited for model intercomparison projects. Example applications will be presented in Section 4 for the ICON GCM.

### 3.1 BASIR width

Following the EBM, we define the BASIR width as the difference between the latitude of the snow and ice lines,

$$\Delta\varphi_{BASIR} = \varphi_s - \varphi_i. \tag{20}$$

For the zonally-symmetric aquaplanet setup used in this paper (see Section 4), $\varphi_i$ is calculated from the inverse sine of one minus the global-mean ice cover. $\varphi_s$ is calculated analogously.

### 3.2 Decomposition of the shortwave feedback

We assess the shortwave feedback using the approximate partial radiative perturbation method (APRP) (Taylor et al., 2007). APRP is a computationally efficient approximation of the partial radiative perturbation method (Wetherald & Manabe, 1988) that instead of detailed radiative transfer calculations requires only TOA and surface radiative fluxes in all-sky and clear-sky conditions and cloud cover. By approximating the atmosphere as a single layer, APRP decomposes the shortwave feedback into contributions from changes in surface albedo, clouds, and clear-sky atmospheric conditions. Our implementation of APRP follows M. Zelinka (2023) and M. D. Zelinka et al. (2023).

In the APRP method, the TOA albedo $\alpha$ at each longitude, latitude and time step is expressed as

$$\alpha = \alpha(c, a_{cs}, a_{oc}, \mu_{cs}, \mu_{cld}, \gamma_{cs}, \gamma_{cld}), \tag{21}$$

where $c$ is cloud cover, $a_{cs}$ is the surface albedo in clear-sky conditions ($c = 0$), and $a_{oc}$ is the surface albedo for overcast conditions ($c = 1$). $\gamma_{cs}$ and $\mu_{cs}$ represent the scattering and absorption of the clear-sky atmosphere, whereas $\mu_{cld}$ and $\gamma_{cld}$ describe the radiative properties of clouds. For a derivation and details, see Taylor et al. (2007). The clear-sky TOA albedo can be computed in the same manner by setting cloud cover to zero.

We diagnose the shortwave feedback by differencing the TOA albedo of two states, 1 and 2, whose ice-line latitudes differ by $\Delta\varphi_i = \varphi_{i,1} - \varphi_{i,2}$,

$$\lambda_{sw} = -\frac{(\alpha_1 - \alpha_2)I}{\Delta\varphi_i}. \tag{22}$$

$I$ is the insolation at TOA, which is equal to $\frac{Q}{4}s$ in the EBM, and $\alpha_{1,2}$ are the TOA albedos of state 1 and 2,

$$\alpha_1 = \alpha(c_1, a_{cs,1}, a_{oc,1}, \mu_{cs,1}, \mu_{cld,1}, \gamma_{cs,1}, \gamma_{cld,1}) \tag{23}$$

$$\alpha_2 = \alpha(c_2, a_{cs,2}, a_{oc,2}, \mu_{cs,2}, \mu_{cld,2}, \gamma_{cs,2}, \gamma_{cld,2}) \tag{24}$$

The shortwave feedback is calculated for each grid cell and climatological month, and then averaged spatially and over time to obtain the global-mean feedback. $\lambda_{sw}$ has units of $\mathrm{W\,m^{-2}\,deglat^{-1}}$, as in the EBM.

As in the EBM, we aim to decompose the shortwave feedback. We achieve this through forward and backward APRP calculations. For the cloud contribution, for example, the forward calculation computes the change in TOA albedo when the cloud properties are changed from state 1 to state 2, with the other variables kept at state 1,

$$\Delta\alpha_{cld}^{fwd} = \alpha(c_2, a_{cs,1}, a_{oc,1}, \mu_{cs,1}, \mu_{cld,2}, \gamma_{cs,1}, \gamma_{cld,2}) - \alpha_1. \tag{25}$$

The backward calculation does the opposite,

$$\Delta\alpha_{cld}^{bwd} = \alpha_2 - \alpha(c_1, a_{cs,2}, a_{oc,2}, \mu_{cs,2}, \mu_{cld,1}, \gamma_{cs,2}, \gamma_{cld,1}). \tag{26}$$

The change in TOA albedo due to cloud changes is then

$$\Delta\alpha_{cld} = \frac{1}{2}(\Delta\alpha_{cld}^{fwd} + \Delta\alpha_{cld}^{bwd}), \tag{27}$$

which yields the shortwave cloud feedback as

$$\lambda_{cld} = -\frac{\Delta\alpha^{cld} I}{\Delta\varphi_{ice}}. \tag{28}$$

The all-sky ice-albedo feedback and the feedback arising from changes in properties of the clear-sky atmosphere (most notably from changes in shortwave absorption by water vapor) are computed analogously by swapping $(a_{cs}, a_{oc})$ and $(\mu_{cs}, \gamma_{cs})$ between state 1 and 2, respectively. We also compute the clear-sky ice-albedo feedback with cloud cover set to zero, from which we diagnose the effect of cloud masking as the difference between the all-sky and clear-sky ice-albedo feedback,

$$\lambda_{mask} = \lambda_{ice} - \lambda_{ice}^{clr}. \tag{29}$$

The result is the decomposition of the shortwave feedback as

$$\lambda_{sw} = \lambda_{ice}^{clr} + \lambda_{cld} + \lambda_{mask} + \lambda_{atm}. \tag{30}$$

This is the same as in the EBM, apart from an additional small contribution from the clear-sky atmosphere feedback $\lambda_{atm}$.

We calculate the feedbacks from the GCM simulations by grouping the simulated years into 45 bins according to their annual-mean ice-line latitude. All bins have a latitude width of 2 deg. For each bin, the TOA albedos are derived, and the difference with the neighboring bins is used to compute the feedbacks.

### 3.3 Transient simulations

The factors can be computed from transient simulations that start with zero ice cover and slowly drift towards complete ice cover, where slowly means that the simulations spend enough years in each latitude bin to allow for a computation of the shortwave feedback and its decomposition. Indeed, the diagnostics can be obtained from a single transient simulation. This is in contrast to the bifurcation diagram, which requires many simulations with different atmospheric $CO_2$ values run over many hundreds of years to test for equilibrium solutions.

## 4 Example applications in three versions of the ICON GCM

We diagnose the three factors in simulations with three different versions of the atmospheric component of the ICON GCM. We examine existing simulations that use the version of the atmospheric component described in Giorgetta et al. (2018) and were performed by Braun et al. (2022). We will refer to this ICON version as ICON-A. We further analyze the set of simulations performed by Hörner and Voigt (2024), which also use the ICON-A model but with an enhanced Wegener-Bergeron-Findeisen (WBF) process to increase the reflectivity of subtropical low-level clouds, following Braun et al. (2022). We will refer to them as ICON-A-WBF. Although both Braun et al. (2022) and Hörner and Voigt (2024) calculated the same bifurcation diagram for ICON-A-WBF, we use the archived simulations from Hörner and Voigt (2024) because Braun et al. (2022) only archived zonal-mean model output. Finally, we perform new simulations that use the atmospheric component of the ICON-ESM earth system model (Jungclaus et al., 2022). ICON-ESM uses different tuning parameters for cloud microphysics and entrainment than ICON-

A, which Jungclaus et al. (2022) found beneficial when coupling with the ocean. In addition, we enhance the WBF process compared to ICON-ESM in the same manner as for ICON-A-WBF in these simulation, and hereafter refer to them as ICON-ESM-WBF.

### 4.1 ICON-A versus ICON-A-WBF: cloud masking

We start with comparing waterbelt simulations with ICON-A from Braun et al. (2022) and ICON-A-WBF from Hörner and Voigt (2024). Figure 5 shows the bifurcation diagrams. In ICON-A, waterbelt states are restricted to a narrow range of $CO_2$ and are inaccessible from the present-like climate. ICON-A-WBF, on the other hand, easily simulates waterbelt states that can be reached from the present-day-like climate by lowering $CO_2$.

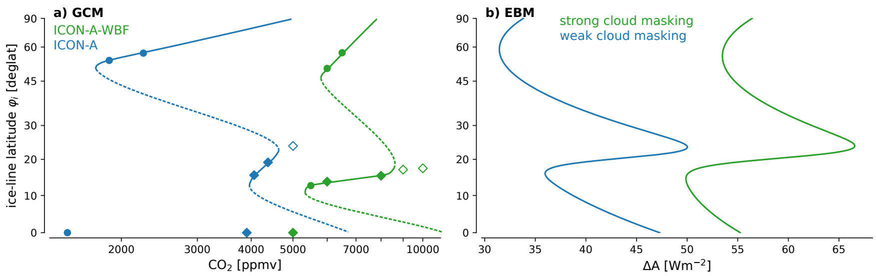


**Figure 5.** Left: bifurcation diagram for ICON-A and ICON-A-WBF. Filled symbols show stable states in equlibrium, open symbols show transient states. Simulations started from an present-day-like state are marked by circles, whereas those that start from a waterbelt state are marked by diamonds. Right: bifurcation diagram of the Jormungand EBM for strong (green) and weak (blue) cloud masking. EBM parameters are the same as for the blue solid line in Figure 2 except for $\alpha_o^{ref}$, which is 0.35 for strong cloud masking and 0.25 for weak cloud masking.

Although waterbelt states exist over a very different range of $CO_2$ radiative forcing in the two model versions, their range of ice-line latitudes is the same. This is consistent with the effect of the BASIR that we worked out using the EBM: since the evolution of the BASIR width with ice-line latitude is the same in the two model versions, as shown in Figure 5, the Jormungand mechanism and hence waterbelt states occur at the same latitudes around 13 degrees latitude.

As noted by Braun et al. (2022), the difference in waterbelt states between the two model versions results from a differences in low-latitude, low-level clouds. Sparse clouds in ICON-A lead to weaker cloud masking, allowing for a stronger shortwave feedback. In contrast, in ICON-A WBF clouds are prevalent due to the enhanced WBF process, resulting in stronger cloud masking and a weaker shortwave feedback.

Our decomposition of the shortwave feedback convincingly captures the crucial role of cloud masking. To this end, Figure 6 shows the components of the shortwave feedback as a function of the ice-line latitude, computed using the APRP method. ICON-A model output Braun et al. (2022) is only available as a zonal average, but this does not affect our analysis: diagnosing the shortwave feedback from zonally averaged instead of the latitude-longitude model output of ICON-A-WBF does not change the result (not shown). The magnitude of cloud masking stands out as the difference between ICON-A and ICON-A-WBF. In comparison, the clear-sky ice-albedo feedback, the shortwave cloud feedback, and the longwave feedback are in good agreement between the two model versions.

Overall, our diagnostics allow us to conclude the following. First, cloud masking is the primary factor responsible for the difference in waterbelt states between ICON-A and ICON-A-noWBF. This confirms Braun et al. (2022). Second, weaker cloud masking leads to waterbelt states that may become inccessible from the present-day-like climate and have a narrower $CO_2$ range. This ICON GCM result is consistent with the differences in the bifurcation diagram between the two EBM versions shown in the right panel of Figure 5, although the effect of cloud masking is much stronger in the GCM compared to the EBM. Third, both ICON versions have the same BASIR width. This explains why waterbelt states occur over the same ice-line latitudes.

### 4.2 ICON-A-WBF versus ICON-ESM-WBF: BASIR and shortwave cloud feedback

We now compare ICON-A-WBF and ICON-ESM-WBF. Figure 7 shows the bifurcation diagram for the two model versions. As discussed in the previous subsection, waterbelt states are robustly simulated in ICON-A-WBF and exist for 5,500 to 8000 ppmv $CO_2$. ICON-ESM-WBF also simulates a waterbelt state for 5,500 ppmv $CO_2$ that, as in ICON-A-WBF, is accessible from the present-day-like climate. However, waterbelt states

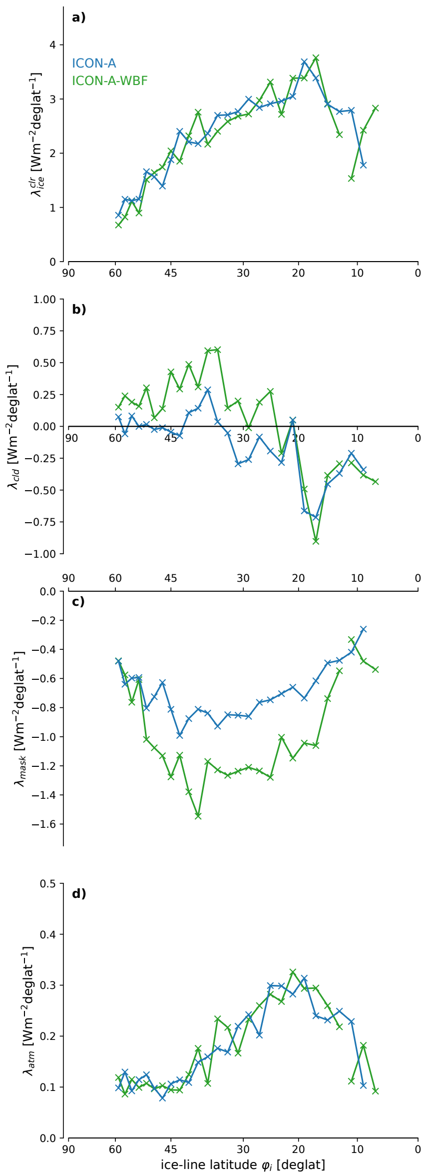


**Figure 6.** Components of the shortwave feedback in ICON-A and ICON-A-WBF calculated with the APRP method as a function of the ice-line latitude.

are limited to a $CO_2$ range of only 5,500 to 6,000 ppmv, and for 6,000 ppmv there is a second waterbelt state with an ice line shifted poleward from 13 to 22 degrees latitude. The bifurcation diagram in ICON-ESM-WBF is therefore much more complex.

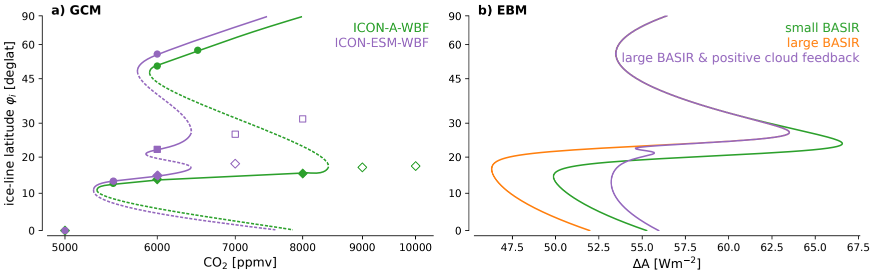


**Figure 7.** As in Figure 5 but for ICON-A-WBF and ICON-ESM-WBF. Left: bifurcation diagram for the two ICON versions. Filled symbols show stable states in equilibrium, open symbols show transient unstable states. Simulations started from a present-day-like state are marked by circles. Simulations started from the lower and upper waterbelt state are marked by diamonds and squares, respectively. Right: bifurcation diagram of the Jormungand EBM for a small BASIR (green), a large BASIR (orange), and a large BASIR and a positive shortwave cloud feedback (purple). EBM parameters are the same as for the solid blue line in Figure 2, with the following differences. Green: $x_s = 0.35$. Orange: $x_s = 0.4$. Purple: $x_s = 0.4, x_c = 0.375$, $\Delta x_c = 0.015$, $\Delta \alpha_o^c = 0.05$.

### *BASIR*

The BASIR width as a function of the ice-line latitude is shown in Figure 8 a). In both ICON versions, it increases as ice enters the subtropics, a manifestation of subtropical net evaporation ($P - E < 0$) and the Jormungand mechanism. In ICON-ESM-WBF, the BASIR expands significantly earlier, when ice passes 30 degrees latitude, and is 2 degrees latitude wider than in ICON-A-WBF for the same ice-line latitude.

The difference in the BASIR width is explained by the difference in the width of the Hadley cell, shown in Figure 8 b. Because the simulations use a hemispherically symmetric aquaplanet setup, we quantify the Hadley cell width as the subtropical zero-crossing of the mass-stream function at 500 hPa. In ICON-ESM-WBF, the Hadley cell is about 2 degrees latitude wider, favoring a wider BASIR. The impact of the Hadley cell is fur-

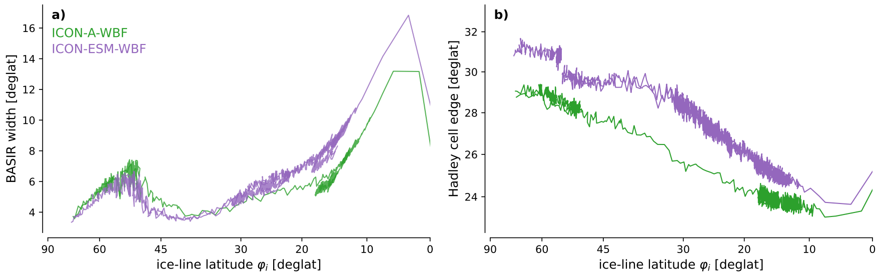


**Figure 8.** Width of the BASIR (left) and the Hadley cell (right) as a function of the ice-line latitude in ICON-A-WBF and ICON-ESM-WBF.

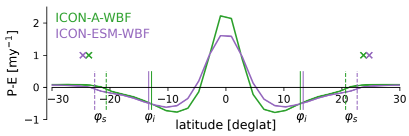


**Figure 9.** Annual-mean zonal-mean precipitation minus evaporation ($P - E$) for the waterbelt state at 5,500 ppmv $CO_2$ in ICON-ESM-WBF (purple) and ICON-A-WBF (green). The two simulations have the same ice-line latitude (solid vertical lines). The snow line (dashed vertical lines) and the Hadley cell edge (crosses), however, are shifted poleward in ICON-ESM-WBF. The BASIR width is the latitude difference between the solid and dashed vertical lines.

ther illustrated in Figure 9, which compares the two waterbelt states with 5,500 ppm $CO_2$ and an ice line at 13 degrees latitude (marked by the solid vertical lines). The snow line (vertical dashed lines) falls together with the $P - E = 0$ latitude, and the $P - E = 0$ latitude is shifted poleward in ICON-ESM-WBF due to the wider Hadley cell (marked by the crosses).

In summary, ICON-ESM-WBF simulates a wider BASIR and an earlier onset of the Jormungand mechanism. This in isolation is expected to result in waterbelt states positioned at higher latitudes in ICON-ESM-WBF compared to ICON-A-WBF. We show below that the wider BASIR indeed explains the waterbelt state with a stable ice line at 22 degrees latitude found in ICON-ESM-WBF, but that the shortwave cloud feedback is needed in addition to explain the complex structure of the bifurcation diagram of this version of ICON.

***Shortwave cloud feedback***

Figure 10 shows the different components of the shortwave feedback calculated with the APRP method. The clear-sky ice-albedo feedback agrees between the two model versions, first increasing as the ice line moves equatorward and then decreasing as ice enters subtropics. The wider BASIR in ICON-ESM-WBF should result in a weaker clear-sky feedback compared to ICON-A-WBF for subtropical ice lines, but the APRP method is too blurry to detect this impact, demonstrating the value of separately diagnosing the BASIR width.

While the cloud masking and the clear-sky shortwave feedback are the same in both model versions, the shortwave cloud feedback shows a significant difference. For ice lines poleward of 20 degrees latitude, the feedback is slightly positive in both ICON-A-WBF and ICON-ESM-WBF. However, when the ice line reaches the subtropics, ICON-A-WBF simulates a strong negative stabilizing feedback, while in ICON-ESM-WBF the feedback is weakly positive for an ice line at 20 degrees latitude. Notably, the model difference in the shortwave cloud feedback is limited to ice lines equatorward of 20 degrees latitude; in all other climate states, the cloud feedback is similar.

The difference in cloud feedback also affects the global-mean cloud radiative effect (CRE) at the top of the atmosphere, shown in Figure 11. In both models, the CRE magnitude decreases as the ice line moves toward the equator. The decrease is almost entirely due to the shortwave component of CRE and results simply from the fact that the shortwave component of CRE diminishes when the surface albedo and the clear-sky reflectance increase, even in the absence of cloud changes. When the ice line reaches 20 degrees latitude, the CRE weakens much more rapidly in ICON-A-WBF, in line with the negative shortwave cloud feedback that reduces the shortwave reflectance of clouds. This is not the case in ICON-ESM-WBF: the positive cloud feedback increases the shortwave reflection by clouds and the CRE decreases less strongly than would be expected from an increase in ice cover alone.

To further illustrate the model differences in CRE and cloud feedback, Figure 12 shows the shortwave component of CRE (left) as well as the cloud condensate (right) binned by surface type for the same waterbelt simulations with 5,500 ppmv $CO_2$ and the ice line at 13 degrees as in Figure 9. Model differences in CRE and cloud condensate are clearly dominated by the ocean, with a fifty percent higher cloud condensate in ICON-ESM-WBF

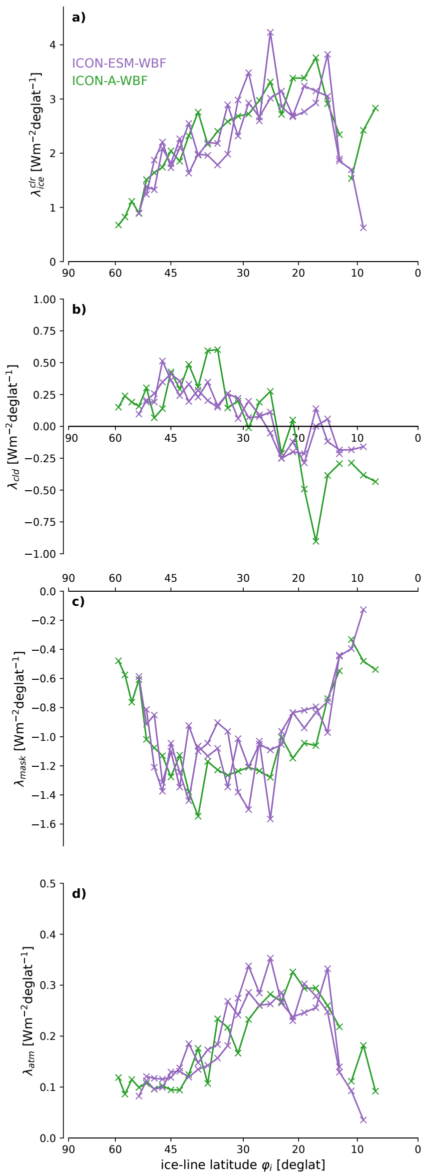


**Figure 10.** Components of the shortwave feedback in ICON-A-WBF and ICON-ESM-WBF calculated with the APRP method as a function of the ice-line latitude.

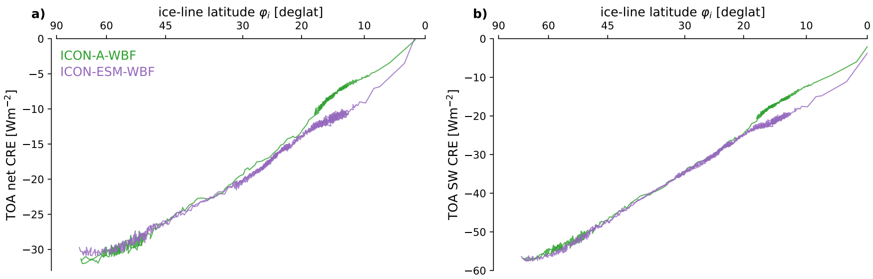


**Figure 11.** Top-of-atmosphere cloud-radiative effect for ICON-A-WBF and ICON-ESM-WBF in dependence of the annual-mean ice-line latitude. Left: net cloud-radiative effect, calculated as the sum of shortwave and longwave cloud-radiative effects. Right: shortwave cloud-radiative effect.

compared to ICON-A-WBF. Moreover, Figure 13 presents the meridional profile of the shortwave cloud feedback as a function of the ice-line latitude. Consistent with cloud condensate, the difference in the cloud feedback for subtropical ice lines results from the open ocean regions, which in ICON-ESM-WBF show a strong positive feedback that is absent in ICON-A-WBF. This, a-posteriori, justifies the our idealization made for the EBM that the cloud feedback is dominated by the behavior of ocean clouds.

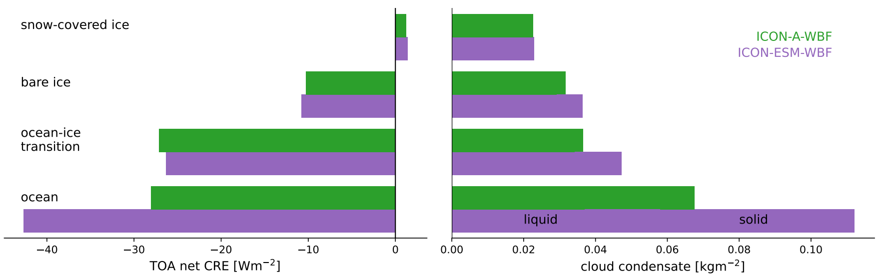


**Figure 12.** Top-of-atmsphere net cloud radiative effect (left) and cloud condensate (right) binned according to surface type for the waterbelt state at 5,500ppmv $CO_2$ in ICON-A-WBF (green) and ICON-ESM-WBF (purple). Grid cells are binned into four types: snow-covered, bare ice (ice cover larger than 0.75), ocean-ice transition (ice cover between 0.25 and 0.75), and ocean (ice cover smaller than 0.25).

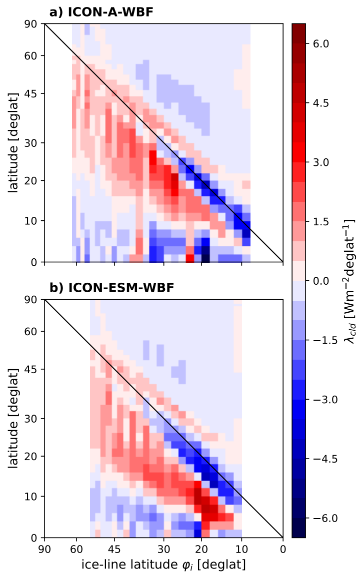


**Figure 13.** Meridional profile of the shortwave cloud feedback as a function of the ice-line latitude in ICON-A-WBF (top) and ICON-ESM-WBF (bottom). The diagonal line marks the latitude of the ice line.

**Explaining the difference in the bifurcation diagram**

Finally, we argue that the difference in the bifurcation diagram between ICON-ESM-WBF and ICON-A-WBF can be understood from the combined differences in the BASIR width and the shortwave cloud feedback. To this end, the right panel of Figure 7 compares three bifurcation diagrams computed from the EBM as approximations to the ICON GCM behavior. First, a bifurcation with an early onset of the Jormungand mechanism, a wide BASIR, and a positive cloud feedback. This case is shown in purple and represents ICON-ESM-WBF. The second case with a narrow BASIR and no shortwave cloud feedback is shown in green and represents ICON-A-WBF. The third case uses an early onset of the Jormungand mechanism and a wide BASIR and no cloud feedback. It is intended as an intermediate case between the two ICON versions and shown in orange.

The three EBM cases capture the waterbelt state differences between the two ICON versions in a remarkable qualitative manner. The earlier onset of the Jormungand mechanism and wider BASIR allow waterbelt states at higher latitudes, consistent with the isolated waterbelt state in ICON-ESM-WBF with an ice line at 22 degrees latitude. Yet, these waterbelt states are destabilized by a positive subtropical cloud feedback that also occurs in ICON-ESM-WBF and leads to an additional bifurcation for ice lines at 20 degrees latitude. Remarkably, the EBM thus explains the complex behavior of ICON-ESM-WBF as the result of a wider Hadley cell and wider BASIR on the one hand, and a positive cloud feedback on the other hand.

## 5 Conclusions

In this study, we established a framework to explain the presence or absence of waterbelt states in climate models by analyzing the role of three factors: the width of the bare sea-ice region (BASIR), cloud masking of the ice-albedo feedback, and shortwave cloud feedback. To this end, we extended the classical Budkyo-Sellers EBM energy balance model (EBM) to include the Jormungand mechanism and a shortwave cloud feedback, and we introduced a decomposition of the shortwave feedback from the ice-line perspective. We further applied the framework to simulations with three versions of the ICON global climate model, which allowed us to understand why some versions of ICON robustly simulate waterbelt states while others do not.

We summarize our findings as follows:

- BASIR width: A wider BASIR, resulting from an early onset of the Jormungand mechanism, favors waterbelt states and allows them to exist at higher latitude. In our simulations, the BASIR width is set by the width of the Hadley circulation.
- Cloud Masking: The presence of clouds at the ice margin reduces the strength of the ice-albedo feedback. Strong cloud masking, as simulated by the ICON-A-WBF model, makes waterbelt states more accessible and increases the range of $CO_2$ radiative forcing over which waterbelt states exisit.
- Shortwave Cloud Feedback: Differences in subtropical cloud properties lead to either stabilizing or destabilizing effects on waterbelt states. ICON-ESM-WBF, for example, exhibits a pronounced positive cloud feedback at low latitudes that works against waterbelt states and leads to a complex bifurcation diagram. This is different in ICON-A and ICON-A-WBF, illustrating the uncertainty in the cloud feedback and the impact of this uncertainty on waterbelt states.

An important finding of our work is that the three factors are able to explain the differences in waterbelt states between the ICON versions. Since the framework is easily applied to standard simulation output of global climate models, it lays the foundation for future model intercomparison projects aimed at advancing understanding of waterbelt states. Such an effort is planned for future work.

## Open Research Section

The data required to generate the figures as well as the code for simulation runs, post-processing and figure generation are preliminarily available at `https://ucloud.univie.ac.at/index.php/s/y2BLQAXq43Fdmri`. After acceptance, the data will be available at `https://doi.org/10.25365/phaidra.635`.

## Acknowledgments

The computational results presented have been achieved using the Vienna Scientific Cluster (VSC). Open-access funding was provided by University of Vienna. AI tools (DeepL and ChatGPT) were used to improve the grammar, writing style and wording for parts of the paper.

## References

Abbot, D. S., Voigt, A., & Koll, D. (2011). The Jormungand global climate state and implications for Neoproterozoic glaciations. *J. Geophys. Res.*, *116*(D18), D18103. doi: 10.1029/2011JD015927

Braun, C., Hörner, J., Voigt, A., & Pinto, J. G. (2022). Ice-free tropical waterbelt for Snowball Earth events questioned by uncertain clouds. *Nat. Geosci.*, *15*(6), 489–493. doi: 10.1038/s41561-022-00950-1

Budyko, M. I. (1969). The effect of solar radiation variations on the climate of the Earth. *Tellus*, *21*(5), 611–619. doi: 10.3402/tellusa.v21i5.10109

Eisenman, I., & Armour, K. C. (2024). The radiative feedback continuum from Snowball Earth to an ice-free hothouse. *Nat Commun*, *15*(1), 6582. doi: 10.1038/s41467-024-50406-w

Giorgetta, M. A., Brokopf, R., Crueger, T., Esch, M., Fiedler, S., Helmert, J., ... Stevens, B. (2018). ICON-A, the Atmosphere Component of the ICON Earth System Model: I. Model Description. *J. Adv. Model. Earth Syst.*, *10*(7), 1613–1637. doi: 10.1029/2017MS001242

Held, I. M., & Suarez, M. J. (1974). Simple albedo feedback models of the icecaps. *Tellus*, *26*(6), 613–629. doi: 10.1111/j.2153-3490.1974.tb01641.x

Hoffman, P. F., Abbot, D. S., Ashkenazy, Y., Benn, D. I., Brocks, J. J., Cohen, P. A., ... Warren, S. G. (2017). Snowball Earth climate dynamics and Cryogenian geology-geobiology. *Science Advances*, *3*(11), e1600983. doi: 10.1126/sciadv.1600983

Hörner, J., & Voigt, A. (2024). Sea-ice thermodynamics can determine waterbelt scenarios for Snowball Earth. *Earth System Dynamics*, *15*(2), 215–223. doi: 10.5194/esd-15-215-2024

Jungclaus, J. H., Lorenz, S. J., Schmidt, H., Brovkin, V., Brüggemann, N., Chegini, F., ... Claussen, M. (2022). The ICON Earth System Model Version 1.0. *J. Adv. Model. Earth Syst.*, *14*(4), e2021MS002813. doi: 10.1029/2021MS002813

North, G. R. (1975). Theory of Energy-Balance Climate Models. *J. Atmos. Sci.*, *32*(11), 2033–2043. doi: 10.1175/1520-0469(1975)032⟨2033:TOEBCM⟩2.0.CO;2

Pierrehumbert, R. T., Abbot, D. S., Voigt, A., & Koll, D. (2011). Climate of the Neoproterozoic. *Annu. Rev. Earth Pl. Sc.*, *39*(1), 417–460. doi: 10.1146/

annurev-earth-040809-152447

Poulsen, C. J., & Jacob, R. L. (2004). Factors that inhibit snowball Earth simulation. *Paleoceanography and Paleoclimatology*, *19*(4). doi: 10.1029/2004PA001056

Renoult, M., Sagoo, N., Hörner, J., & Mauritsen, T. (2024). Snowball earth transitions from last glacial maximum conditions provide an independent upper limit on earth's climate sensitivity. *EGUsphere [preprint]*. doi: 10.5194/egusphere-2024-2981

Roe, G. H., & Baker, M. B. (2010). Notes on a Catastrophe: A Feedback Analysis of Snowball Earth. *Journal of Climate*, *23*(17), 4694–4703. doi: 10.1175/2010JCLI3545.1

Rose, B. E. J. (2015). Stable "Waterbelt" climates controlled by tropical ocean heat transport: A nonlinear coupled climate mechanism of relevance to Snowball Earth. *J. Geophys. Res.-Amos.*, *120*(4), 1404–1423. doi: 10.1002/2014JD022659

Sellers, W. D. (1969). A Global Climatic Model Based on the Energy Balance of the Earth-Atmosphere System. *J. Appl. Meteor.*, *8*(3), 392–400. doi: 10.1175/1520-0450(1969)008⟨0392:AGCMBO⟩2.0.CO;2

Soden, B. J., Broccoli, A. J., & Hemler, R. S. (2004). On the Use of Cloud Forcing to Estimate Cloud Feedback. *Journal of Climate*, *17*(19), 3661–3665. doi: 10.1175/1520-0442(2004)017⟨3661:OTUOCF⟩2.0.CO;2

Taylor, K. E., Crucifix, M., Braconnot, P., Hewitt, C. D., Doutriaux, C., Broccoli, A. J., … Webb, M. J. (2007). Estimating Shortwave Radiative Forcing and Response in Climate Models. *Journal of Climate*, *20*(11), 2530–2543. doi: 10.1175/JCLI4143.1

Voigt, A., & Marotzke, J. (2010). The transition from the present-day climate to a modern Snowball Earth. *Clim. Dyn.*, *35*(5), 887–905. doi: 10.1007/s00382-009-0633-5

Waba, A. (2024). *Snowball Earth and waterbelt states in ExoCAM* (M.Sc. thesis, Universität Wien). doi: 10.25365/thesis.76131

Wetherald, R. T., & Manabe, S. (1988). Cloud Feedback Processes in a General Circulation Model. *Journal of the Atmospheric Sciences*, *45*(8), 1397–1416. doi: 10.1175/1520-0469(1988)045⟨1397:CFPIAG⟩2.0.CO;2

Wolf, E. T., Shields, A. L., Kopparapu, R. K., Haqq-Misra, J., & Toon, O. B. (2017). Constraints on Climate and Habitability for Earth-like Exoplanets Determined from a General Circulation Model. *ApJ*, *837*(2), 107. doi: 10.3847/1538-4357/aa5ffc

Yang, J., Peltier, W. R., & Hu, Y. (2012). The Initiation of Modern "Soft Snowball" and "Hard Snowball" Climates in CCSM3. Part II: Climate Dynamic Feedbacks. *J. Climate*, *25*(8), 2737–2754. doi: 10.1175/JCLI-D-11-00190.1

Zelinka, M. (2023). *mzelinka/aprp: Aug 1, 2023 Release, Zenodo.* Retrieved from `https://doi.org/10.5281/zenodo.8206763` doi: 10.5281/zenodo.8206763

Zelinka, M. D., Smith, C. J., Qin, Y., & Taylor, K. E. (2023). Comparison of methods to estimate aerosol effective radiative forcings in climate models. *Atmospheric Chemistry and Physics*, *23*(15), 8879–8898. doi: 10.5194/acp-23-8879-2023

# 7 Waterbelt states over different generations of the ICON and CAM atmospheric climate models

The third manuscript addresses research question 3: Can the inter-model difference in waterbelt state stability be explained by the sum of contributions of the Jormungand mechanism, cloud masking, and cloud feedback?

To achieve this, 5 different versions of the ICON model and 4 different versions of the CAM model are investigated. The datasets are compared according to their simulated waterbelt hysteresis. The framework developed in 6 is applied to compare the models according to their differences in cloud masking, cloud feedback and BASIR width. Result show that all CAM models show larger waterbelt hystereses, which can be related to more favorable cloud masking and cloud feedback in the CAM models.

This study was designed and written by the author and Aiko Voigt. Model setup and simulation runs were performed by the author and Aiko Voigt. Data analysis and visualization was conducted by the author. The author's contribution is therefore estimated at approximately 50%. The manuscript is still in preparation, and more models are being added to the manuscript.

**Hörner, J., & Voigt, A. (in preparation). Waterbelt states over different generations of the ICON and CAM atmospheric climate models**

# Waterbelt states over different generations of the ICON and CAM atmospheric climate models

Johannes Hörner and Aiko Voigt

## 1 Methods

We compare models of two model families: ICON and CAM. The model names and their reference are listed in Table 1. All models have the same simulation setup: an aquaplanet with a 50 m deep mixed-layer ocean, with surface albedo of snow-covered and bare sea ice set to 0.79 and 0.45 respectively. The solar constant is set to $1285\,\mathrm{W\,m^{-2}}$ with a circular orbit and an obliquity of 23.5°. Simulations are run with atmospheric $CO_2$ constant in time, and the climate is assumed to be stable if the ice-line latitude does not drift for 50 years.

### 1.1 ICON

The first model from the ICON family used in this paper is ICON-A, the release of Giorgetta et al. (2018). ICON-A-WBF is a slightly adapted version of ICON-A, where the Wegener-Bergeron-Findeisen process has been retuned to increase the liquid-ice partitioning in clouds and thus the reflectivity of clouds (Braun et al., 2022). ICON-ESM-WBF describes the newer version of the ICON-A model (Jungclaus et al., 2022). As for ICON-A-WBF, the reflectivity of clouds has been increased. ICON-A-WBF-3W differs from ICON-A-WBF in the sea-ice model, it uses a 3-layer sea-ice model instead of a 0-layer model. Equivalently, ICON-ESM-WBF-3W differs from ICON-ESM-WBF by using a 3-layer sea-ice model instead of a 0-layer model.

### 1.2 CESM/CAM

For this model family, no adaptations have been made. CAM3, CAM4 and CAM5 are subsequent releases of the CAM model. ExoCAM is a different release, it is a branch of CAM4 that has been adapted for the use with exoplanetary atmospheres. It differs from the original CAM4 model especially via its radiative model. All CAM models deploy the CSIM/CICE thermodynamical sea-ice scheme with 5 vertical layers.

## 2 Results

### 2.1 Waterbelt states

The results of all models are depicted as the evolution of the ice-line latitude in Figure 1, and as estimated bifurcation diagrams in Figure 2.

In ICON, all models show a stable waterbelt state, except those using the 3-layer sea ice scheme (ICON-A-WBF-3W and ICON-ESM-WBF-3W). In the ice-line evolution in Figure 1 d)&e), ICON-A-WBF-3W and ICON-ESM-WBF-3W show no sign of slowing ice drift when the ice line is at lower latitudes. Thus, there is no stable waterbelt in the bifurcation diagram in Figure 2. This

1

Table 1: Models used in this manuscript, their horizontal grid, sea-ice model, mode reference and dataset reference if the data is already published.

| model name | horizontal grid | sea-ice model | dataset reference | model reference |
|---|---|---|---|---|
| ICON-A | 158 km icosahedral | 0-layer Semtner | Giorgetta et al. (2018) | Braun et al. (2022) |
| ICON-A-WBF | 158 km icosahedral | 0-layer Semtner | Giorgetta et al. (2018) | Hörner and Voigt (2024) |
| ICON-ESM-WBF | 158 km icosahedral | 0-layer Semtner | Jungclaus et al. (2022) | Hörner and Voigt (2025) |
| ICON-A-WBF-3W | 158 km icosahedral | 3-layer Winton | Giorgetta et al. (2018) | Hörner and Voigt (2024) |
| ICON-ESM-WBF-3W | 158 km icosahedral | 3-layer Winton | Jungclaus et al. (2022) | - |
| CAM3 | 310 km spectral | 5-layer CSIM | Collins et al. (2004) | Braun et al. (2022) |
| ExoCAM | 4°x5° lat-lom | 5-layer CICE | Wolf et al. (2022) | Waba (2024) & new simulations |
| CAM4 | 1.9°x2.5° lat-lon | 5-layer CICE | Neale et al. (2010) | - |
| CAM5 | 1.9°x2.5° lat-lon | 5-layer CICE | Neale et al. (2012) | - |

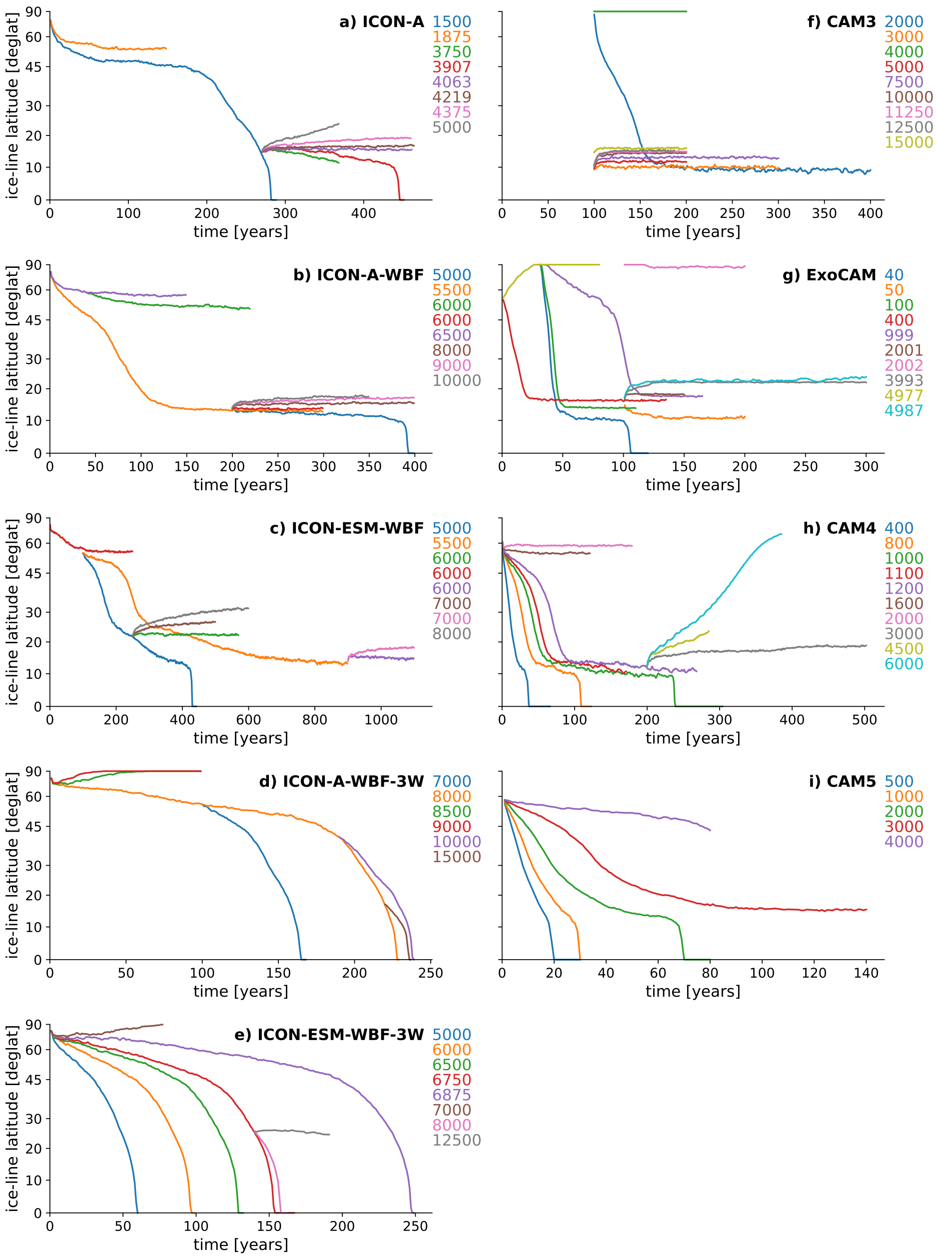


Figure 1: Evolution of the ice-line latitude for all simulations of all models. Each panel corresponds to one model, colors indicate the atmospheric $CO_2$ content of each simulation. Note that the time axis is different for each model, but the ice-line axis is shared. CAM5 results are preliminary, a stable accessible waterbelt state has been found, but no stable temperate state as of yet.

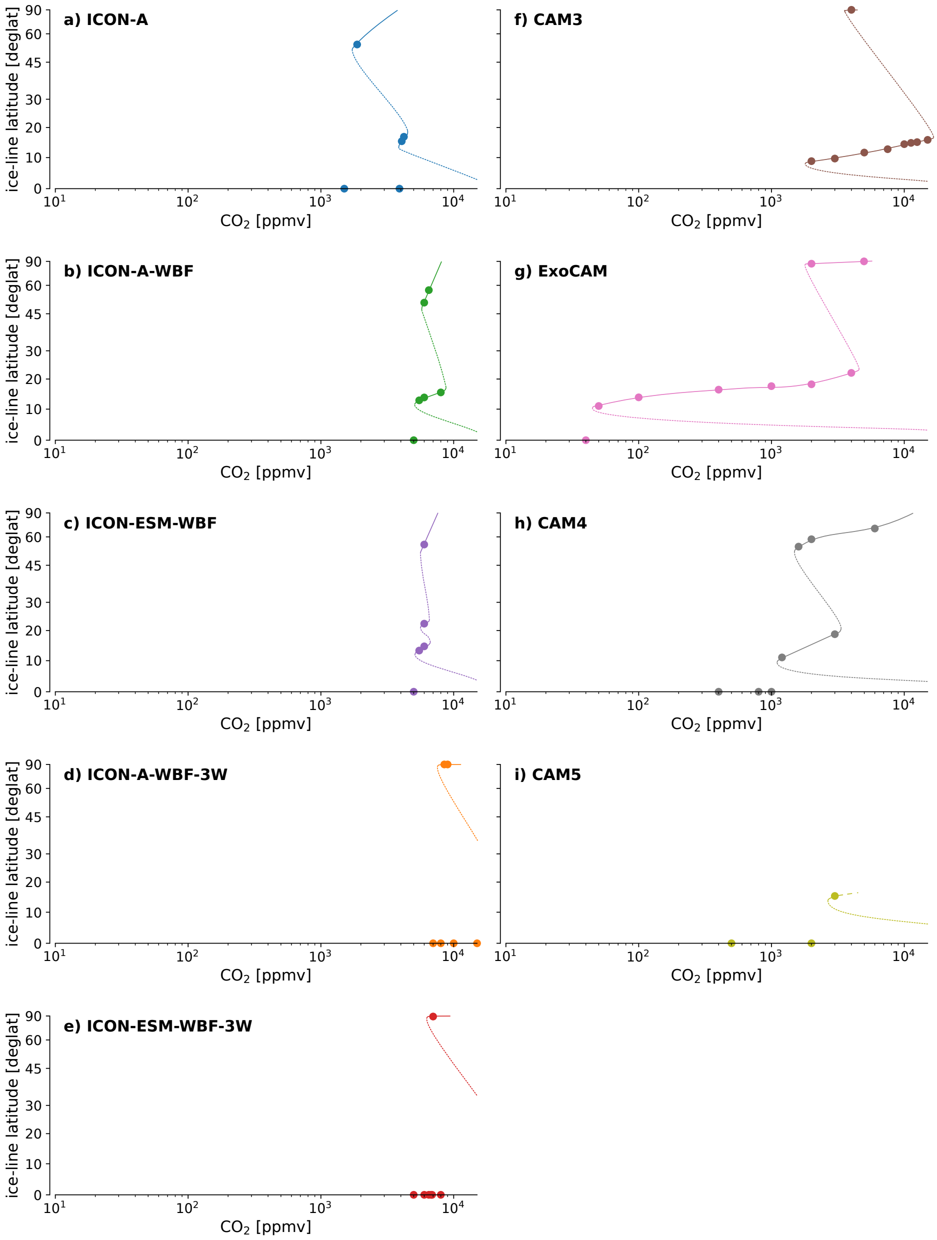


Figure 2: Estimated bifurcation diagram for each model. The atmospheric $CO_2$ content is shown on the logarithmic x-axis, the ice-line latitude on the y-axis. Only stable simulations are shown. All models share the same axes to demonstrate the differences in the bifurcation diagrams. CAM5 results are preliminary, a stable accessible waterbelt state has been found, but no stable temperate state as of yet.

demonstrates the influence of the vertical resolution of the sea ice when using ICON, described in Hörner and Voigt (2024).

Another difference is visible when comparing the ICON models with increased cloud reflectivity (ICON-A-WBF an ICON-ESM-WBF) to the ICON-A model. ICON-A-WBF and ICON-ESM-WBF have an accessible waterbelt state, whereas ICON-A only shows a smaller, inaccessible waterbelt state. This difference in waterbelt stability has been attributed to larger cloud masking when cloud reflectivity is increased (Braun et al., 2022).

ICON-ESM-WBF shows a smaller waterbelt state as ICON-A-WBF, as well as an additional stable waterbelt state at higher latitudes. This has been attributed to differences in BASIR width and cloud feedback in Hörner and Voigt (2025).

In general, the CAM models simulate a wider branch of stable waterbelt states than the ICON models, (right and left column of Figure 2). In ICON, both increased cloud reflectivity as well as a simplified 0-layer sea-ice model are necessary in order to simulate an accessible waterbelt state. In the CAM models, no such adaptations are required, the model family is much more favorable for the formation of waterbelt states. Due to this, the stable waterbelt branch in CAM3, ExoCAM and CAM4 is larger than in any of the ICON models. CAM5 also simulates one stable accessible waterbelt state, and more simulations are still being run to determine the width of the stable waterbelt branch.

The results of the CAM models also suggest a possible resolution dependency of waterbelt stability. ExoCAM and CAM3 are the models with the largest stable waterbelt branch, and their resolution is about twice as coarse as all other models (Table 1).

In general, there are large inter-model difference in the bifurcation diagrams, especially when comparing between ICON and CAM. In ICON, these differences can be attributed to differences in the sea-ice model and cloud tuning. In CAM, this has not been investigated yet. In the following section, we apply the APRP method from Hörner and Voigt (2025) to the model differences between the CAM versions, as well as between CAM and ICON.

### 2.2 Bare sea ice, cloud feedback and masking

The output of all models is analyzed according to the three factors defined in Hörner and Voigt (2025). The width of the bare sea-ice region (BASIR) is depicted in Figure 3. For each model, the BASIR width dependent on the ice-line latitude is averaged over all simulations using linear spline interpolation. The feedback parameters for clear-sky ice-albedo feedback, cloud masking, cloud feedback and clear-sky atmospheric feedback are shown in Figure 4. For each feedback factor of each model, the data is averaged over all simulations in every latitude bin.

All models show the Jormungand mechanism, as the BASIR width increases when the ice line enters low latitudes (Figure 3). This confirms that the Jormungand mechanism itself is robust across models. However, the models differ in the strength of the Jormungand mechanism.

The feedback parameters exhibit similar behavior, but with larger inter-model differences (Figure 4). In addition, the inter-model differences generally increase with increasing ice cover. Whereas models agree well in their values for the feedback factors in a temperate climate, the differences grow when the ice line reaches lower latitudes, especially in the latitude range of stable waterbelt states between 20° and 10°. This implies that models that agree well in their simulated feedback factors in a temperate climate do not necessarily do so in a much colder climate. The details of each model have an increasing impact on model results as the climate becomes colder, which complicates the interpretation and evaluation of model results.

The cloud masking in Figure 4 c) exhibits the largest systematic differences between the models. CAM3 shows the largest values for cloud masking in low latitudes, ICON-A and ExoCAM the

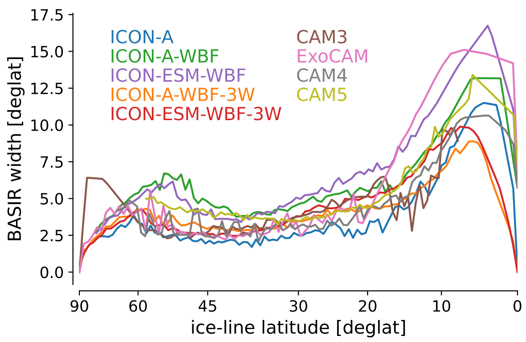


Figure 3: Width of the bare-sea ice region (BASIR) dependent on ice-line latitude for all models, indicated by different colors. For each model, the data is average over all simulations using linear spline interpolation.

smallest. This confirms the results of Braun et al. (2022), who found strong influence of cloud masking on waterbelt stability when comparing ICON-A and CAM3. CAM3 also exhibits only a small BASIR (Figure 3), which could explain why the waterbelt stretches to slightly lower latitudes in comparison to other models. The large stable waterbelt branch in CAM3 thus might be mainly due to strong cloud masking.

ExoCAM has large outliers in the feedback factors. This is likely due to the fact that the ice line drifts faster in ExoCAM than in any of the other models (Figure 1 g), which complicates the APRP feedback analysis, which requires simulations with a slower drifting ice line so that data is available for each latitude bin. On the other hand, ExoCAM shows a very strong Jormungand mechanism, as it has the largest BASIR of all models at low latitudes (Figure 3). The large stable waterbelt branch in ExoCAM could thus be due to a strong Jormungand mechanism, which also relates to a waterbelt state at higher latitudes.

CAM4 exhibits generally strong stabilizing cloud feedback in low latitudes (Figure 4 b) and also stronger cloud masking, but only a small BASIR width (Figure 3). Cloud feedback and cloud masking thus might support stable waterbelt states in CESM1-CAM4.

CAM5 exhibits the strongest stabilizing cloud feedback in low latitudes, but only weak cloud masking. This demonstrates that cloud masking and cloud feedback are independent from each other. The large stabilizing cloud feedback should thus also favor stable waterbelt states.

To diagnose the influence of cloud feedback, cloud masking and BASIR width on the width of the stable waterbelt branch, all data is aggregated into a final summary plot in Figure 5. Each model is described by one value for cloud masking, cloud feedback, BASIR width as well as the width of the stable waterbelt branch. Cloud feedback is calculated for every model by averaging over the cloud feedback factor over all bins from 20° to 10° ice-line latitude. Cloud masking is calculated equivalently. The BASIR width is averaged over the last 50 years of all stable waterbelt states per model. The width of the stable waterbelt branch is calculated as the ratio between the $CO_2$ content of the waterbelt state with the highest $CO_2$ and the lowest $CO_2$ for each model.

With this analysis, all models can be represented by a single marker in a plot with cloud masking on the x-axis, cloud feedback on the y-axis, and the BASIR width represented by the marker size in Figure 5. These are three factors that favor the stability of waterbelt states. Thus, the larger cloud masking, cloud feedback and BASIR width are in a given model, the larger we expect the stable waterbelt branch to be.

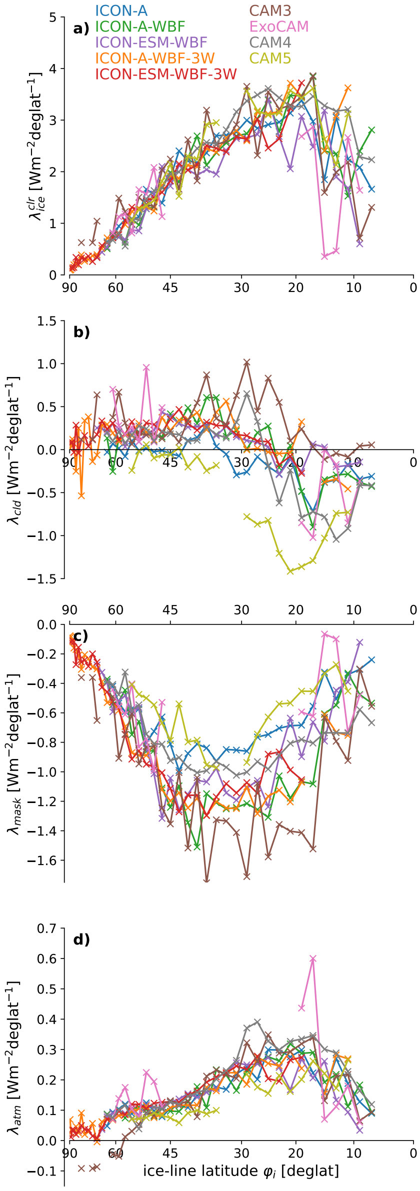


Figure 4: Feedback factors resulting from the APRP analysis dependent on ice-line latitude. Each model is indicated by a different color. a) clear-sky ice-albedo feedback, b) cloud feedback, c) cloud masking, d) clear-sky atmospheric feedback.

7

First, this plot summarizes the difference between the ICON models. ICON-A-WBF and ICON-ESM-WBF simulate larger cloud masking than ICON-A, and thus exhibit a larger stable waterbelt branch. ICON-ESM-WBF however also simulates weaker stabilizing cloud feedback, which partially compensates the stabilizing effect of the cloud masking. The larger BASIR in ICON-ESM-WBF provides an additional supporting mechanism, but it is not as strong here.

The ICON models in general, which all exhibit only a small stable waterbelt branch, are all located near the bottom left of the plot, where small values of cloud masking and cloud feedback only provide limited support for waterbelt stability. This manifests itself in the small stable waterbelt branches in the ICON models. In contrast, the CAM models exhibit larger cloud masking (CAM3), larger cloud feedback (CAM5 and ExoCAM) or both (CAM4). This is represented in the larger stable waterbelt branches in all CAM models. As such, this visualization demonstrates the importance of cloud feedback and cloud masking for waterbelt stability. Models that exhibit large values in one or both of these, tend to simulate larger stable waterbelt branches.

In this framework, the BASIR width appears to be a secondary effect for the inter-model difference of waterbelt stability. On the one hand, ExoCAM and ICON-A do show a clear dependency of BASIR width on the width of the stable waterbelt branch. On the other hand, CAM3 exhibits a large waterbelt state without large BASIR width, and ICON-ESM only exhibits a small waterbelt state with a large BASIR. This suggests that the influence of cloud masking and feedback is more important for the inter-model difference of waterbelt stability than the BASIR width.

## 3 Conclusions

In this manuscript, we analyzed a large dataset from different generations of the ICON and CAM models for the stability of waterbelt states. The CAM models are generally more favorable for simulating stable waterbelt states. Using the framework of Hörner and Voigt (2025), the differences in waterbelt stability can be attributed mainly to differences in cloud masking and cloud feedback, and only to a lesser extent to the BASIR width. This emphasizes that clouds are an important factor for the stability of waterbelt states, and cloud uncertainty is a reason for the large inter-model differences in the stability of waterbelt states.

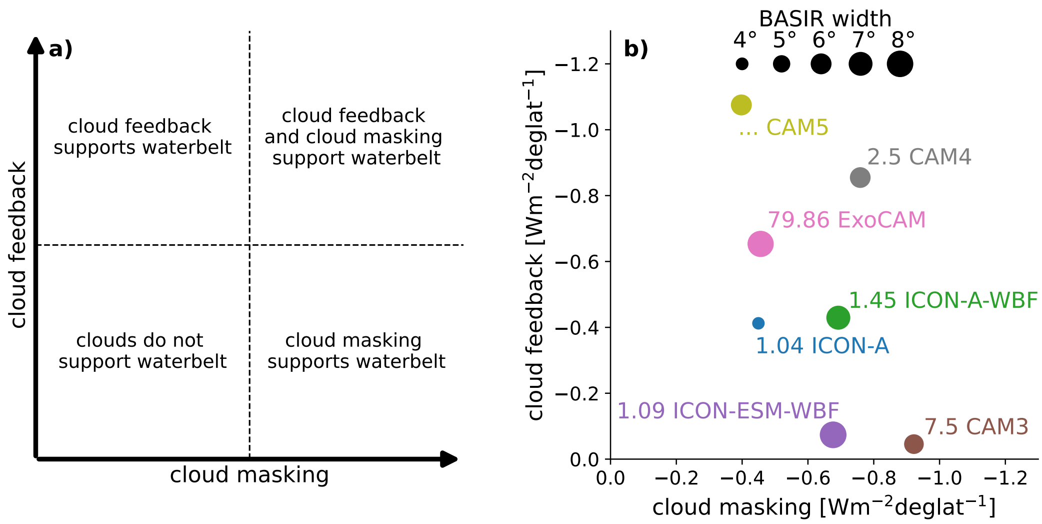


Figure 5: Cloud feedback (y-axis), cloud masking (x-axis) and BASIR width (marker size) in waterbelt states related to the width of the stable waterbelt branch (numbers) for all models. a) Schematic demonstrating how the location in the plot indicates the cloud support for waterbelt stability. b) Results diagnosed from model data. Only models with stable waterbelt states are depicted.

9

## References

Braun, C., Hörner, J., Voigt, A., and Pinto, J. G.: Ice-Free Tropical Waterbelt for Snowball Earth Events Questioned by Uncertain Clouds, Nature Geoscience, 15, 489–493, 10.1038/s41561-022-00950-1, 2022.

Collins, W. D., Rasch, P. J., Boville, B. A., Hack, J. J., McCaa, J. R., Williamson, D. L., Kiehl, J. T., Briegleb, B., Bitz, C., Lin, S.-J., Zhang, M., and Dai, Y.: Description of the NCAR Community Atmosphere Model (CAM 3.0), NCAR Technical Note, 464, 226, 2004.

Giorgetta, M. A., Brokopf, R., Crueger, T., Esch, M., Fiedler, S., Helmert, J., Hohenegger, C., Kornblueh, L., Köhler, M., Manzini, E., Mauritsen, T., Nam, C., Raddatz, T., Rast, S., Reinert, D., Sakradzija, M., Schmidt, H., Schneck, R., Schnur, R., Silvers, L., Wan, H., Zängl, G., and Stevens, B.: ICON-A, the Atmosphere Component of the ICON Earth System Model: I. Model Description, Journal of Advances in Modeling Earth Systems, 10, 1613–1637, 10.1029/2017MS001242, 2018.

Hörner, J. and Voigt, A.: Sea-Ice Thermodynamics Can Determine Waterbelt Scenarios for Snowball Earth, Earth System Dynamics, 15, 215–223, 10.5194/esd-15-215-2024, 2024.

Hörner, J. and Voigt, A.: Making Sense of Bifurcation Diagrams: A New Framework to Understand the Role of Clouds and Bare Sea Ice for Waterbelt States, ESS Open Archive, under review for JGR-A, 10.22541/essoar.173924231.15255244/v1, 2025.

Jungclaus, J. H., Lorenz, S. J., Schmidt, H., Brovkin, V., Brüggemann, N., Chegini, F., Crüger, T., De-Vrese, P., Gayler, V., Giorgetta, M. A., Gutjahr, O., Haak, H., Hagemann, S., Hanke, M., Ilyina, T., Korn, P., Kröger, J., Linardakis, L., Mehlmann, C., Mikolajewicz, U., Müller, W. A., Nabel, J. E. M. S., Notz, D., Pohlmann, H., Putrasahan, D. A., Raddatz, T., Ramme, L., Redler, R., Reick, C. H., Riddick, T., Sam, T., Schneck, R., Schnur, R., Schupfner, M., von Storch, J.-S., Wachsmann, F., Wieners, K.-H., Ziemen, F., Stevens, B., Marotzke, J., and Claussen, M.: The ICON Earth System Model Version 1.0, Journal of Advances in Modeling Earth Systems, 14, e2021MS002 813, 10.1029/2021MS002813, 2022.

Neale, R. B., Richter, J. H., Conley, A. J., Park, S., Lauritzen, P. H., Gettelman, A., Williamson, D. L., Rasch, P. J., Vavrus, S. J., Taylor, M. A., Collins, W. D., Zhang, M., and Lin, S.-J.: Description of the NCAR Community Atmosphere Model (CAM 4.0), NCAR Technical Note, 485, 2010.

Neale, R. B., Chen, C.-C., Gettelman, A., Lauritzen, P. H., Park, S., Williamson, D. L., Conley, A. J., Garcia, R., Kinnison, D., Lamarque, J.-F., Marsh, D., Mills, M., Smith, A. K., Tilmes, S., Vitt, F., Morrison, H., Cameron-Smith, P., Collins, W. D., Iacono, M. J., Easter, R. C., Ghan, S. J., Liu, X., Rasch, P. J., and Taylor, M. A.: Description of the NCAR Community Atmosphere Model (CAM 5.0), NCAR Technical Note, 486, 2012.

Waba, A.: Snowball Earth and Waterbelt States in ExoCAM, Master's thesis, University of Vienna, Wien, 2024.

Wolf, E. T., Kopparapu, R., Haqq-Misra, J., and Fauchez, T. J.: ExoCAM: A 3D Climate Model for Exoplanet Atmospheres, The Planetary Science Journal, 3, 7, 10.3847/PSJ/ac3f3d, 2022.

# 8 Further relevant literature with contributions by the author

This chapter contains a list of additional literature with contributions by the author that are relevant to the topic of this thesis.

**Hörner, J., Voigt, A., & Braun, C. (2022). Snowball Earth Initiation and the Thermodynamics of Sea Ice. *Journal of Advances in Modeling Earth Systems*, *14*(8), e2021MS002734. DOI:10.1029/2021MS002734**

This paper examines the influence of sea ice thermodynamics on Snowball Earth initiation. It provides part of the basis for chapter 5 of this thesis. This paper largely resulted from the author's master's thesis at the Karlsruhe Institute of Technology (Hörner, 2020) and is therefore not part of this thesis. The author's contribution is estimated at 80%.

**Braun, C., Hörner, J., Voigt, A., & Pinto, J. G. (2022a). Ice-free tropical waterbelt for Snowball Earth events questioned by uncertain clouds. *Nature Geoscience*, *15*(6), 489–493. DOI:10.1038/s41561-022-00950-1**

This paper investigates the influence of cloud masking on the stability of waterbelt states, and concludes that cloud masking is a major factor responsible for waterbelt states. The author's contribution was performing parts of the simulations as well as scientific discussion, estimated at 15%.

**Renoult, M., Sagoo, N., Hörner, J., & Mauritsen, T. (2024). Snowball Earth transitions from Last Glacial Maximum conditions provide an independent upper limit on Earth's climate sensitivity. *EGUsphere, under review for ESD*. DOI:10.5194/egusphere-2024-2981**

This manuscript quantifies feedback processes using the partial radiative perturbation method in coupled simulations of Snowball Earth initiation and derives constraints on climate sensitivity. The author's contribution was scientific discussion, estimated at 5%.

**Zetterberg, D., Huang, X., Hörner, J., & Voigt, A. (2025). Instantaneous radiative effect of surface long wave spectral emissivity in a Snowball Earth simulation. *ESS Open Archive, under review for JGR-A*. DOI:10.22541/essoar.173939569.91686572/v1**

This manuscript analyzes the spectrally dependent surface emission in a Snowball Earth. It postulates that the often neglected spectral dependence of surface emissions in climate models can influence model results for Snowball Earth, waterbelt states, and other cold climates. The author's contribution was to perform simulations as well as scientific discussion, estimated at 5%.

# 9 Conclusion

## 9.1 Summary

This thesis investigated the Jormungand mechanism and its influence on the stability of waterbelt states in three overarching research questions.

**RQ1: How robust is the Jormungand mechanism with respect to different sea-ice models?**

Chapter 5 demonstrates that the Jormungand mechanism, the exposure of bare sea ice as ice enters the subtropics, depends on the vertical resolution of the sea-ice model. This is achieved by running the ICON-A model with a 0-layer and a 3-layer sea-ice model. As the 0-layer model neglects the heat capacity of sea ice, it overestimates surface temperatures and hence surface ablation. This results in less snow on ice and thus a larger width of the Bare Sea-Ice Region (BASIR) near the ice edge. The Jormungand mechanism is therefore stronger when using the 0-layer sea-ice model, and a stable accessible waterbelt state is achieved. On the other hand, when the more sophisticated 3-layer sea-ice model is used, there is no indication of stable waterbelt states. This has two main implications: First, the BASIR width as a proxy of the Jormungand mechanism can determine the stability of waterbelt states. Second, low vertical resolution of sea-ice models overestimates the BASIR width and thus the stability of waterbelt states.

**RQ2: What is the contribution of the Jormungand mechanism, cloud masking, and cloud radiative feedback for the stability of waterbelt states?**

Chapter 6 introduces a framework for quantifying the influence of bare sea ice, cloud masking and cloud radiative effects on the waterbelt hysteresis, and demonstrates that all three factors shape the bifurcation diagram in different versions of the ICON model. First, the influence of the three factors on the waterbelt hysteresis are demonstrated in an adapted EBM. Second, the APRP method is applied to model output to calculate the feedback factors for cloud masking and shortwave cloud radiative feedback. The analysis shows that the BASIR width can determine the latitude of the stable waterbelt state. Cloud masking is responsible for stabilizing waterbelt states by weakening the ice-albedo feedback. A negative cloud feedback can provide an additional stabilizing mechanism, and a positive cloud feedback can destabilize waterbelt states and introduce an additional hysteresis.

**RQ3: Can the inter-model differences in waterbelt state stability be explained by the sum of contributions of the Jormungand mechanism, cloud masking, and cloud feedback?**

Chapter 7 demonstrates that the inter-model differences in the stability of waterbelt states can be related to differences in cloud masking, cloud feedback and the BASIR width. This is achieved by deploying a large set of models from different generations of the ICON and CAM models. The CAM models in general are more favorable for stable waterbelt states, and they simulate larger waterbelt hystereses. Deploying the framework from chapter 6 indicates that this is mainly due to differences in cloud masking and cloud feedback. The CAM models exhibit either larger cloud masking, stronger negative cloud feedback or both. First, this shows that the three factors can determine the inter-model difference in waterbelt state stability. Second, this shows that all CAM models in general are more favorable for simulating waterbelt states as ICON due to their simulated clouds.

## 9.2 Discussion

The main outcome of this thesis is that the inter-model difference on waterbelt states in idealized atmospheric models without ocean dynamics is largely driven by clouds as well as BASIR width. This raises the question how these factors will influence waterbelt stability in a model that represents more features of the climate system, and ultimately how this affects our understanding of waterbelt states as an alternative explanation for the Neoproterozoic Snowball Earth.

Other mechanisms that are likely to influence the BASIR width are sea-ice dynamics and ocean heat transport. Sea-ice dynamics induce a viscous ice flow of sea glaciers from high latitudes to low latitudes, which not only destabilizes a low-latitude sea-ice edge itself (Voigt & Abbot, 2012), but could also decreases the width of the BASIR due to high-albedo snow-covered sea-ice flowing equatorwards into the BASIR. On the other hand, the intense wind-driven ocean circulation in a waterbelt state converging energy to a low latitude sea-ice edge could decrease the BASIR width by melting the bare ice cover (Rose, 2015), even though the melting itself is a stabilizing effect. Due to this, the BASIR width could be decreased from both sides, weakening its stabilizing impact on waterbelt stability.

Another important prerequisite for the influence of the BASIR width on climate is the surface albedo of bare sea ice. The albedo of bare sea ice used in the simulations of this thesis is on the low edge of the suggested range of observations (Webster & Warren, 2022), which could overestimate the strength of the Jormungand mechanism in our setup. However, the low bare sea-ice albedo can be justified by the fact that we neglect other processes that are known to reduce the surface albedo of sea ice, mainly melt ponds and dust. The reduction of surface albedo due to melt ponds and dust has been proposed to enhance the deglaciation of a hard Snowball Earth (Wu et al., 2021). The low-latitude sea-ice edge in a waterbelt state would be an ideal environment for the formation of melt ponds (Yang et al., 2012b), which could further decrease the surface albedo of the BASIR. Additionally, the transport of dust from higher latitudes via the flow of sea glaciers (D. Li & Pierrehumbert, 2011) and the subsequent exposure of dust due to the melting of the covering snow layer could provide a mechanism to reduce surface albedo. This calls for more research on how the surface albedo of sea ice will change near a subtropical sea-ice edge.

Few studies have been conducted that investigate the change of cloud radiative effects or feedbacks during the transition to a Snowball Earth, and they show large differences (Voigt & Marotzke, 2010; Yang et al., 2012b; Eisenman & Armour, 2024; Renoult et al., 2024). This is expected, as cloud radiative feedbacks pose one of the largest uncertainty for climate sensitivity also in present-day climate (Zelinka et al., 2020). In a climate that is as different from today's as a waterbelt state, one can expect the uncertainties to increase significantly due to the less well constrained boundary conditions.

While there have been studies about clouds in a hard Snowball Earth (e.g., Abbot, 2014; Yan & Yang, 2024), these can not be seen as representative for clouds in a waterbelt state, due to the vastly different atmospheric conditions between the two states. The atmosphere of a Snowball Earth differs from that of a waterbelt state by being significantly dryer, colder and having a vastly different atmospheric circulation due to the lack of open water (Pierrehumbert et al., 2011). Thus, in order to understand the role of clouds for waterbelt stability, model studies with a low-latitude sea-ice edge have to be performed. Braun et al. (2022b) did study cloud reflectivity and their potential masking effect in a waterbelt climate and found it to be especially dependent on the abundance of ice nucleating particles. However, they only investigated a climate with a fixed sea ice cover, so cloud radiative feedbacks were not considered.

Consequently, it is important to study not only the state of clouds in a waterbelt state itself, but also the changes in clouds during the transition from a temperate climate to a Snowball climate. This is because, as we have shown in this thesis, clouds act as a stabilizing mechanism by masking the ice-albedo feedback, but they can also act either with or against the ice-albedo feedback via their radiative feedbacks. Due to this, the uncertain cloud feedback can assist in stabilizing or destabilizing any potential intermediate state between a temperate state and a Snowball Earth. Reducing uncertainty of cloud feedbacks during the Snowball transition is not a trivial task, as it requires better understanding of cloud controlling factors and cloud microphysics not only in the waterbelt state itself, but also in all instable climates between the temperate state and the waterbelt state.

Ultimately, the results of this thesis pose a challenge for waterbelt states stabilized by the Jormungand mechanism, as the strong influence of uncertain clouds renders waterbelt stability highly model-dependent. It is difficult to determine model performance in a waterbelt climate, thus we cannot make statements if the models that favor waterbelt state stability due to their large simulated cloud masking or cloud feedback are more or less realistic. Thus, the conclusion of this thesis questions the relevance of the Jormungand mechanism for waterbelt states stability. The stabilizing Jormungand mechanism is dependent on support from favorable cloud conditions, and thus may not be strong enough to stop the runaway ice-albedo feedback.

However, even if the Jormungand mechanism alone is not strong enough, it is still possible that it provides support for other mechanisms. The studies in this thesis show that even simulations that do not reach a stable waterbelt state show a robust increase in BASIR width with increasing ice cover, and often a slowing of ice drift when the ice line is at low latitudes. This suggests that the stabilizing effect of the Jormungand mechanism is still active, and it might act as a support for other mechanism in stabilizing waterbelt states. In particular, ocean dynamics have been shown to stabilize a waterbelt state, which is not considered in this thesis. Thus, the next crucial step for determining the plausibility of waterbelt states is to step up the model hierarchy and test the influence of the factors shown here in models representing more features of the climate system.

# Bibliography


Abbot, D. S. (2014). Resolved Snowball Earth Clouds. *Journal of Climate*, *27*(12), 4391–4402. DOI:10.1175/JCLI-D-13-00738.1.

Abbot, D. S., Eisenman, I., & Pierrehumbert, R. T. (2010). The Importance of Ice Vertical Resolution for Snowball Climate and Deglaciation. *Journal of Climate*, *23*(22), 6100–6109. DOI:10.1175/2010JCLI3693.1.

Abbot, D. S., Voigt, A., & Koll, D. (2011). The Jormungand global climate state and implications for Neoproterozoic glaciations. *Journal of Geophysical Research*, *116*(D18), D18103. DOI:10.1029/2011JD015927.

Allen, P. A., & Hoffman, P. F. (2005). Extreme winds and waves in the aftermath of a Neoproterozoic glaciation. *Nature*, *433*(7022), 123–127. DOI:10.1038/nature03176.

Bitz, C. M., & Lipscomb, W. H. (1999). An energy-conserving thermodynamic model of sea ice. *Journal of Geophysical Research: Oceans*, *104*(C7), 15669–15677. DOI:10.1029/1999JC900100.

Brady, P. V., & Carroll, S. A. (1994). Direct effects of CO2 and temperature on silicate weathering: Possible implications for climate control. *Geochimica et Cosmochimica Acta*, *58*(7), 1853–1856. DOI:10.1016/0016-7037(94)90543-6.

Braun, C. (2022). *Waterbelt scenario for the Cryogenian glaciations questioned by uncertain mixed-phase clouds* [Doctoral Thesis]. Karlsruhe Institute of Technology.

Braun, C., Hörner, J., Voigt, A., & Pinto, J. G. (2022a). Ice-free tropical waterbelt for Snowball Earth events questioned by uncertain clouds. *Nature Geoscience*, *15*(6), 489–493. DOI:10.1038/s41561-022-00950-1.

Braun, C., Voigt, A., Hoose, C., Ekman, A. M. L., & Pinto, J. G. (2022b). Controls on Subtropical Cloud Reflectivity during a Waterbelt Scenario for the Cryogenian Glaciations. *Journal of Climate*, *35*(21), 3457–3476. DOI:10.1175/JCLI-D-22-0241.1.

Brocks, J. J., & Butterfield, N. J. (2009). Early animals out in the cold. *Nature*, *457*(7230), 672–673. DOI:10.1038/457672a.

Budyko, M. I. (1969). The effect of solar radiation variations on the climate of the Earth. *Tellus*, *21*(5), 611–619. DOI:10.3402/tellusa.v21i5.10109.

Catling, D. C., & Kasting, J. F. (2017). *Atmospheric Evolution on Inhabited and Lifeless Worlds*. Cambridge University Press. DOI:10.1017/9781139020558.

Collins, W. D., Rasch, P. J., Boville, B. A., Hack, J. J., McCaa, J. R., Williamson, D. L., Briegleb, B. P., Bitz, C. M., Lin, S.-J., & Zhang, M. (2006). The Formulation and Atmospheric Simulation of the Community Atmosphere Model Version 3 (CAM3). *Journal of Climate*, *19*(11), 2144–2161. DOI:10.1175/JCLI3760.1.

Crockett, W. W., Shaw, J. O., Simpson, C., & Kempes, C. P. (2024). Physical constraints during Snowball Earth drive the evolution of multicellularity. *Proceedings of the Royal Society B: Biological Sciences*, *291*(2025), 20232767. DOI:10.1098/rspb.2023.2767.

Crowley, T. J., Hyde, W. T., & Peltier, W. R. (2001). CO2 levels required for deglaciation of a "near-snowball" Earth. *Geophysical Research Letters*, *28*(2), 283–286. DOI: 10.1029/2000GL011836.

Dadic, R., Mullen, P. C., Schneebeli, M., Brandt, R. E., & Warren, S. G. (2013). Effects of bubbles, cracks, and volcanic tephra on the spectral albedo of bare ice near the Transantarctic Mountains: Implications for sea glaciers on Snowball Earth. *Journal of Geophysical Research: Earth Surface*, *118*(3), 1658–1676. DOI:10.1002/jgrf.20098.

Danabasoglu, G., Lamarque, J.-F., Bacmeister, J., Bailey, D. A., DuVivier, A. K., Edwards, J., Emmons, L. K., Fasullo, J., Garcia, R., Gettelman, A., Hannay, C., Holland, M. M., Large, W. G., Lauritzen, P. H., Lawrence, D. M., Lenaerts, J. T. M., Lindsay, K., Lipscomb, W. H., Mills, M. J., ... Strand, W. G. (2020). The Community Earth System Model Version 2 (CESM2). *Journal of Advances in Modeling Earth Systems*, *12*(2), e2019MS001916. DOI:10.1029/2019MS001916.

Donnadieu, Y., Goddéris, Y., Ramstein, G., Nédélec, A., & Meert, J. (2004). A 'snowball Earth' climate triggered by continental break-up through changes in runoff. *Nature*, *428*(6980), 303–306. DOI:10.1038/nature02408.

Eberhard, J., Bevan, O. E., Feulner, G., Petri, S., van Hunen, J., & Baldini, J. U. L. (2023). Sensitivity of Neoproterozoic snowball-Earth inceptions to continental configuration, orbital geometry, and volcanism. *Climate of the Past*, *19*(11), 2203–2235. DOI: 10.5194/cp-19-2203-2023.

Eisenman, I., & Armour, K. C. (2024). The radiative feedback continuum from Snowball Earth to an ice-free hothouse. *Nature Communications*, *15*(1), 6582. DOI:10.1038/s41467-024-50406-w.

Evans, D. A. (2013). Reconstructing pre-Pangean supercontinents. *GSA Bulletin*, *125*(11-12), 1735–1751. DOI:10.1130/B30950.1.

Eyles, N., & Januszczak, N. (2004). 'Zipper-rift': A tectonic model for Neoproterozoic glaciations during the breakup of Rodinia after 750 Ma. *Earth-Science Reviews*, *65*(1), 1–73. DOI:10.1016/S0012-8252(03)00080-1.

Fairchild, I. J., & Kennedy, M. J. (2007). Neoproterozoic glaciation in the Earth System. *Journal of the Geological Society*, *164*(5), 895–921. DOI:10.1144/0016-76492006-191.

Feulner, G., Bukenberger, M., & Petri, S. (2023). Tracing the Snowball bifurcation of aquaplanets through time reveals a fundamental shift in critical-state dynamics. *Earth System Dynamics*, *14*(3), 533–547. DOI:10.5194/esd-14-533-2023.

Giorgetta, M. A., Brokopf, R., Crueger, T., Esch, M., Fiedler, S., Helmert, J., Hohenegger, C., Kornblueh, L., Köhler, M., Manzini, E., Mauritsen, T., Nam, C., Raddatz, T., Rast, S., Reinert, D., Sakradzija, M., Schmidt, H., Schneck, R., Schnur, R., … Stevens, B. (2018). ICON-A, the Atmosphere Component of the ICON Earth System Model: I. Model Description. *Journal of Advances in Modeling Earth Systems*, *10*(7), 1613–1637. DOI:10.1029/2017MS001242.

Gough, D. O. (1981). Solar Interior Structure and Luminosity Variations. *Solar Physics*, *74*, 21–34. DOI:10.1007/978-94-010-9633-1_4.

Grotzinger, J. P., & Knoll, A. H. (1995). Anomalous Carbonate Precipitates: Is the Precambrian the Key to the Permian? *PALAIOS*, *10*(6), 578–596. DOI:10.2307/3515096.

Harland, W. B., & Rudwick, M. J. S. (1964). The Great Infra-Cambrian Ice Age. *Scientific American*, *211*(2), 28–37.

Hoffman, P. F. (2011). Strange bedfellows: Glacial diamictite and cap carbonate from the Marinoan (635 Ma) glaciation in Namibia. *Sedimentology*, *58*(1), 57–119. DOI: 10.1111/j.1365-3091.2010.01206.x.

Hoffman, P. F. (2016). Cryoconite pans on Snowball Earth: Supraglacial oases for Cryogenian eukaryotes? *Geobiology*, *14*(6), 531–542. DOI:10.1111/gbi.12191.

Hoffman, P. F., Abbot, D. S., Ashkenazy, Y., Benn, D. I., Brocks, J. J., Cohen, P. A., Cox, G. M., Creveling, J. R., Donnadieu, Y., Erwin, D. H., Fairchild, I. J., Ferreira, D., Goodman, J. C., Halverson, G. P., Jansen, M. F., Hir, G. L., Love, G. D., Macdonald, F. A., Maloof, A. C., … Warren, S. G. (2017). Snowball Earth climate dynamics and Cryogenian geology-geobiology. *Science Advances*, *3*(11), e1600983. DOI: 10.1126/sciadv.1600983.

Hoffman, P. F., Kaufman, A. J., Halverson, G. P., & Schrag, D. P. (1998). A Neoproterozoic Snowball Earth. *Science*, *281*(5381), 1342–1346. DOI:10.1126/science.281.5381.1342.

Hoffman, P. F., & Schrag, D. (2002). The snowball Earth hypothesis: Testing the limits of global change. *Terra Nova*, *14*, 129–155. DOI:10.1046/J.1365-3121.2002.00408.X.

Hörner, J. (2020). *The Influence of Sea-ice Parameterizations on the Modelling of Snowball Earth Initiation* [Master's Thesis]. Karlsruhe Institute of Technology.

Hörner, J., & Voigt, A. (2024). Sea-ice thermodynamics can determine waterbelt scenarios for Snowball Earth. *Earth System Dynamics*, *15*(2), 215–223. DOI:10.5194/esd-15-215-2024.

Hörner, J., & Voigt, A. (2025). Making sense of bifurcation diagrams: A new framework to understand the role of clouds and bare sea ice for waterbelt states. *ESS Open Archive, under review for JGR-A*. DOI:10.22541/essoar.173924231.15255244/v1.

Hörner, J., & Voigt, A. (in preparation). Waterbelt states over different generations of the ICON and CAM atmospheric climate models.

Hörner, J., Voigt, A., & Braun, C. (2022). Snowball Earth Initiation and the Thermodynamics of Sea Ice. *Journal of Advances in Modeling Earth Systems*, *14*(8), e2021MS002734. DOI:10.1029/2021MS002734.

Hyde, W. T., Crowley, T. J., Baum, S. K., & Peltier, W. R. (2000). Neoproterozoic 'snowball Earth' simulations with a coupled climate/ice-sheet model. *Nature*, *405*(6785), 425–429. DOI:10.1038/35013005.

Kappler, A., Pasquero, C., Konhauser, K. O., & Newman, D. K. (2005). Deposition of banded iron formations by anoxygenic phototrophic Fe(II)-oxidizing bacteria. *Geology*, *33*(11), 865–868. DOI:10.1130/G21658.1.

Kirschvink, J. L. (1992). Late Proterozoic Low-Latitude Global Glaciation: The Snowball Earth. In J. W. Schopf & C. Klein (Eds.), *The Proterozoic Biosphere: A Multidisciplinary Study* (pp. 51–52). Cambridge University Press.

Knoll, A. H. (1992). The Early Evolution of Eukaryotes: A Geological Perspective. *Science*, *256*(5057), 622–627. DOI:10.1126/science.1585174.

Li, D., & Pierrehumbert, R. T. (2011). Sea glacier flow and dust transport on Snowball Earth. *Geophysical Research Letters*, *38*(17). DOI:10.1029/2011GL048991.

Li, Z. X., Bogdanova, S. V., Collins, A. S., Davidson, A., De Waele, B., Ernst, R. E., Fitzsimons, I. C. W., Fuck, R. A., Gladkochub, D. P., Jacobs, J., Karlstrom, K. E., Lu, S., Natapov, L. M., Pease, V., Pisarevsky, S. A., Thrane, K., & Vernikovsky, V. (2008). Assembly, configuration, and break-up history of Rodinia: A synthesis. *Precambrian Research*, *160*(1), 179–210. DOI:10.1016/j.precamres.2007.04.021.

Li, Z. X., Evans, D. A. D., & Halverson, G. P. (2013). Neoproterozoic glaciations in a revised global palaeogeography from the breakup of Rodinia to the assembly of Gondwanaland. *Sedimentary Geology*, *294*, 219–232. DOI:10.1016/j.sedgeo.2013.05.016.

Liu, P., Li, X., Chen, S., Lan, Z., Yang, B., Shang, X., & Yin, C. (2015). New SIMS U–Pb zircon age and its constraint on the beginning of the Nantuo glaciation. *Science Bulletin*, *60*(10), 958–963. DOI:10.1007/s11434-015-0790-3.

Liu, Y., Peltier, W. R., Yang, J., & Vettoretti, G. (2013). The initiation of Neoproterozoic "snowball" climates in CCSM3: The influence of paleocontinental configuration. *Climate of the Past*, *9*(6), 2555–2577. DOI:10.5194/cp-9-2555-2013.

Liu, Y., Peltier, W. R., Yang, J., & Hu, Y. (2018). Influence of Surface Topography on the Critical Carbon Dioxide Level Required for the Formation of a Modern Snowball Earth. *Journal of Climate*, *31*(20), 8463–8479. DOI:10.1175/JCLI-D-17-0821.1.

Love, G. D., Grosjean, E., Stalvies, C., Fike, D. A., Grotzinger, J. P., Bradley, A. S., Kelly, A. E., Bhatia, M., Meredith, W., Snape, C. E., Bowring, S. A., Condon, D. J., & Summons, R. E. (2009). Fossil steroids record the appearance of Demospongiae during the Cryogenian period. *Nature*, *457*(7230), 718–721. DOI:10.1038/nature07673.

Macdonald, F. A., Schmitz, M. D., Crowley, J. L., Roots, C. F., Jones, D. S., Maloof, A. C., Strauss, J. V., Cohen, P. A., Johnston, D. T., & Schrag, D. P. (2010). Calibrating the Cryogenian. *Science*, *327*(5970), 1241–1243. DOI:10.1126/science.1183325.

Maher, P., Gerber, E. P., Medeiros, B., Merlis, T. M., Sherwood, S., Sheshadri, A., Sobel, A. H., Vallis, G. K., Voigt, A., & Zurita-Gotor, P. (2019). Model Hierarchies for Understanding Atmospheric Circulation. *Reviews of Geophysics*, *57*(2), 250–280. DOI:10.1029/2018RG000607.

Mawson, D., & Segnit, E. R. (1949). Purple slates of the Adelaide System. *Transactions of the Royal Society of South Australia*, *72*, 276–280.

McKay, C. (2000). Thickness of tropical ice and photosynthesis on a snowball earth. *Geophysical Research Letters*, *27*(14), 2153–2156. DOI:10.1029/2000GL008525.

Merdith, A. S., Collins, A. S., Williams, S. E., Pisarevsky, S., Foden, J. D., Archibald, D. B., Blades, M. L., Alessio, B. L., Armistead, S., Plavsa, D., Clark, C., & Müller, R. D. (2017). A full-plate global reconstruction of the Neoproterozoic. *Gondwana Research*, *50*, 84–134. DOI:10.1016/j.gr.2017.04.001.

Milanković, M. (1957). Astronomische Theorie der Klimaschwankungen. In R. Kašanin (Ed.), *Monographien der Serbischen Akademie der Wissenschaften, Mathematisches Institut* (Vol. 280). Serbische Akademie der Wissenschaften.

Neale, R. B., Chen, C.-C., Gettelman, A., Lauritzen, P. H., Park, S., Williamson, D. L., Conley, A. J., Garcia, R., Kinnison, D., Lamarque, J.-F., Marsh, D., Mills, M., Smith, A. K., Tilmes, S., Vitt, F., Morrison, H., Cameron-Smith, P., Collins, W. D., Iacono, M. J., ... Taylor, M. A. (2012). Description of the NCAR community atmosphere model (CAM 5.0). *NCAR Technical Note*, *486*.

Neale, R. B., Richter, J. H., Conley, A. J., Park, S., Lauritzen, P. H., Gettelman, A., Williamson, D. L., Rasch, P. J., Vavrus, S. J., Taylor, M. A., Collins, W. D., Zhang, M., & Lin, S.-J. (2010). Description of the NCAR Community Atmosphere Model (CAM 4.0). *NCAR Technical Note*, *485*.

North, G. R. (1975). Theory of Energy-Balance Climate Models. *Journal of the Atmospheric Sciences*, *32*(11), 2033–2043. DOI:10.1175/1520-0469(1975)032<2033:TOEBCM>2.0.CO;2.

Pierrehumbert, R. T., Abbot, D. S., Voigt, A., & Koll, D. (2011). Climate of the Neoproterozoic. *Annual Review of Earth and Planetary Sciences*, *39*(1), 417–460. DOI:10.1146/annurev-earth-040809-152447.

Pincus, R., & Stevens, B. (2013). Paths to accuracy for radiation parameterizations in atmospheric models. *Journal of Advances in Modeling Earth Systems*, *5*(2), 225–233. DOI:10.1002/jame.20027.

Pollard, D., & Kasting, J. F. (2005). Snowball Earth: A thin-ice solution with flowing sea glaciers. *Journal of Geophysical Research: Oceans*, *110*(C7). DOI:10.1029/2004JC002525.

Pollard, D., & Kasting, J. F. (2006). Reply to comment by Stephen G. Warren and Richard E. Brandt on “Snowball Earth: A thin-ice solution with flowing sea glaciers”. *Journal of Geophysical Research: Oceans*, *111*(C9). DOI:10.1029/2006JC003488.

Poulsen, C. J., Pierrehumbert, R. T., & Jacob, R. L. (2001). Impact of ocean dynamics on the simulation of the neoproterozoic “snowball Earth”. *Geophysical Research Letters*, *28*(8), 1575–1578. DOI:10.1029/2000GL012058.

Prothero, D. R. (2018). *The story of the Earth in 25 rocks: Tales of important geological puzzles and the people who solved them*. Columbia university press. DOI:10.7312/prot18260.

Prothero, D. R. (2024). *The Story of Earth’s Climate in 25 Discoveries: How Scientists Found the Connections Between Climate and Life*. Columbia University Press. DOI:10.7312/prot20358.

Renoult, M., Sagoo, N., Hörner, J., & Mauritsen, T. (2024). Snowball Earth transitions from Last Glacial Maximum conditions provide an independent upper limit on Earth’s climate sensitivity. *EGUsphere, under review for ESD*. DOI:10.5194/egusphere-2024-2981.

Reusch, H. (1891). Skuringsmærker og morænegrus eftervist i Finmarken fra en periode meget ældre end "istiden". *Norges Geol. Unders.*, *1*, 78–85.

Ridgwell, A. J., Kennedy, M. J., & Caldeira, K. (2003). Carbonate Deposition, Climate Stability, and Neoproterozoic Ice Ages. *Science*, *302*(5646), 859–862. DOI:10.1126/science.1088342.

Rodehacke, C. B., Voigt, A., Ziemen, F., & Abbot, D. S. (2013). An open ocean region in Neoproterozoic glaciations would have to be narrow to allow equatorial ice sheets. *Geophysical Research Letters*, *40*(20), 5503–5507. DOI:10.1002/2013gl057582.

Roe, G. H., & Baker, M. B. (2010). Notes on a Catastrophe: A Feedback Analysis of Snowball Earth. *Journal of Climate*, *23*(17), 4694–4703. DOI:10.1175/2010JCLI3545.1.

Rooney, A. D., Strauss, J. V., Brandon, A. D., & Macdonald, F. A. (2015). A Cryogenian chronology: Two long-lasting synchronous Neoproterozoic glaciations. *Geology*, *43*(5), 459–462. DOI:10.1130/G36511.1.

Rose, B. E. J. (2015). Stable “Waterbelt” climates controlled by tropical ocean heat transport: A nonlinear coupled climate mechanism of relevance to Snowball Earth. *Journal of Geophysical Research: Atmospheres*, *120*(4), 1404–1423. DOI:10.1002/2014JD022659.

Runnegar, B. (2000). Loophole for snowball Earth. *Nature*, *405*(6785), 403–404. DOI:10.1038/35013168.

Sellers, W. D. (1969). A Global Climatic Model Based on the Energy Balance of the Earth-Atmosphere System. *Journal of Applied Meteorology*, *8*(3), 392–400. DOI:10.1175/1520-0450(1969)008<0392:AGCMBO>2.0.CO;2.

Semtner, A. J. (1976). A Model for the Thermodynamic Growth of Sea Ice in Numerical Investigations of Climate. *Journal of Physical Oceanography*, *6*(3), 379–389. DOI:10.1175/1520-0485(1976)006<0379:AMFTTG>2.0.CO;2.

Sundqvist, H., Berge, E., & Kristjánsson, J. E. (1989). Condensation and Cloud Parameterization Studies with a Mesoscale Numerical Weather Prediction Model. *Monthly Weather Review*, *117*(8), 1641–1657. DOI:10.1175/1520-0493(1989)117<1641:CACPSW>2.0.CO;2.

Tiedtke, M. (1989). A Comprehensive Mass Flux Scheme for Cumulus Parameterization in Large-Scale Models. *Monthly Weather Review*, *117*(8), 1779–1800. DOI:10.1175/1520-0493(1989)117<1779:ACMFSF>2.0.CO;2.

Vincent, W. F., Gibson, J. A. E., Pienitz, R., Villeneuve, V., Broady, P. A., Hamilton, P. B., & Howard-Williams, C. (2000). Ice Shelf Microbial Ecosystems in the High Arctic and Implications for Life on Snowball Earth. *Naturwissenschaften*, *87*(3), 137–141. DOI:10.1007/s001140050692.

Voigt, A., & Abbot, D. S. (2012). Sea-ice dynamics strongly promote Snowball Earth initiation and destabilize tropical sea-ice margins. *Climate of the Past*, *8*(6), 2079–2092. DOI:10.5194/cp-8-2079-2012.

Voigt, A., Abbot, D. S., Pierrehumbert, R. T., & Marotzke, J. (2011). Initiation of a Marinoan Snowball Earth in a state-of-the-art atmosphere-ocean general circulation model. *Climate of the Past*, *7*, 249–263. DOI:10.5194/cp-7-249-2011.

Voigt, A., & Marotzke, J. (2010). The transition from the present-day climate to a modern Snowball Earth. *Climate Dynamics*, *35*(5), 887–905. DOI:10.1007/s00382-009-0633-5.

Waldbauer, J. R., Sherman, L. S., Sumner, D. Y., & Summons, R. E. (2009). Late Archean molecular fossils from the Transvaal Supergroup record the antiquity of microbial diversity and aerobiosis. *Precambrian Research*, *169*(1), 28–47. DOI:10.1016/j.precamres.2008.10.011.

Walker, J. C. G., Hays, P. B., & Kasting, J. F. (1981). A negative feedback mechanism for the long-term stabilization of Earth's surface temperature. *Journal of Geophysical Research: Oceans*, *86*(C10), 9776–9782. DOI:10.1029/JC086iC10p09776.

Walsh, J., & Rackauckas, C. (2015). On the Budyko-Sellers energy balance climate model with ice line coupling. *Discrete and Continuous Dynamical Systems - Series B*, *20*(7), 2187–2216. DOI:10.3934/dcdsb.2015.20.2187.

Ward, W. R. (1974). Climatic variations on Mars: 1. Astronomical theory of insolation. *Journal of Geophysical Research (1896-1977)*, *79*(24), 3375–3386. DOI:10.1029/JC079i024p03375.

Warren, S. G., Brandt, R. E., Grenfell, T. C., & McKay, C. P. (2002). Snowball Earth: Ice thickness on the tropical ocean. *Journal of Geophysical Research: Oceans*, *107*(C10), 3167. DOI:10.1029/2001JC001123.

Webster, M. A., & Warren, S. G. (2022). Regional Geoengineering Using Tiny Glass Bubbles Would Accelerate the Loss of Arctic Sea Ice. *Earth's Future*, *10*(10), e2022EF002815. DOI:10.1029/2022EF002815.

Williams, G. E. (1975). Late Precambrian glacial climate and the Earth's obliquity. *Geological Magazine*, *112*(5), 441–465. DOI:10.1017/S0016756800046185.

Winton, M. (2000). A Reformulated Three-Layer Sea Ice Model. *Journal of Atmospheric and Oceanic Technology*, *17*(4), 525–531. DOI:10.1175/1520-0426(2000)017<0525:ARTLSI>2.0.CO;2.

Wolf, E. T., Kopparapu, R., Haqq-Misra, J., & Fauchez, T. J. (2022). ExoCAM: A 3D Climate Model for Exoplanet Atmospheres. *The Planetary Science Journal*, *3*(1), 7. DOI:10.3847/PSJ/ac3f3d.

Wu, J., & Liu, Y. (2023). Response of the Snowball Earth Climate to Orbital Forcing at a High CO2 Level. *Journal of Climate*, *36*(18), 6349–6362. DOI:10.1175/JCLI-D-23-0041.1.

Wu, J., Liu, Y., & Zhao, Z. (2021). How Should Snowball Earth Deglaciation Start. *Journal of Geophysical Research: Atmospheres*, *126*(2), e2020JD033833. DOI:10.1029/2020JD033833.

Yan, M., & Yang, J. (2024). Fine Cloud Structures on a Hard Snowball Earth. *Journal of Geophysical Research: Atmospheres*, *129*(10), e2023JD040688. DOI:10.1029/2023JD040688.

Yang, J., Peltier, W. R., & Hu, Y. (2012a). The Initiation of Modern “Soft Snowball” and “Hard Snowball” Climates in CCSM3. Part I: The Influences of Solar Luminosity, $CO_2$ Concentration, and the Sea Ice/Snow Albedo Parameterization. *Journal of Climate*, *25*(8), 2711–2736. DOI:10.1175/JCLI-D-11-00189.1.

Yang, J., Peltier, W. R., & Hu, Y. (2012b). The Initiation of Modern “Soft Snowball” and “Hard Snowball” Climates in CCSM3. Part II: Climate Dynamic Feedbacks. *Journal of Climate*, *25*(8), 2737–2754. DOI:10.1175/JCLI-D-11-00190.1.

Yang, J., Peltier, W. R., & Hu, Y. (2012c). The initiation of modern soft and hard Snowball Earth climates in CCSM4. *Climate of the Past*, *8*(3), 907–918. DOI:10.5194/cp-8-907-2012.

Zängl, G., Reinert, D., Rípodas, P., & Baldauf, M. (2015). The ICON (ICOsahedral Non-hydrostatic) modelling framework of DWD and MPI-M: Description of the non-hydrostatic dynamical core. *Quarterly Journal of the Royal Meteorological Society*, *141*(687), 563–579. DOI:10.1002/qj.2378.

Zelinka, M. D., Myers, T. A., McCoy, D. T., Po-Chedley, S., Caldwell, P. M., Ceppi, P., Klein, S. A., & Taylor, K. E. (2020). Causes of Higher Climate Sensitivity in CMIP6 Models. *Geophysical Research Letters*, *47*(1), e2019GL085782. DOI:10.1029/2019GL085782.

Zetterberg, D., Huang, X., Hörner, J., & Voigt, A. (2025). Instantaneous radiative effect of surface long wave spectral emissivity in a Snowball Earth simulation. *ESS Open Archive, under review for JGR-A*. DOI:10.22541/essoar.173939569.91686572/v1.

# Acronyms

**APRP** Approximate Partial Radiative Perturbation

**BASIR** Bare Sea-Ice Region

**C2SM** Center for Climate Systems Modeling

**CAM** Community Atmosphere Model

**CCSM** Community Climate System Model

**CESM** Community Earth System Model

**CRE** Cloud Radiative Effect

**DWD** German Weather Service

**EBM** Energy Balance Model

**ECHAM** Max Planck Institute Atmosphere Model

**ExoCAM** Community Atmosphere Model for Exoplanets

**GCM** General Circulation Model

**ICON** Icosahedral Nonhydrostatic Model

**ITCZ** Intertropical Convergence Zone

**KIT** Karlsruhe Institute of Technology

**MITgcm** Massachusetts Institute of Technology General Circulation Model

**MPI-M** Max Planck Institute for Meteorology

**MPI-OM** Max Planck Institute Ocean Model

**NCAR** National Center for Atmospheric Research

**P-E** Precipitation minus Evaporation

**RRTM** Rapid Radiation Transfer Model

**TOA** Top of Atmosphere

**WBF** Wegener–Bergeron–Findeisen Process

# Writing tools

The AI tools DeepL, ChatGPT and Mistral AI have been used to improve the grammar, style and wording of this text, and to find and correct spelling and grammatical mistakes.

# Acknowledgements

First of all, I would like to express my deepest gratitude to my supervisor Aiko Voigt for the valuable input and guidance over the past years, and for supporting my professional growth. I would also like to thank all my friends and colleagues at the Department of Meteorology and Geophysics, the VISESS doctoral school, and DokNawi. Thanks to my office mate Dorian, for many discussions and coffees.

I want to thank my family and my friends, who supported me through all distances and lockdowns. Finally, I want to thank Natalija. I am very glad to have you by my side in this adventure.